Accelerated Carbonated Concrete as Corrosion Environment

Saija Varjonen
M.Sc., Research Engineer
Tampere University of Technology
E-mail: saija.varjonen@tut.fi

ABSTRACT

The corrosion of steel in concrete may occur when carbonation has destroyed the protective passivation layer on the steel. Carbonation of concrete is a slow phenomenon and in laboratory studies special treatments are often used to accelerate carbonation to enable the corrosion of steel to start earlier. With accelerated methods it may be, however, not possible to achieve exactly the same result as due to the natural carbonation. This study investigated the effects of accelerated carbonation on the concrete and the potential differences between naturally carbonated concrete especially from the corrosion point of view. Corrosion rate and corrosion potential of steel bars in naturally and accelerated carbonated concrete was measured with computer-aided monitoring system. According to electrochemical measurements the corrosion rate in accelerated carbonated concrete may be smaller than in naturally carbonated concrete.

Keywords: carbonation, corrosion, accelerated carbonation, concrete

1. INTRODUCTION

1.1 Background

Among the most pressing concerns for the durability of structural concrete is the corrosion of reinforcement. It has recently received much attention as a topic of numerous experimental studies.

Reinforcing bars in alkaline concrete are protected from corrosion by a thin passivation layer. Corrosion may start when this passivation layer is destroyed, either by chloride penetration or due to the lowering of the pH by the carbonated concrete. Only carbonation is dealt with in this study.

Carbonation of concrete is a chemical reaction where atmospheric CO_2 diffuses into the pore system of concrete through the pores of concrete and causes changes into the chemical composition of concrete. In carbonation the carbon dioxide reacts principally with calcium hydroxide to form calcium carbonate [1][2]:

$$Ca(OH)_2 + CO_2 \rightarrow CaCO_3 + H_2O$$

The calcium hydroxide is not the only substance that reacts with CO_2; the other hydration products and even the residual unhydrated cement compounds also take part into carbonation reactions [3].

Due to carbonation, the alkalinity of the pore fluid drops from a pH value exceeding 12.6 to a value about of 8.0. A critical pH value, where the passive layer cannot protect the steel anymore is around 11.4 [1]. Below that level corrosion starts if there is enough moisture and oxygen present.

The volume of formed calcium carbonate exceeds that of the parent hydrate. This is why carbonation reaction generally causes a reduction in porosity [1]. According to [4] smaller pore diameters are reduced in diameter in carbonation. The effect does not seem to be significant in larger pores. The reduction of permeability due to carbonation is generally agreed, but also contradictory results, especially concerning specimens with low strength, have been published [5].

Carbonation of concrete is relatively slow under natural conditions. The progress of carbonation depth can be modelled by the following equation [6]:

$$x = k \cdot \sqrt{t}$$

where	x	is carbonation depth [mm]
	k	is carbonation coefficient [$mm/a^{0.5}$]
	t	is time [a]

Because of the slow phenomenon, the investigation of carbonation is usually conducted under accelerated conditions, with higher CO_2-concentrations, for example 4 %-vol, to speed up the process. Four weeks of accelerated carbonation in 4 %-vol is often considered as equivalent to approximately 4 years in natural conditions [7] [8].

The various factors influences carbonation [1] [4] [9]:

- The permeability of concrete
  The permeability of hardened cement paste is affected by the type of cement, the water/cement ratio, the degree of hydration (curing) and the compaction of the concrete. Correspondingly the moisture content of the concrete is also a substantial factor. The presence of water is necessary for carbonation. On the other hand, if the pores of concrete are saturated, the diffusion of carbon dioxide is slow. The diffusion rate of CO_2 in water is about four decades lower than in the air. According to [1], the rate of carbonation reaches its maximum at the range of the relative humidity of 50 to 70 %.
- The amount or reactive material
  Cement content, type and quality affect the carbonation; the more the cement, the more calcium hydroxide and the longer it takes to carbonate. Also the total alkalinity available to react with CO_2 influences carbonation.
- The content of CO_2 in the air.
  For most of the concretes studied in [7], increase of the carbon dioxide concentration beyond 4 % had little effect on carbonation rates.
- Temperature
  According to [10] the rate of carbonation is very weakly sensitive to temperature (RH 65 %).

The corrosion of steel in concrete is an electrochemical reaction where corroding steel acts as an anode (where steel dissolves as positive ions into the electrolyte) and cathode (where water reacts with oxygen producing hydroxyl ions). The reaction requires also an electrolyte in which ions migrate towards each other to form corrosion products (rust). An electron conductor between anodic and cathodic areas (steel) is also essential for the reaction [1] [11] [12].

The electrochemical sub-reactions are (Fig. 1)[12]:

Anodic: $Fe \rightarrow Fe^{2+} + 2e^{-}$

Cathodic: $2H_2O + O_2 + 4e^{-} \rightarrow 4OH^{-}$

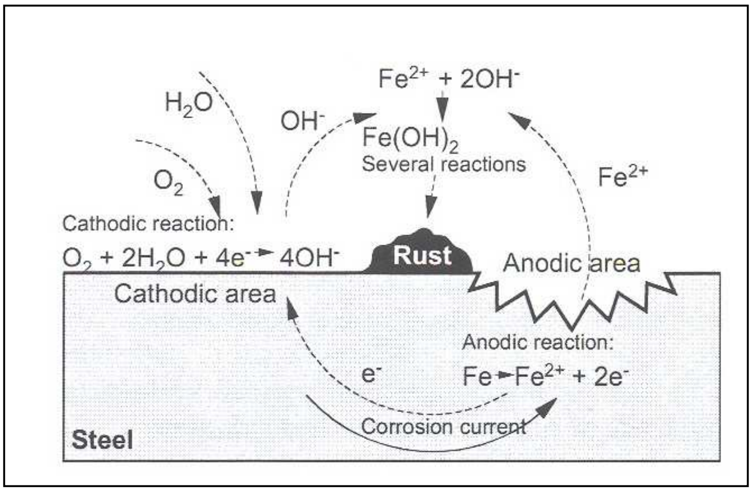

Figure 1 - Electrochemical reactions of steel corrosion in neutral or alkaline solution [12].

The rate of corrosion in chloride-free concrete depends on [12]:

- pH of pore solution
- Resistivity of electrolyte
- Oxygen supply
- Temperature.

1.2 Objective

The aim of this study was to establish whether representative specimens can be prepared by accelerated carbonation for studying active corrosion of reinforcement.

The study was limited to the effects of carbonation and carbonation induced corrosion in specimens which contain OPC. Chloride-induced corrosion, the effects of admixtures and different cementitious materials, like fly ash, ground granulated blast furnace slag and silica fume, were excluded.

2. TEST PROGRAMME

The protective properties of concrete specimens against corrosion and the corrosion rate of steel in carbonated concrete were tested using electrochemical methods. The samples were carbonated either in natural environment or under accelerated conditions. The effects of carbonation on the pore structure of concrete were determined with cup tests. Water absorption tests were used to study the capillarity of the specimens.
Carbonation chamber

Accelerated carbonation has been used at least since 1968 [12]. Curing and test conditions have varied between different laboratories because there has not been standardised method for this test. The accelerated carbonation testing of concrete was reviewed by BRE in 2000 [7]. Based on this research, standard recommendations for carbonation system have been given:

- CO_2 level 4 %
- Relative humidity 65 %
- Temperature 20 °C
- Active CO_2 control
- Efficient circulation fan
- Calibration and logging
- Reference mix.

The carbonation chamber used in this study satisfies most of the requirements. The relative humidity was 75±5 % and no reference mix was used. The progress of carbonation was followed using the phenolphthalein test.

The carbonation in the accelerated conditions used in this study can be considered to be roughly 50 times faster than in normal conditions [8].

2.1 Electrochemical measurements

The potential measurements can be used to evaluate whether the corrosion of steel takes place. When passivation layer protects the steel, the anodic reaction is prevented and the mixed potential of steel is relatively high. After the passivation layer is disrupted, the mixed potential decreases. The potential can be monitored by half-cell measurements using a simple reference electrode. The practical measurement is described for example in [13].

There are guidelines for interpreting the results of corrosion potential measurements. The connection between corrosion potential and probability of corrosion with copper-copper sulphate reference electrode is presented in Table 1 [12].

Table 1 – Correlation between half-cell potential and probability of corrosion [13].

Half-cell potential vs. CSE	Probability of corrosion
> -200 mV	Less than 10 %
-200…-350 mV	Uncertain
< -350 mV	Higher than 90 %

The corrosion rate can be evaluated by polarisation resistance method. In this method the current change is examined by the function of electrode potential (polarisation curve). The polarisation curve is close to linear near the rest potential. The slope of this linear part is called polarisation resistance ($\Delta E/\Delta I$). The corrosion rate (i_{corr}) can be evaluated by the equation [14]:

$$i_{corr} = \frac{B}{R_p \cdot A}$$

where B = coefficient that depends on the Tafel slopes
R_p = the polarisation resistance [Ω]
A = the area of polarised metal [m^2]

In the case of steel in concrete 26 mV can be used as the coefficient B when corrosion is in active state and 52 mV when corrosion is still in passive state [14].

As for potentials, there are also guidelines to interpret the results of corrosion rates (Table 2):

Table 2 – Levels of corrosion rate [15].

Attack penetration (µm/year)	Corrosion rate (µA/cm²)	Corrosion level
< 1	< 0.1	Negligible
1-5	0.1-0.5	Low
5-10	0.5-1	Moderate
> 10	> 1	High

The theoretical background for electrochemical measurements is presented for example in [12].

The electrochemical measurements in this study were performed with computer-aided measurement system, which has been prepared in the Laboratory of Structural Engineering at Tampere University of Technology. In this system, the potential is controlled and the passing current is recorded. The measurements were carried out using a CSE reference electrode with a potential of +318 mV vs. SHE. Passive steel was also used as a reference electrode for short term polarisation purposes. The potential shift used for determining R_p was +10 mV and the waiting time 40 s. The ohmic drop was compensated by the current interruption method.

Specimens of type 1:

A thin layer (2.5 mm) of OPC mortar was cast on one face of a flat section of steel. The area of the specimen exposed to corrosion was 40*75 mm² the rest of the surface being sealed by adhesive tape.

Two kinds of mortar mixes were used. The first (Mix 1) contained OPC and sand (0-0.6 mm) in the weight proportions of 1:4.5. The water/cement ratio of the mix was 1.08. The second (Mix 2) contained OPC and filler (< 0.125 mm) in the weight proportions of 1:1.6. The water/cement ratio of the second mix was 0.74. The reason for the high water/cement ratios was to enable fast carbonation. Specimens were cured on wet cloth (the cloth was in contact with water 40 °C) for one week after which they were stored at RH 75 % with minimal content of CO_2 for at least 2 weeks. After curing the specimens were covered so that only the area of 20*50 mm² was exposed (Fig. 2).

The specimens were divided into three groups (five parallel specimens in each group). One third of the specimens were retained alkaline (RH 75 %, CO_2 ~ 0 %). One third was carbonated in natural conditions (RH 75 %, CO_2 0.04 %) for 10 months. The rest was carbonated accelerated in 4 % CO_2 and 75 % relative humidity for 6 months after which they were stored at natural conditions (RH 75 %, CO_2 0.04 %) for one month.

Three specimens were sealed throughout with the adhesive tape to reveal the possible current leaks through the sealing. No measurable corrosion occurred in these specimens during the tests.

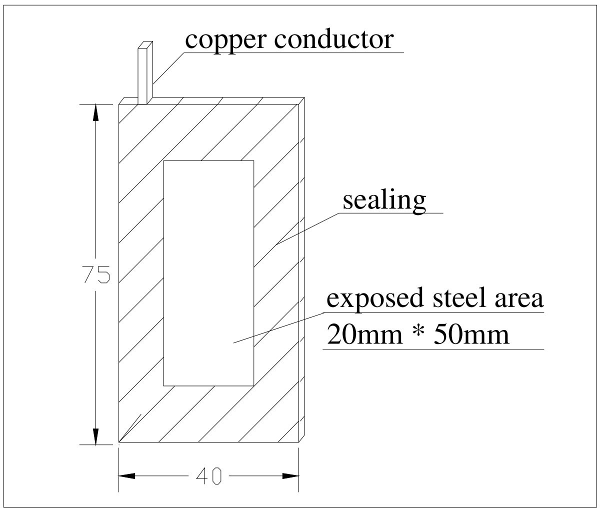

Figure 2 – Diagram of specimens of type 1.

Specimens of type 2:

Specimens of type 2 were prepared from pieces taken from a demolished concrete shelter built in 1950s-1960s. The maximum aggregate size of the concrete was 25 - 35 mm. The specimens contained reinforcing steel in alkaline and in carbonated concrete. The specimens with alkaline concrete were carbonated accelerated for 15 weeks.

For electrochemical measurements an extra layer of mortar (w/c = 0.78) was cast on the rear side of the specimens to allow the embedment of steel bars acting as counter and reference electrodes. These were steel bars with a diameter of 4 mm and nominal yield strength of 500 N/mm² (B500K) (Fig. 3).

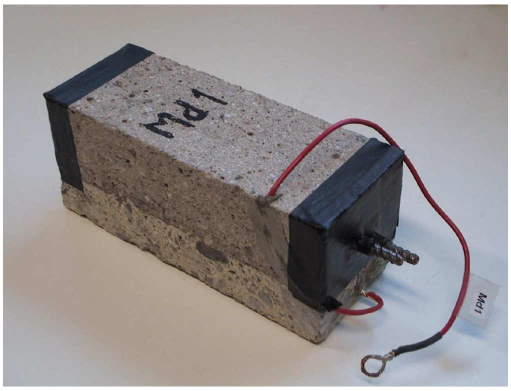

Figure 3 – Specimens of type 2.

2.2 Cup tests

Water vapour permeability of the specimens was measured by the simple cup tests. In this study the cup test were conducted to find out potential differences in porosity between normally carbonated and accelerated carbonated specimens.

The cup tests were performed in a chamber with temperature of 20 °C and RH of 75 % produced by saturated sodium chloride solution. The chamber was equipped with a blower to ensure even humidity everywhere in the chamber. The relative humidity in the cups was intended to be 97 %

(saturated potassium sulphate solution in the cup). According to measurements the RH in the cups was around 95 %.

The permeability was determined by weighing the cup periodically until the steady-state was reached. In steady-state the rate of change in weight during 7 days was measured and the water permeability calculated according to the following equation:

$$\delta = g\frac{d}{\Delta p} = \frac{\Delta m}{At}\cdot\frac{d}{\Delta p},$$

where δ = water vapour permeability [kg/(Pa·s·m)]
Δm = change in weight [kg]
A = the area of the specimen [m²]
t = time [s]
d = thickness of the specimen [m]
Δp = partial pressure gradient

The mix of the mortar was the same than used in the electrochemical measurements (Mix 1): The mortar mix contained OPC and sand (0-0.6 mm) in the weight proportions of 1:4.5. The water/cement ratio of the mix was 1.08. To enable fast carbonation the thickness of the specimens was minimised. The specimens were 103 mm in diameter and the thickness was 2.7 mm ± 0.2 mm (Fig. 4).

After a 3 weeks curing in water immersion (water 40 °C) and subsequent drying the specimens were placed in rings with inner diameter of 103 mm with melt glue. The rings were placed on the top of the cups. The joints were sealed with adhesive tape. Two “blind” cups with impermeable specimens were also prepared to reveal the possible leaks through the joints.

During the first measurements the specimens were alkaline. One half of the specimens were then carbonated accelerated in 4 % CO_2 and 75 ± 5 % relative humidity for 3 months. The other half of the specimens were carbonated normally in 0.04 %-vol CO_2 and 70 % relative humidity for 6 months. The progress of carbonation depths was determined by the means of phenolphthalein test. The 2nd test was started when the specimens were carbonated through. All the specimens were stored at 0.04 %-vol CO_2 and 70 % RH for one week before testing.

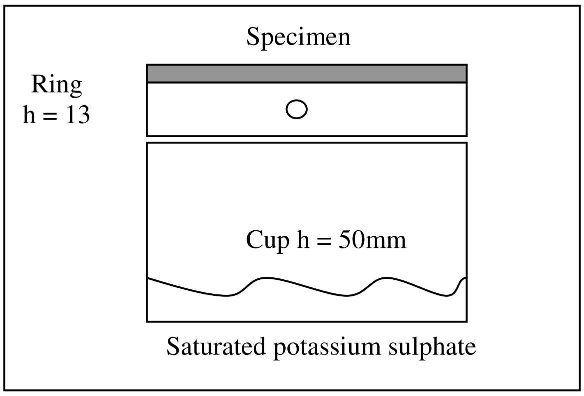

Figure 4 – Specimens of type 3.

2.3 Water absorption test

In water absorption tests dry specimens are immersed in water completely or partly. The water suction is determined by weighing the specimens periodically. Water absorption coefficient is calculated according to the following equation:

$$A = \frac{m}{\sqrt{t}},$$

where A = water absorption coefficient [kg/m²s]
m = the change in weight /the area of the specimen [kg/m²]
t = time [√s]

In this research the specimens were stored at RH ~ 0 %, and the drying was followed by weighing the specimens. When the change in weight had become steady, the specimens were placed in vacuum to finish the drying.

The specimens were prepared of the same pieces from a demolished concrete shelter than specimens of type 2 used in the electrochemical measurements. The carbonation front was measured and the specimens were sawed to specified size. A piece of concrete containing both alkaline and carbonated concrete was cut from the carbonation zone. The opposite surfaces (in two different specimens) with similar properties were reached: the other specimen was alkaline and the other carbonated. The water absorption tests were performed for the both specimens. After this the alkaline specimens were accelerated carbonated for 10-12 weeks and the tests were performed again.

The dry specimens were covered with water vapour impermeable covering. Only the sawed surface was exposed to moisture by capillary contact to free water. The specimens were weighted in the time of 1 min, 2 min, 3 min, 4 min, 5 min, 7 min, 10 min, 15 min, 20 min, 30 min, 45 min and 1 h.

The water suction to the alkaline parts of the specimens is affecting the results after the first minutes, so the emphasis was in the first 5 minutes of the test.

3. RESULTS

3.1 Corrosion potential and corrosion rate

The corrosion potential of specimens, which were carbonated in two kinds of conditions were monitored to find out any differences between their corrosion tendencies. The corrosion rates of specimens were monitored by the polarisation resistance method.

3.1.1 Specimens of type 1, Mix 1

The specimens were monitored when immersed in water. The corrosion potential measurements were carried out using a standard SCE electrode. The monitoring was made in three periods. At first, the specimens were monitored after 30 min, 3 h and 6 h immersion in water. After the first test the specimens were dried up for one week in RH 75 % after which the measurements were performed again. This time the readings were taken after 20 h and 1 week immersion. Before the 3rd monitoring the specimens were stored at RH 75 % for one week. The specimens were then monitored after 30 min, 3 h, 6 h, 24 h and 7d immersion in water.

The results from potential monitoring are presented in Figure 5 and the results from corrosion rate monitoring in Figure 6. All presented values are means of measurements on five specimens.

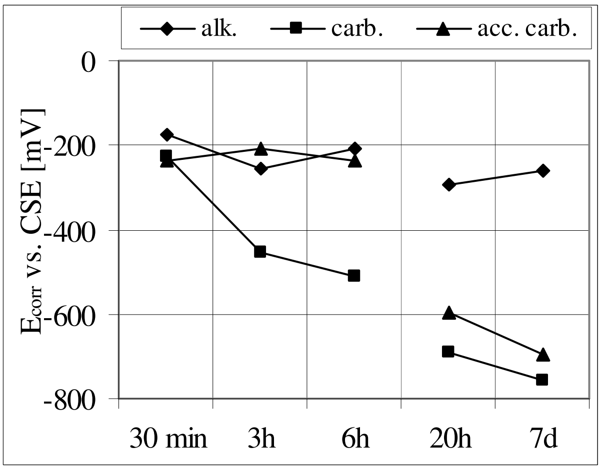

Figure 5 – The potentials of Specimens 1, Mix 1. (alk.=alkaline, carb.=carbonated in 0.04 %-vol CO_2, acc. carb.=accelerated carbonated in 4 %-vol CO_2).

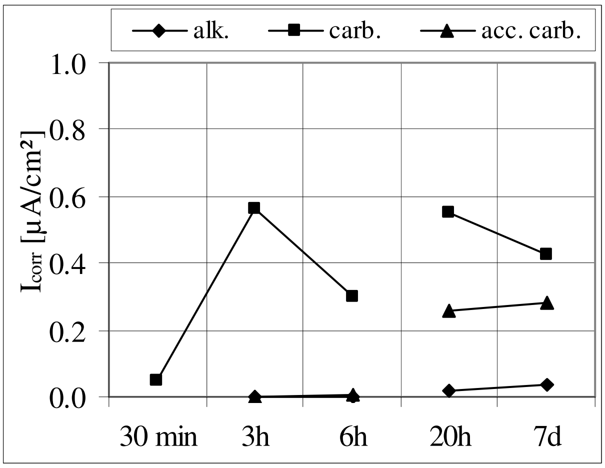

Figure 6 – The corrosion rates of Specimens 1, Mix 1. (alk.=alkaline, carb.=carbonated in 0.04 %-vol CO_2, acc. carb.=accelerated carbonated in 4 %-vol CO_2).

In the beginning of the test, the specimens were relatively dry (stored at RH 75 %) and after 30 minutes immersion the potentials were still high. Potentials of alkaline specimens were in the passive zone (>-200 mV vs. CSE) and during the test they fell into the uncertain range (-200 … -350 mV vs. CSE). The results of corrosion rate monitoring were congruent with the results of potential. The corrosion rates of alkaline specimens were below 0.1 µA/cm² (negligible corrosion) and grew a little by the end. It is possible that the passive layer weakened during the long immersion due to depletion of oxygen.

During the 1st monitoring, the potentials of carbonated specimens were in the uncertain range (-200 … -350 mV vs. CSE) after 30 minutes. The corrosion protection due to the passivation was rapidly lost in normally carbonated specimens: After 3 hours immersion in water, the potentials were below –350 mV and the corrosion rates > 0.5 µA/cm² (moderate).

At first, the corrosion was slow in accelerated carbonated specimens. The potentials remained high (>-200 mV or –200 … -350 mV) i.e. the corrosion protection was not lost during the first monitoring. The accelerated carbonated specimens lost their corrosion protection ability during the 2nd test. After 20 hours immersion the potentials were below –350 mV and the corrosion rates were observable.

The specimens were stored at RH 75 % for one week before the 3rd test started (results in Figures 7 and 8). In this time, the corrosion rates of carbonated specimens were immediately quite high (>1.0 µA/cm², high corrosion rate). There was no significant difference between normally and accelerated carbonated specimens after 30 minutes immersion. The corrosion started to decrease in time: in accelerated carbonated specimens after 30 minutes and in normally carbonated specimens after 6 hours. After 7 days the mean corrosion rate of normally carbonated specimens was 0.9 µA/cm² and in accelerated carbonated 0.8 µA/cm² (representing both moderate corrosion). Also the corrosion potentials decreased during the second test.

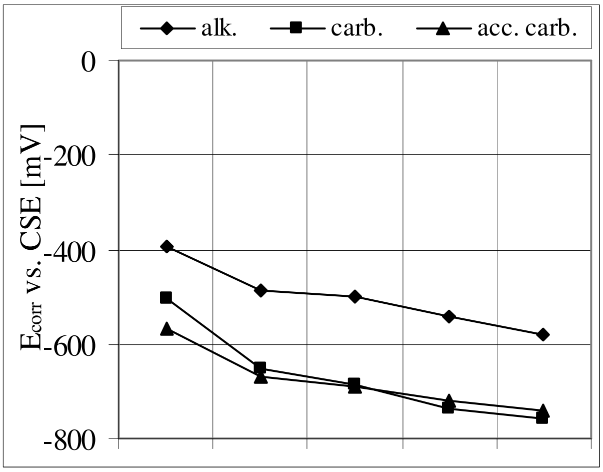

Figure 7 – The potentials of Specimens 1, Mix 1 during 3rd test.
(alk.=alkaline, carb.=carbonated in 0.04 %-vol CO_2, acc. carb.=accelerated carbonated in 4 %-vol CO_2).

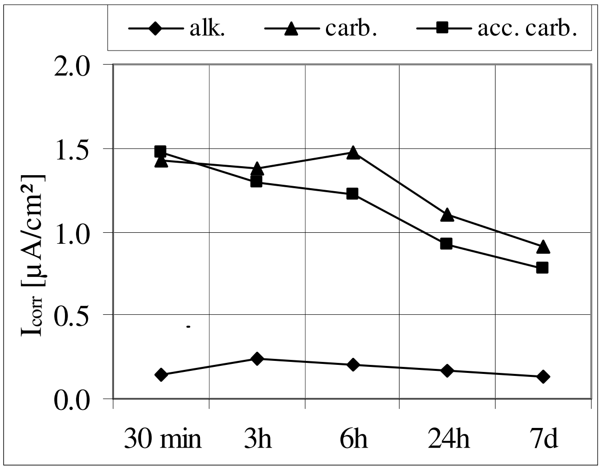

Figure 8 – The corrosion rates of Specimens 1, Mix 1 during 3rd test.
(alk.=alkaline, carb.=carbonated in 0.04 %-vol CO_2, acc. carb.=accelerated carbonated in 4 %-vol CO_2).

3.1.2 Specimens of type 1, Mix 2

The curing, carbonation and storing of the specimens were similar than with specimens of Mix 1.

The results from potential monitoring are presented in Figure 9 and the results of corrosion rate monitoring in Figure 10. All presented values are means of measurements on five specimens.

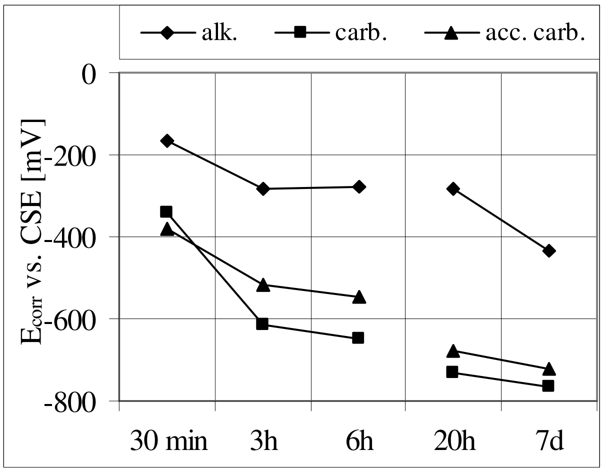

Figure10 – The corrosion rates of Specimens 1, Mix 2.
(alk.=alkaline, carb.=carbonated in 0.04 %-vol CO_2, acc. carb.=accelerated carbonated in 4 %-vol CO_2).

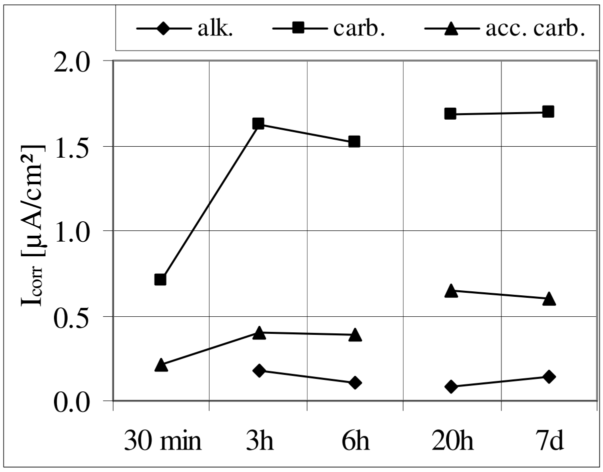

The loss of corrosion protection by depassivation was very similar with normally and accelerated carbonated specimens. Within 3 hours the corrosion potentials of them had dropped to zone < -350 mV.

Corrosion in the normally carbonated specimens was fast (> 1.0 µA/cm²) after 3 hours. Even after 30 minutes, the corrosion rate was higher than 0.50 µA/cm² (moderate corrosion).

The corrosion rate in accelerated carbonated specimens was much slower: < 0.50 µA/cm² during the 1st test and around 0.6 µA/cm² during the 2nd test.

Corrosion in the alkaline specimens was negligible.

The results from 3rd potential and corrosion rate monitoring are presented Figures 11 and 12. The corrosion rates of carbonated specimens were immediately after 30 minutes really high (>3.0 µA/cm²). The corrosion in the normally carbonated specimens was faster than in accelerated carbonated specimens. The corrosion started to decrease in time. After 7 days the mean corrosion rate of normally carbonated specimens was 2.4 µA/cm² and 1.2 µA/cm² in the accelerated carbonated specimens (both fast corrosion). The corrosion potentials decreased during the third test.

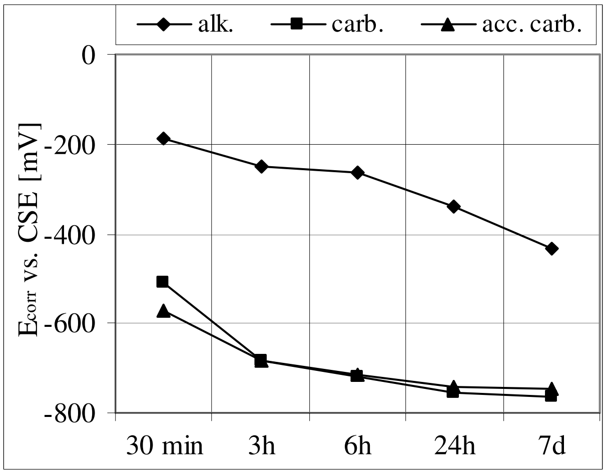

Figure 11 – The potentials of Specimens 1, Mix 2 during 3rd test.
(alk.=alkaline, carb.=carbonated in 0.04 %-vol CO_2, acc. carb.=accelerated carbonated in 4 %-vol CO_2).

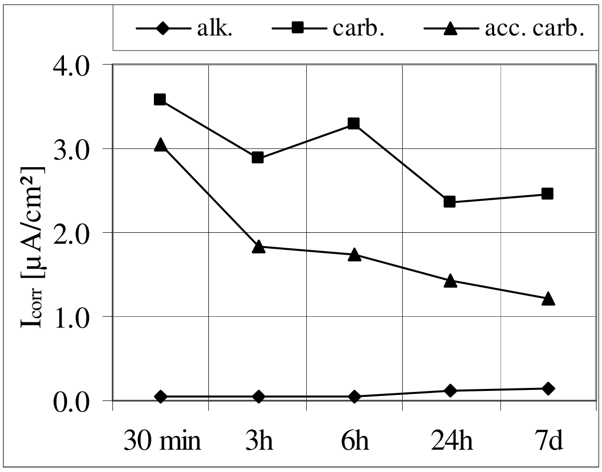

Figure 12 – The corrosion rates of Specimens 1, Mix 2 during 3rd test.
(alk.=alkaline, carb.=carbonated in 0.04 %-vol CO_2, acc. carb.=accelerated carbonated in 4 %-vol CO_2).

3.1.3 Specimens of type 2

With these specimens it was impossible to compare the initiation of the corrosion because of the different thickness of the concrete covering. The objective was to found out whether the corrosion is in longer term as fast in accelerated carbonated concrete than in naturally carbonated concrete.

Corrosion potentials of working electrodes were monitored unconventionally by using passive steel bars in alkaline concrete as a reference.

Before testing the specimens were stored at RH 75 % and 20 °C. The monitoring was made in two parts. First the specimens were laid down on wet cloths which were in contact with water (air RH 75 %, 20 °C). The specimens were monitored after 4 h, 1 d, 2 d, 4 d and 1 week contact with water. After the first test the specimens were removed to conditions of RH 97 % with no water contact. This time the readings were taken after 1, 2, 3 and 4 weeks after moving in 97 % RH.

The results of corrosion potential monitoring are presented in Figure 13. The results of corrosion rate monitoring are presented in Figure 14. Presented values are means of measurements on 8-10 specimens.

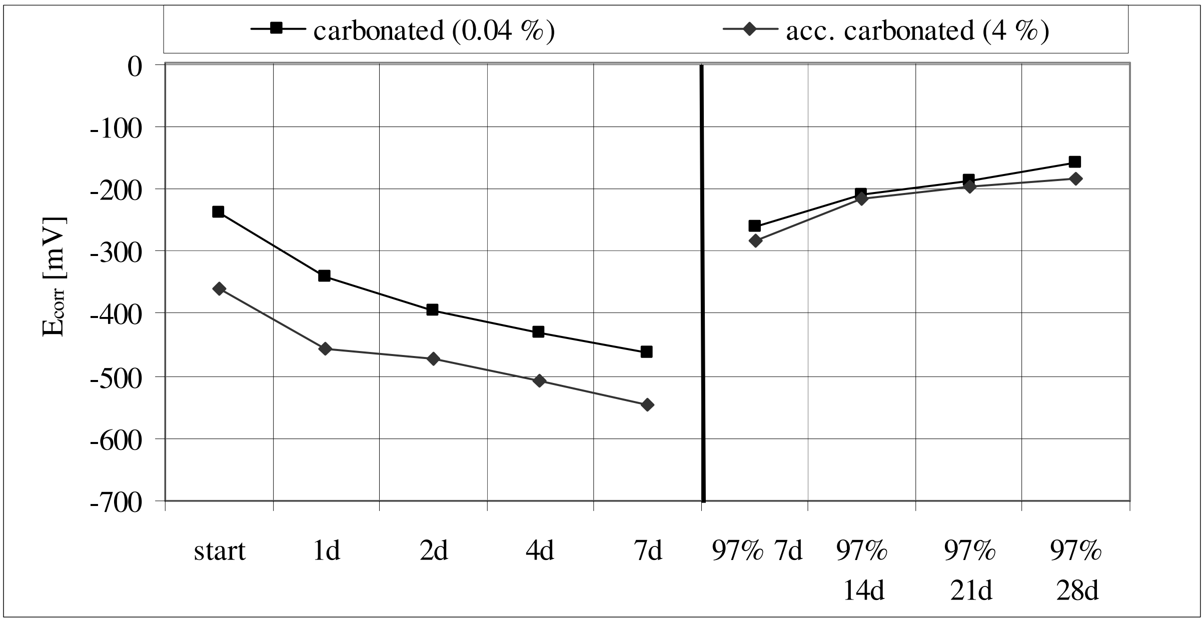

Figure 13 – The results of potential measurements (Specimens of type 2).

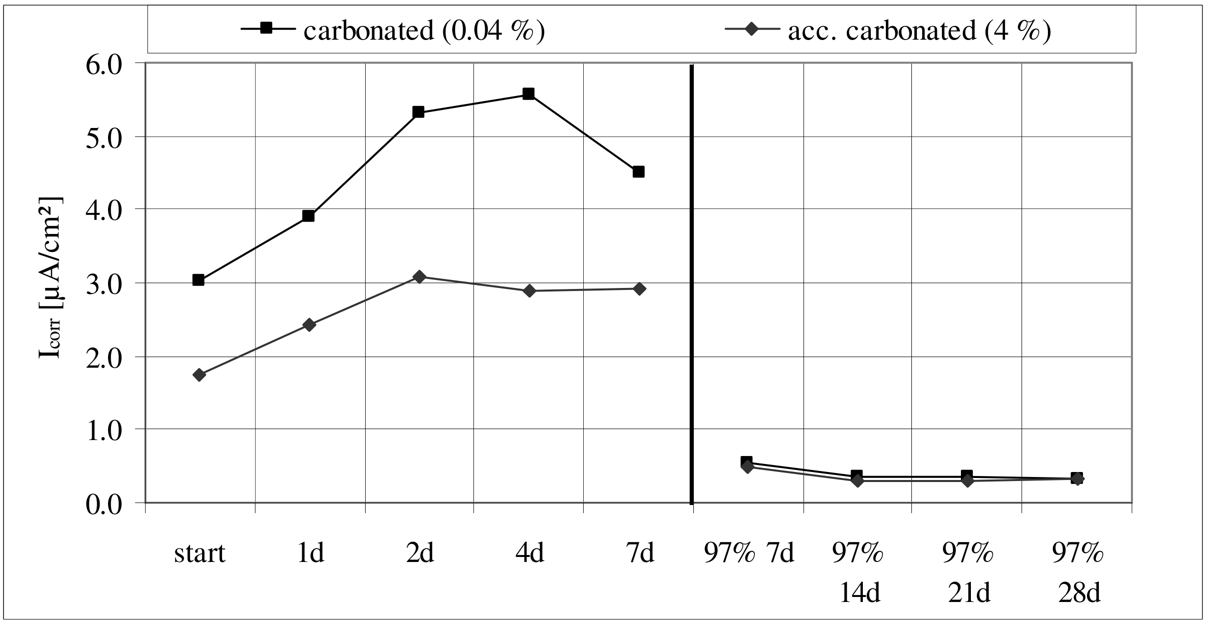

Figure 14 – The results of corrosion rate measurements (Specimens of type 2).

The corrosion potentials dropped to the level -450 … -550 mV in one week. After the water contact was removed and the specimens were stored at RH 97 %, the corrosion potentials raised remarkably. After 4 weeks the corrosion potential was so high that the probability of corrosion was minor.

The maximum corrosion rate was achieved rapidly after the specimens were laid in contact with water. The corrosion in naturally carbonated specimens was somewhat higher than in acceleratedly carbonated specimens. The corrosion rate of accelerated carbonated specimens was about 35 % smaller after 7 days than in normally carbonated specimens.

In RH 97 % the corrosion was low in both cases.

3.2 Cup tests

The results of cup tests are presented in Table 3. All the values presented in the table are means of measurements on four identical specimens.

Table 3 – The permeability related quantities calculated from the results of cup tests.

		CO_2 0.04 %		CO_2 4 %	
		alkal.	carb.	alkal.	carb.
Water vapour diffusion resistance (Z)	10^9 [m²sPa/kg]	1.58	1.08	1.67	1.24
Water vapour permeability (δ)	10^{-12} [kg/msPa]	1.77	2.56	1.62	2.16

The water vapour permeability is known to be a moisture-dependent material property. To determine an exact value, the cup test should be performed in different moisture levels. In this study the aim was not to determine the exact value, but to find differences between specimens.

The mean δ of normally carbonated specimens was 2.6 kg/msPa and mean δ of accelerated carbonated specimens 2.2 kg/msPa. The changes during carbonation were correspondingly 45 % and 34 %. The results of single specimens are presented in Table 4.

The other blind cup had a little leakage. This may have influenced the results.

Table 4 – The single results of cup test method.

		Water vapour permeability [δ] 10^{-12} [kg/msPa]		Water vapour diffusion resistance [Z] 10^{9} [m²sPa/kg]	
		alkaline	carbonated	alkaline	carbonated
CO_2 0.04%	1d	1.72	2.50	1.69	1.16
	1e	1.94	2.45	1.27	1.01
	1f	1.59	2.59	1.78	1.10
	1g	1.83	2.72	1.58	1.07
CO_2 4%	2d	2.00	2.62	1.30	0.99
	2e	1.33	1.92	2.10	1.46
	2f	1.39	1.83	1.84	1.40
	2g	1.75	2.29	1.45	1.11
Blind cups	T1	0.02	0.12	117.66	17.08
	T2	0.00	0.01	∞	168.34

3.3 Water absorption test

The curves of water absorption were determined for each specimen and the water absorption coefficients were calculated. The curve of one specimen is presented as an example in Figure 15. The other curves were almost identical. It can be seen from the curve, that the change in weight was the fastest when the specimen was alkaline. Carbonation clearly retarded water absorption. The effect was bigger when accelerated carbonation was used.

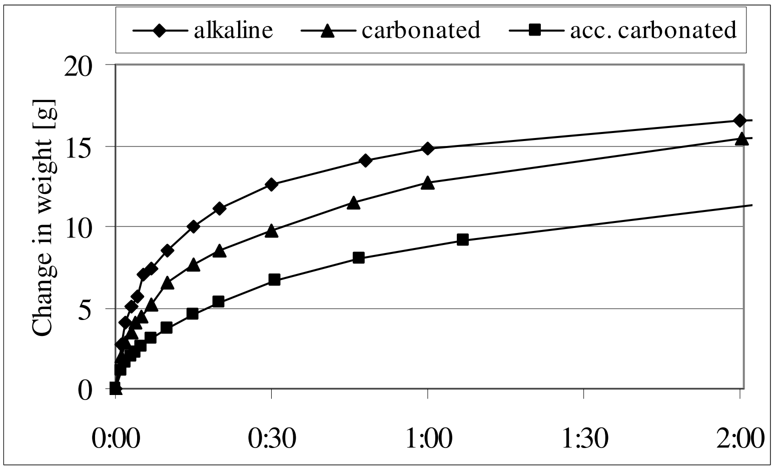

Figure 15 – The curve of water absorption.

The water absorption coefficients of each specimen after 1 and 5 minutes are presented in Figures 16 and 17. The carbonated and the alkaline surfaces are reached from same pieces of concrete (Fa…Vd) by removing concrete from the carbonation zone. The accelerated carbonated surface is the alkaline surface after carbonation.

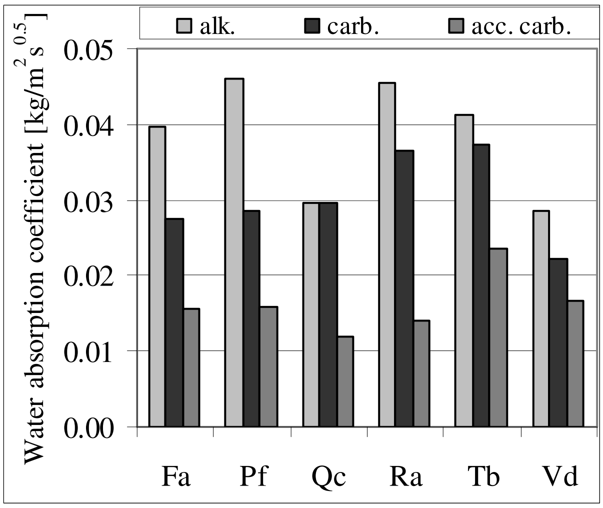

Figure 16 – The water absorption coefficients recorded after 1 minute.
(alk.=alkaline, carb.=carbonated in 0.04 %-vol CO_2, acc. carb.=accelerated carbonated in 4 %-vol CO_2).

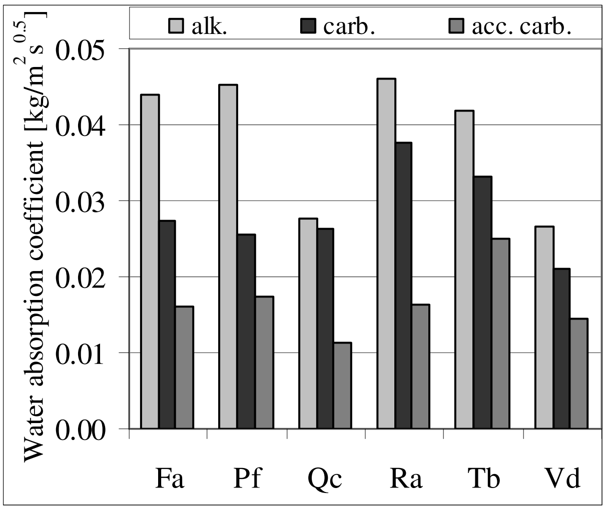

Figure 17 – The water absorption coefficients recorded after 5 minutes.
(alk.=alkaline, carb.=carbonated in 0.04 %-vol CO_2, acc. carb.=accelerated carbonated in 4 %-vol CO_2).

After 1 hour the water front had reached the alkaline parts of the specimens and the water absorption coefficients of carbonated specimens were higher.

4. DISCUSSION

The corrosion rate of specimens made of Mix 1 was slower in accelerated carbonated specimens than in naturally carbonated specimens. In the 1st test, the mean rate of accelerated carbonated specimens was 34 – 38 % smaller than in normally carbonated specimens. In the 2nd test the mean rate of accelerated carbonated specimens ended up to be 15 – 20 % smaller than in normally carbonated specimens.

During the 1st test the corrosion rates increased during the tests because the corrosion was starting. Immediately in the beginning of the 2nd test the corrosion rates reached their maximum and decreased by time possible due to depletion of oxygen.

The corrosion in specimens made of Mix 2 was much faster than in specimens made of Mix 1. In the 1st test, the mean rate of normally carbonated specimens was 3-4 times faster during the first 6 hours and later 2-3 times faster than in accelerated carbonated specimens. In the 2nd test the difference was smaller: mean rate of normally carbonated specimens was 1.2-2 times of that in accelerated carbonated specimens.

Monitoring of specimens 2 indicated also that corrosion is faster in naturally carbonated specimens: the mean corrosion rate in accelerated carbonated specimens was 35 % slower than in naturally carbonated specimens.

The water vapour permeability of the specimens increased during carbonation. This is contradictory with the common understanding, but also corresponding results are being introduced /5/. There were no significant differences between accelerated and normally carbonated specimens. The water vapour permeability of accelerated carbonated specimens was 16 % smaller than in normally carbonated specimens. The scatter of the results was quite wide which may have been caused by leakages from the cups or by measuring errors. In small number of specimens even one difference may affect the results remarkable.

According to the water absorption tests, the carbonation makes the concrete denser. This effect is more pronounced in accelerated carbonated specimens than in naturally carbonated ones. The water absorption coefficients of accelerated carbonated parts were approximately 40 % smaller than in naturally carbonated parts during the first 5 minutes. It was impossible to perform the tests to all groups of specimens in the same time because of the frequent weighing. That's why the results may have been affected for example by the drying of the specimens and different initial moisture content.

5. CONCLUSIONS

The data of this study shows that there are some differences between natural and accelerated carbonation.

Carbonation reaction generally causes a reduction in porosity. According to this study the effect may be more pronounced when using accelerated methods. The water vapour permeability and water absorption coefficients of accelerated carbonated specimens were smaller than in normally carbonated specimens. The effect was also observed as differences in resistivity: The corrosion rate was 15-50 % smaller in accelerated carbonated specimens (4 %-vol CO_2) than in naturally carbonated specimens (0.04 %-vol CO_2).

According to the results of this study, the corrosion rate results received with accelerated carbonation may be 15 - 40 % smaller than in naturally carbonated concrete. This should be taken into consideration when using accelerated carbonation for studying corrosion. However accelerated carbonation enables corrosion of steel to start much earlier which is a remarkable benefit when studying corrosion of steel.

REFERENCES

1. Parrot L.J., “A review of carbonation in reinforced concrete”, Cement and Concrete Association, Wexham Springs, 1987.
2. Bakker R., “Initiation period,” Schiessl P. (editor), Corrosion of steel in concrete, Chapman and Hall, London, 1988
3. Claisse et al., ”Permeability and Pore Volume of Carbonated concrete” European concerted action, Final report, Brussels, 1997
4. Richardsson M.G., “Carbonation of reinforced concrete: Its Causes and Management” Civil Engineering Department, Ireland, 1988
5. Häkkinen T., “Influence of high slag content on the basic mechanical properties and carbonation of concrete” VTT Building Materials Laboratory, Espoo, 1993 (in Finnish)
6. Tuutti, K., “Corrosion of Steel in Concrete” Swedish Cement and Concrete Institute, Stockholm, 1982
7. Dunster, A.M., “Accelerated carbonation testing of concrete” BRE, Information paper, December, 2000

8. Sulankivi H., Tiililaatan vaikutus betonin karbonatisoitumiseen, diplomityö, Tampere, 1993 (in Finnish)
9. Neville, A.M., “Properties of Concrete” Longman Scientific & Technical, Singapore, 1988
10. Papadagis V.G. et al., “Fundamental Modelling and Experimental Investigation of Concrete Carbonation” ACI Materials Journal, V. 88, NO. 4, July-August, 1991
11. Page C. L., “Basic Principles of Corrosion” Schiessl P. (editor), Corrosion of steel in concrete, Chapman and Hall, London, 1988
12. Mattila J., “On the Durability of Cement-Based Patch Repairs on Finnish Concrete Facades and Balconies” Doctoral thesis, Tampere University of Technology, Structural Engineering, Tampere, 2003
13. Anon., “Standard test method for half-cell potentials of uncoated reinforcing steel in concrete” ASTM C876-91, The American Society for Testing and Materials, 1999
14. COST 509, Corrosion and protection of metals in contact with concrete, European concerted action, Final report, Brussels, 1997
15. Andrade C., “Measurement of Polarization Resistance on-site” COST Action 521, Corrosion of steel in reinforced concrete structures, Final report, 2003

Microstructure-Rheology: Thixotropy and workability loss

Jon E. Wallevik
Dr.ing., Senior research engineer
Icelandic Building Research Institute
Keldnaholti
IS-112 Reykjavik
Island
E-mail: wallevik.j@ibri.is

ABSTRACT

This paper presents a new rheological equation that simulates thixotropic behavior of cement paste. This new material model is based on previous work done by Hattori and Izumi [1,2], where the coagulation rate and dispersion rate of the cement particles is assumed to play the dominating role in generating thixotropic behavior. This model is named the *modified Hattori-Izumi theory* and is based on the so-called microstructural approach [3]. In addition to this theory, other older and well-known material models are also tested for comparison. In this comparison, it is shown that the modified Hattori-Izumi theory simulates thixotropic behavior much better. Comparing experimental data with model prediction does the evaluation of the different models. The experimental data is attained from the ConTec Viscometer 4 [4]. The model prediction is calculated with the software Viscometric-ViscoPlastic-Flow$^{©}$ [5].

Since the modified Hattori-Izumi theory is on a scientific frontier, there is still some distance to its direct application in the "real concrete world". Nevertheless, this theory introduces a model of the thixotropic behavior and workability loss. More precisely, this theory connects rheological behavior to the structural changes of cement particles that can undergo a reversible- and a permanent coagulation. For the future, this can be a valuable tool, for example when comparing different cement types or examine different admixture effect in more detail. This would provide an additional help and a better know-how in solving problems that might occur at building site.

Due to the complexity of the main theory presented here, all details cannot be presented in a single paper. However, for the interested reader, a complete description of the theory can be found in [5].

Key words: Rheology; Thixotropy; Workability loss; Microstructural approach

1. INTRODUCTION

The interest in thixotropic phenomena is nearly as old as modern rheology [6]. An increasing number of real materials have been found to show these effects. Also, they have been applied in various industrial applications. The term thixotropy was originally coined to describe an isothermal reversible, gel-sol (i.e. solid-liquid) transition due to mechanical agitation [6]. According to Barnes et al. [7], the accepted definition of thixotropy is "… *a gradual decrease of the viscosity under shear stress followed by a gradual recovery of structure when the stress is removed…*". Additional definitions of thixotropy are given in [3]. In this last-mentioned citation, the term viscosity denotes *apparent viscosity* η. In theoretical rheology the term η is also called the *shear viscosity.*

The amount of theoretical literature on the above-mentioned time-dependent material is limited [7]. However, comprehensive review articles have been written on the subject, done by Mewis [6] and Barnes [3]. A shorter review is recently given in Mujumdar et al. [8] and in a newly published textbook by Tanner and Walters [9]. In these literatures, the various approaches used to measure thixotropy are represented. For example, one approach mentioned is by measuring the torque T under a linear increase and then decrease in rotational frequency f_o of the rotating part of the viscometer (f_o is in revolutions per second or [rps]). If the test sample is thixotropic, the two torque curves produced do not coincide, causing rather a hysteresis loop. While hysteresis loops are useful as a preliminary indicator of thixotropic behavior, they do not provide a good basis for quantitative treatments [3,10]. However, an attempt can be made to quantify thixotropic behavior from such torque curve by its integration [3,10,11]. Another possible approach to study thixotropic behavior is by monitoring the decay of measured torque from an initial value T_o to an equilibrium value T_e with time t, at a constant rotational frequency f_o [10]. In some cases, a simple exponential relationship can be found, but other and more complicated relationships may also exist. For example, Lapasin et al. [12] make use of the above approach on cement pastes, using three different types of functions, however all more complicated than the simple exponential form. Nevertheless, a material model created by this approach is very limited because the corresponding apparent viscosity function η can only be valid when only one constant rotational frequency f_o is applied to each rheological experiment. Considering an apparent viscosity function η extracted from such experiment and then using it in another experiment of more complicated shear history, will turn out to be almost impossible. Hence, such viscosity function will not represent a *true* rheological picture of the test material. As will be demonstrated in this paper, a *true* viscosity function must at least depend on (fading) memory information of both shear rate $\dot{\gamma}$ (related to dispersion rate of the cement particles) and of coagulation rate H.

In this paper, the analysis of thixotropic behavior consists of measuring torque $T = T(t)$ as a function of time t, under complex rotational frequency conditions $f_o = f_o(t)$ shown in the left illustration of Figure 2. During such condition, the processes of structural breakdown and structural rebuild (or recovery) are simultaneously present in each experiment. If both processes are occurring at equal rate, a state of microstructural equilibrium is reached. The challenge is to create a material model η that is based on the microstructural approach and can simulate the measured rheological behavior of the cement paste under arbitrary and very complex shear rate conditions. With a good apparent viscosity function $\eta = \eta(\dot{\gamma},t,\ldots)$ that is used in the numerical simulation, the computed torque T_c should be able to overlap the measured torque T. With such satisfactory material model, a better idea of what controls the rheological behavior of the cement-based material can be attained. Also, such a connection of the rheological behavior to the structural changes governing thixotropy can provide additional insight and a better understanding of the admixture performance for example relative to potential formwork pressure and workability loss.

The viscometer used in the experiment is the ConTec Viscometer 4 [4]. It is a coaxial cylinders viscometer that has a stationary inner cylinder (of radius R_i = 85 mm) that measures torque T, and a rotating outer cylinder (of radius R_o = 101 mm). The height of the inner cylinder is h = 116 mm. Shearing from the bottom part of the viscometer is filtered out by a special means [4]. The left illustration of Figure 1 shows a simulated flow inside the ConTec Viscometer 4, while the right illustration shows a schematic presentation of the viscometer.

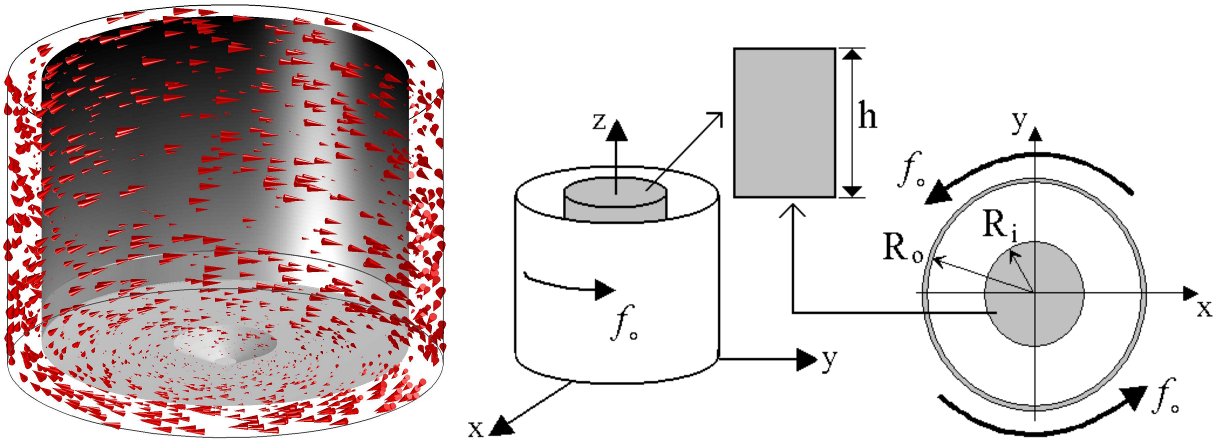

Figure 1 – To the left: Computed flow inside the ConTec Viscometer 4 [5]. *To the right: Schematic representation of the viscometer. The inner cylinder* (R_i) *is stationary and measures the applied torque T from the cement paste. The outer cylinder* (R_o) *rotates at pre-determined rotational frequencies* $f_\mathrm{o} = f_\mathrm{o}(t)$*, shown in the left illustration of Figure 2.*

The numerical software used is named Viscometric-ViscoPlastic-Flow©. This software is freely available in [5]. It is a finite difference model based on the ADI technique (Alternating Direction Implicit). It is designed for time-dependent (transient) and time-independent (steady state) viscoplastic materials. In fundamental terms, the pre-mentioned software solves the Newton's second law $m\, d\mathbf{v}/dt = \mathbf{F} + m\,\mathbf{g}$ inside the ConTec Viscometer 4, where m is the fluid element mass, $\mathbf{v} = \mathbf{v}(\mathbf{x},t)$ is its velocity, $\mathbf{g}$ is gravity and $\mathbf{F}$ is the sum of surface forces applied to the fluid element from its surroundings (see [5], pp.11-16, pp.155-157). The term $\mathbf{x} = (x,y,z)$ is the spatial coordinates. A different apparent viscosity η gives a different force contribution $\mathbf{F} = \mathbf{F}(\eta)$, which again gives a different velocity profile $\mathbf{v} = \mathbf{v}(\mathbf{x},t)$. This again results in a different computed torque $T_\mathrm{c} = 2\pi R_\mathrm{i}^2 h \eta \dot{\gamma}$, because the shear rate is dependent on the velocity $\mathbf{v}$ (meaning $\dot{\gamma} = \dot{\gamma}(\mathbf{v})$). More precisely, the shear rate is calculated according to Equation (1.1) [13, 14, 15].

$$\dot{\gamma} = \sqrt{2\,\dot{\varepsilon} : \dot{\varepsilon}} \tag{1.1}$$

The term $\dot{\varepsilon}$ is the strain rate tensor and is given by Equation (1.2) [13, 14, 15].

$$\dot{\varepsilon} = \left(\nabla\mathbf{v} + (\nabla\mathbf{v})^\mathrm{T}\right)/2 \tag{1.2}$$

Both the shear rate and the strain rate tensor have the unit of s^{-1}. ∇ is the gradient operator and $(\nabla\mathbf{v})^T$ is the transpose of the gradient velocity tensor $\nabla\mathbf{v}$. With Equations (1.1) and (1.2), the shear rate $\dot{\gamma}$ is not only dependent on the geometry (R_i,R_o,h) and on the rotational frequency (f_o) of the viscometer, but also on the rheological parameters of the test material. This is because the shear rate $\dot{\gamma}$ is dependent on velocity $\mathbf{v}$, which is again dependent on the force $\mathbf{F} = \mathbf{F}(\eta)$ (c.f. Newton's second law). This approach is very important when calculating the correct shear rate inside a fluid that has a yield value (i.e. of a viscoplastic material). This type of shear rate calculation is well known in theoretical rheology and dates back at least to 1947 [14]. However, because of how this type of shear rate calculation severely complicates the analysis of the test material, the approach is not popular although it is extremely important (see pp.232-234 in [5]). Furthermore, this type of shear rate calculation is unknown to many.

The results produced by the software Viscometric-ViscoPlastic-Flow© have been demonstrated to be accurate. First of all, the numerical results produced by the software have been tested against known solutions existing in the literature. Also, issues like consistency, convergence, numerical convergence and stability have been dealt with, to verify a good numerical quality. For further information about this issue, see [5], pp.163-164, pp.177-203.

2. EXPERIMENTAL

2.1 Mix Design

The water-cement ratio used for the cement paste is w/c = 0.3. The amount of superplasticizer is 0.5% solids by weight of cement (sbwc) of Suparex M40. This product is a naphthalene (SNF), produced by Hodgson Chemicals Ltd. The volume of the test sample is about three liters, meaning that about 4.80 kg of Norcem Standard Cement (CEM I 42.5R acc. to EN 197-1:2000) and 1.44 kg of water is applied to each batch.

2.2 Mixing procedure

A Hobart AE120 mixer was used for mixing the cement paste. The agitator and the attachment (i.e. the whips) have the following speed settings:

1. *Low*: 107 and 61 rpm;
2. *Intermediate*: 198 and 113 rpm and
3. *High*: 361 and 205 rpm.

The agitator rotates clockwise and the attachment rotates counterclockwise. The attachment is blade shaped (like an open shield).

The fact that the test sample consisted of only pure cement paste, resulted in a reduced reproducibility (*reproducibility = reproduction of rheological result of different batches, of the same mix-design*). After testing different mixing procedures to seek a better reproducibility, the following one was selected:

1. *Between 0 and 3 minutes*: Mixing of cement and water at speed 1. Most of the cement particles are more or less moistened within the first 60 seconds.

2. *Between 3 and 6 minutes*: Hand mixing and resting.
3. *Between 6 and 10 minutes*: Mixing at speed 2 (mixing at speed 3, resulted in too much splashing in most cases).
4. *Between 10 and 11 minutes*: Check with hand mixing, if the cement paste is homogeneous.

2.3 Measuring Procedure

At 12, 42, 72 and 102 minutes after the initial water addition, a rheological measurement with the ConTec Viscometer 4 is performed. Immediately after each measurement, a remixing by hand is done to ensure homogeneous mixture. A complete rest period applies for the test material prior to any data logging in the coming measurement. The rest period is about 29 minutes and was considered to be sufficient for the test sample to gain a large coagulation state at the start of the next measurement. No remixing with the Hobart mixer was applied between measurements. Since the objective is to investigate thixotropic behavior of the cement paste, it would be pointless to use the Hobart mixer to disperse the coagulated cement particles and break up the structure that the viscometer is supposed to measure.

As mentioned just above, a rheological measurement is made at 12, 42, 72 and 102 minutes. However, in the current paper, only one of these four results is shown, analyzed and discussed. This is the measurement conducted at 72 minutes after water addition. For the interested reader, all four results are available in [5]. Each measurement is made with the ConTec Viscometer 4 and begins at the (experimental) time $t = 0$ and ends at $t = 50$ s.

2.4 Rotational frequency and measured torque

The rotational frequency f_0 [rps] of the outer cylinder (see Figure 1) applied in the experiment and also used in the numerical simulation, is shown in the left illustration of Figure 2.

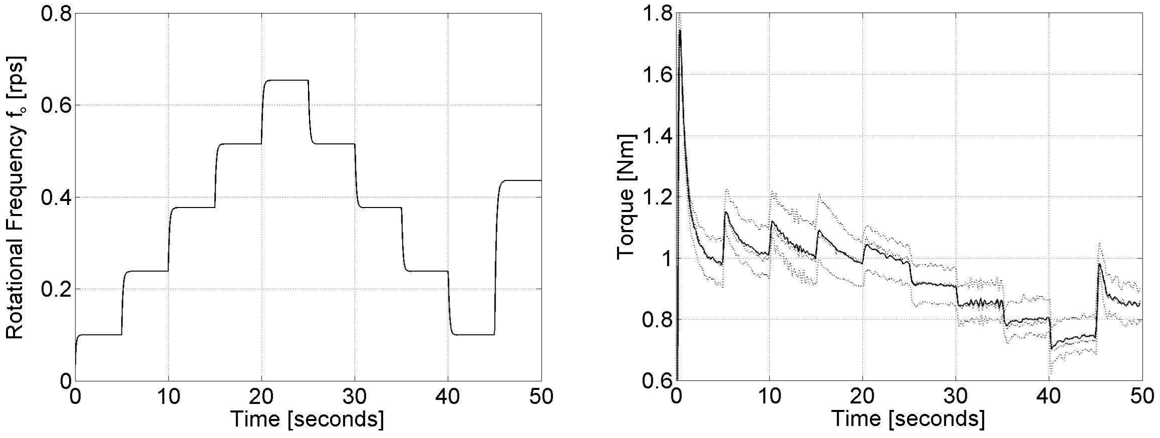

Figure 2 – To the left: The applied rotational frequency f_0 as a function of time t. To the right: The experimental result at 72 minutes after water addition. The dotted lines represent the three repeated batches and the solid line is the average of these three results.

In this work, three repeated batches are mixed and tested to examine reproducibility. In the right illustration of Figure 2, the corresponding rheological results are shown with a dotted line. All these three results apply at 72 min after water addition. To filter out the effect of random experimental error from thixotropic material behavior, the average of these three results is used to represent the rheological behavior of the test material. This average is shown in the same figure with a solid line. The average line is also shown in Figures 3, 4, 5 and 7 and then with a dashed line.

3. TESTING OF DIFFERENT THIXOTROPIC MATERIAL MODELS

Several selected material models are tested in the attempt to reproduce the experimental result (i.e. the solid line) shown in the right part of Figure 2. This is done to examine the quality of each model. Initially, the modified vom Berg equation is tested. It is modified by Lapasin et al. [12]. Thereafter in Section 3.2, the modified Shangraw equation is tested. The modification is also made by Lapasin et al. [12]. In Section 3.3, the original Hattori-Izumi theory [1,2] is investigated and in the end (Section 3.4) its modification [5] is tested.

3.1 The vom Berg equation (modified by Lapasin et al.)

In the original literature [12], the vom Berg model is presented in terms of shear stress τ. In the current paper, it is rather presented in terms of apparent viscosity η. Those two presentations are equal to one another, since by multiplying the apparent viscosity η with the shear rate $\dot{\gamma}$, the shear stress presentation of the material model is attained (i.e. $\tau = \eta\dot{\gamma}$). The material model suggested by vom Berg is given by Equation (3.1).

$$\eta = \frac{\tau_{\mathrm{f}} + A \cdot \operatorname{arcsinh}(\dot{\gamma}/\mathrm{C})}{\dot{\gamma}} \tag{3.1}$$

The term τ_{f} is the yield value (called the *yield stress* in the original paper) and $\dot{\gamma}$ is the shear rate. The two terms *A* and *C* are material constants. The modification suggested by Lapasin et al. [12] replaces the constant *A* with a function shown with Equation (3.2).

$$A = A_0 + (A_1 - A_0)\,\lambda \tag{3.2}$$

The terms A_0 and A_1 are additional material constants. The term λ is known as *structural parameter* [12] and is given by Equation (3.3).

$$\lambda = \exp\left(\frac{-\dot{\gamma}\,t}{a + b\,\dot{\gamma}}\right) \tag{3.3}$$

The two terms *a* and *b* are also material constants and *t* is time. By using Equations (3.1) to (3.3) in the numerical simulation, it became impossible to reproduce the experimental result shown in the right illustration of Figure 2. A vide variety of different values τ_{f}, *C*, A_0, A_1, *a* and *b* were tested in this experiment by trial and error. An example of such numerical result is shown in Figure 3 with a solid line. Also shown in this figure, is the experimental result (dashed line) and the rotational frequency used (dashed dotted line). These two last-mentioned lines are also shown in Figure 2. Note that the rotational frequency line in Figure 3 is a relative line, not showing the absolute values (the absolute values are however shown in Figure 2).

In the current work, it became clear that it is only possible to simulate a part of the experimental data with the modified vom Berg theory. I.e. it is possible to set the values of τ_f, C, A_0, A_1, a and b such that a part of the experimental result is reproduced. However, with these six values fixed, the rest of the experimental data cannot be simulated. For the particular example shown in Figure 3, the following values are used: $\tau_f = 130$ Pa, $C = 4$ s^{-1}, $A_0 = 30$ Pa, $A_1 = 230$ Pa, $a = 1$ and $b = 1$ s. These values are chosen in the attempt to reproduce the first part of the experimental data as much as possible.

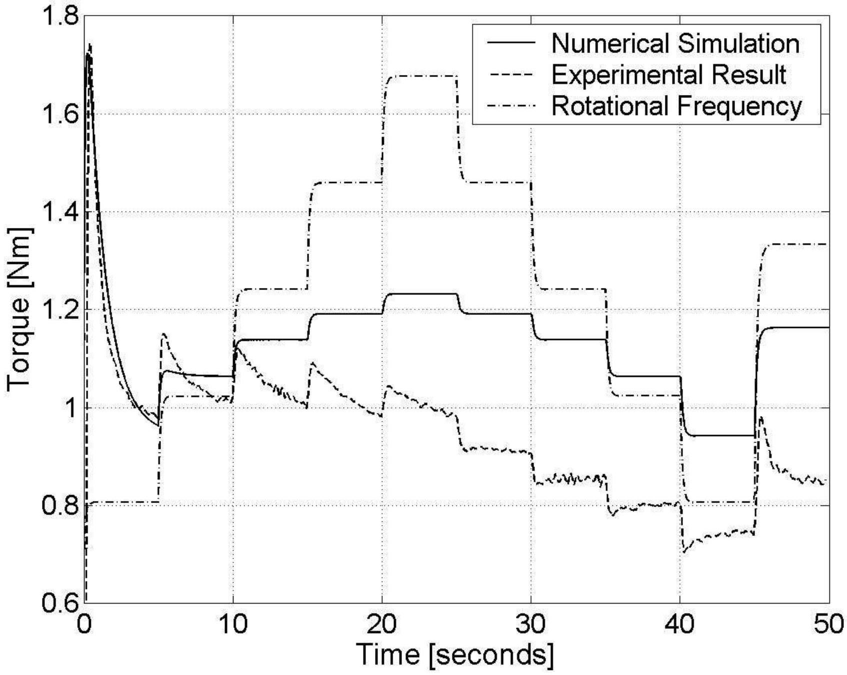

Figure 3 – Numerical result when using the vom Berg equation (modified by Lapasin et al.).

3.2 Shangraw equation (modified by Lapasin et al.)

In this paper, the Shangraw equation is presented in terms of apparent viscosity η rather than in terms of shear stress τ (see the discussion in Section 3.1). The material model suggested by Shangraw is given by Equation (3.4).

$$\eta = \eta_\infty + \frac{\tau_o + \alpha_1[1 - \exp(-\alpha_2\dot{\gamma})]}{\dot{\gamma}} \tag{3.4}$$

The terms τ_o and η_∞ are called the yield stress (i.e. yield value) and dynamic viscosity in the original literature [12]. The two terms α_1 and α_2 are material constants. The modification suggested by Lapasin et al. [12] is replacing the constant α_1 with a function given by the following equation

$$\alpha_1 = \alpha_{10} + (\alpha_{11} - \alpha_{10})\,\lambda \tag{3.5}$$

where the terms α_{10} and α_{11} are additional material constants. The term λ is the same structural parameter as shown in Equation (3.3) [12].

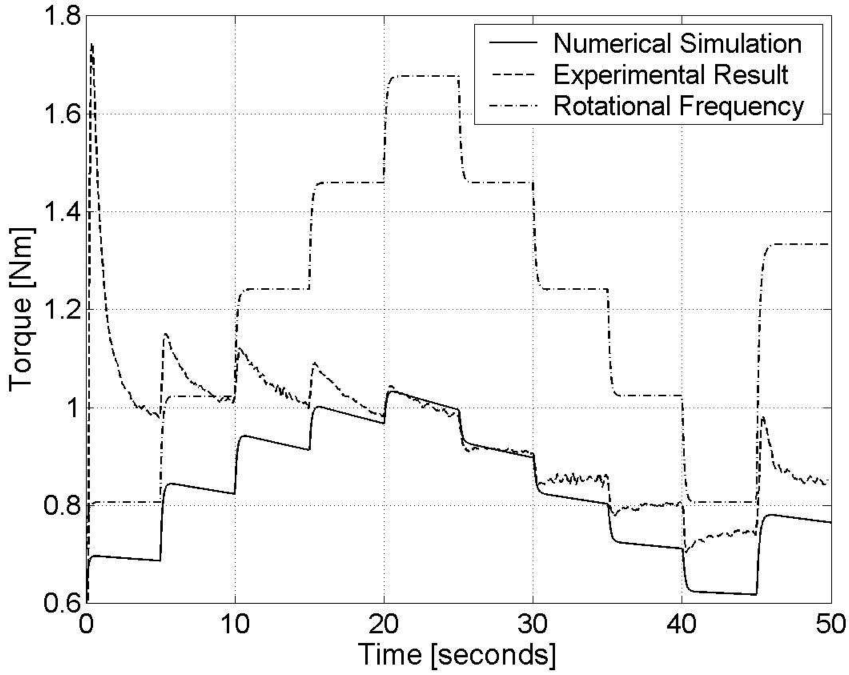

Figure 4 – Numerical result when using the Shangraw equation (modified by Lapasin et al.).

By using Equations (3.4) and (3.5) (as well as Equation (3.3)) in the numerical simulation, it became impossible to reproduce the whole experimental result. A vide variety of different values τ_0, η_∞, α_{10}, α_{11}, α_2, a and b were tested in this experiment by trial and error. Figure 4 shows an example of a result when using the modified Shangraw equation (the solid line). Just as applies in Section 3.1, it was only possible to simulate a part of the experimental data. For the result shown in Figure 4, the material parameters τ_0, η_∞, α_{10}, α_{11}, α_2, a and b are set to such that the middle part of the experimental data is reproduced as much as possible. However, with these seven values fixed, the simulation cannot reproduce the rest of the experimental data. The following values are used in the last-mentioned figure: $\tau_0 = 90$ Pa, $\eta_\infty = 0.002$ Pa·s, $\alpha_{10} = 10$ Pa, $\alpha_{11} = 220$ Pa, $\alpha_2 = 0.03$ s, $a = 40$ and $b = 50$ s.

3.3 The original Hattori-Izumi theory

The apparent viscosity function of Hattori and Izumi [1,2] is given by Equation (3.6).

$$\eta = B_3\, J_t^{2/3} + \{\text{other less relevant terms}\} \approx B_3\, J_t^{2/3} = B_3\, n_3^{2/3}\, U_3^{2/3} \tag{3.6}$$

The term J_t represents the number of junctions (or connections) between the primary cement particles, per unit volume (i.e. this term has the physical unit of [m^{-3}]). With *primary cement* *particles*, it is meant the cement particles that are small enough to be influenced by the total potential energy (*which is the sum of van der Waals attraction, electrostatic repulsion and steric hindrance*) and can therefore interact with each other by coagulation and dispersion (for further reading about this issue, see [5], pp.38-47). The number of such particles per unit volume is represented with the term n_3. The term U_3 is an *indirect microstructural parameter* and is related to the *direct microstructural parameter* J_t with the following relationship $J_\mathrm{t} = n_3U_3$. With coagulation of the cement particles ($H > 0$) the value of J_t increases, but with dispersion ($\dot{\gamma} > 0$) this value decreases. The term B_3 is a so-called friction coefficient with the physical unit of [N•s]. The coagulation state U_3 at time t is calculated by Equation (3.7) [1,2].

$$U_3 = \frac{J_\mathrm{t}}{n_3} = \frac{U_\mathrm{o}(\dot{\gamma}\,H\,t^2+1)+H\,t}{(H\,t+1)(\dot{\gamma}\,t+1)} \tag{3.7}$$

As before, the variable t is time and $\dot{\gamma}$ is the shear rate. The term H is the coagulation rate constant (with the unit of [s^{-1}]) and U_o is the coagulation state at $t = 0$. That is $U_\mathrm{o} = (J_\mathrm{t}|_{\mathrm{t}=0})/n_3$, where the term $J_\mathrm{t}|_{\mathrm{t}=0} = J_\mathrm{o} = n_3U_\mathrm{o}$ describes the number of junctions between the primary cement particles, at the beginning of an experiment $t = 0$. The above equation describes how the number of junctions (or contacts) between primary cement particles is changing, because of coagulation, dispersion and re-coagulation.

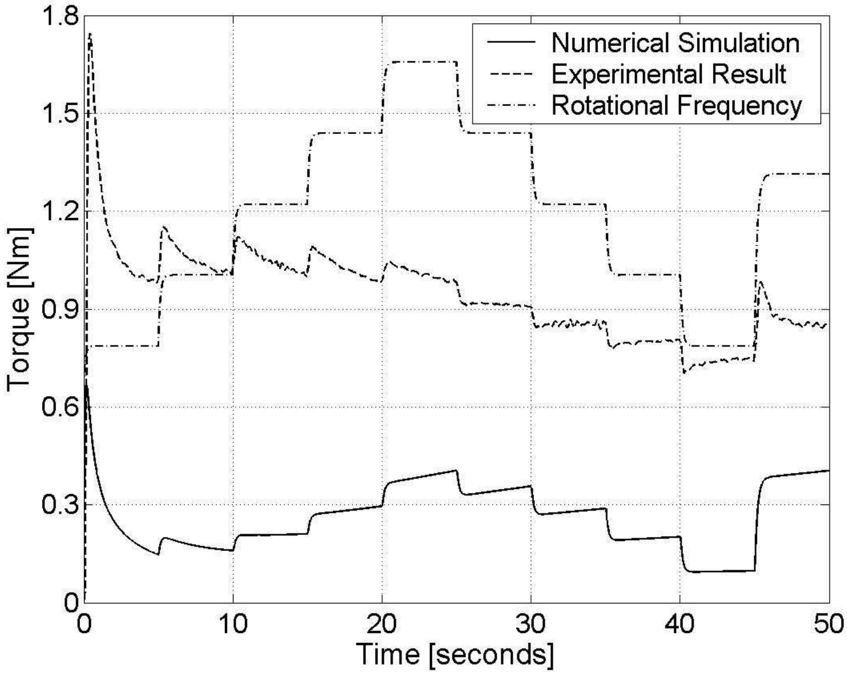

Figure 5 – Numerical result when using the original Hattori-Izumi theory.

Using Equations (3.6) and (3.7) in the numerical simulation, a result like what is shown in Figure 5 emerges (the solid line). Such type of torque profile is never observed experimentally in this work. The values used in this case are as follows $B_3\,n_3^{2/3} = 45$ N•s•m^{-2}, $U_\mathrm{o} = 1$ and $H = 0.0005\ \mathrm{s}^{-1}$. A vide variety of other values were also tested (by trial and error), but without any success. In Section 3.4, some necessary modifications applied to Equations (3.6) and (3.7) are described. Rather than being based on pure theoretical approach, much of these modifications are based on (semi) empirical considerations and intuition. The modifications are made with the objectives to calculate a torque T_c that is identical or very similar to the measured torque T.

3.4 Modified Hattori-Izumi Theory

The material model of the modified Hattori and Izumi theory [5] is given by Equation (3.8).

$$\eta = \left(\mu + \frac{\tau_o}{\dot{\gamma}}\right) + \left(\tilde{\mu} + \frac{\tilde{\tau}_o}{\dot{\gamma}}\right) \tag{3.8}$$

The two terms τ_o and μ are the well-known yield value and plastic viscosity, while $\tilde{\tau}_o$ and $\tilde{\mu}$ are their thixotropic counterparts. As shown with Equations (3.9) and (3.10), both the thixotropic plastic viscosity $\tilde{\mu}$ and the thixotropic yield value $\tilde{\tau}_o$ are dependent on $U_3^{2/3}$. This is based on the relationship shown with Equation (3.6).

$$\tilde{\mu} = \xi_1 U_3^{2/3} \tag{3.9}$$
$$\tilde{\tau}_o = \xi_2 U_3^{2/3} \tag{3.10}$$

Although determined by empirical means, the two terms ξ_1 and ξ_2 are material parameters, depending among other factors, on the surface roughness of the cement particles and phase volume Φ. Also included in ξ_1 and ξ_2, is the interaction between the smaller (coagulating - dispersing) cement particles and the larger cement particles (that mostly interact with a hard sphere collision factor), as well as the contribution from the corresponding admixture and the pore water in-between (see also [5] about this issue, pp.21-28, pp.127-128). The coagulation state U_3 is now calculated by Equation (3.11) instead of by Equation (3.7).

$$U_3 = \frac{J_t}{n_3} = \frac{U_o(\Gamma\,\Theta + 1) + \Theta}{(\Theta + 1)(\Gamma + 1)} \tag{3.11}$$

The above equation is based on Equation (3.7). More precisely, by replacing the two terms $\dot{\gamma}\ t$ and $H\ t$ in the last-mentioned equation, with the memory modules Γ and Θ, Equation (3.11) is attained. These two terms are defined by Equations (3.12) and (3.13) (see [5], pp.171-172, pp.209-210).

$$\Gamma(\mathbf{x}, t) = \int_0^t \alpha(t - t')\ \dot{\gamma}(\mathbf{x}, t')\ dt' \tag{3.12}$$

$$\Theta(\mathbf{x}, t) = \int_0^t \beta(t - t')\ H(\dot{\gamma}, t')\ dt' \tag{3.13}$$

The two terms α and β are fading memory functions and t' is earlier time. As before, the term $\mathbf{x}$ represents the spatial coordinates, meaning $\mathbf{x} = (x,y,z)$ (the coordinates x, y and z are shown in Figure 1). With the application of the two above equations, the apparent viscosity Equation (3.8) now remembers its past. That is, it remembers its past shear rate history and its past coagulation rate history. Apparently, with the requirement of Equations (3.12) and (3.13), the history of shear rate and coagulation rate are important, when considering the thixotropic response of cement pastes.

It is interesting to note that when all the (primary) cement particles are fully dispersed, meaning $U_3 = 0$, Equation (3.8) returns to its pure Bingham form:

$$\eta = \left(\mu + \frac{\tau_o}{\dot{\gamma}}\right) \longleftrightarrow \tau = \eta\dot{\gamma} = \mu\,\dot{\gamma} + \tau_o \tag{3.14}$$

The first part of Equation (3.14), shows the Bingham equation in terms of apparent viscosity, while the latter part shows it in terms of shear stress τ.

In the modified Hattori-Izumi theory [5], it is assumed that basically two kinds of coagulation exist. The first type is the *reversible coagulation*, where two coagulated cement particles can be separated (i.e. dispersed) again for the given rate of work available to the cement paste (the rate of work, or power, is provided by the engine of the viscometer). The number of connections between cement particles that are in reversible coagulated state is represented with the term J_t and calculated according to Equation (3.11). As shown with Equations (3.9) and (3.10), the thixotropic plastic viscosity and yield value are dependent on the number of reversible connections $J_t = n_3U_3$ that exists between the cement particles. In Figure 6, the white cement particles demonstrate a reversible coagulation.

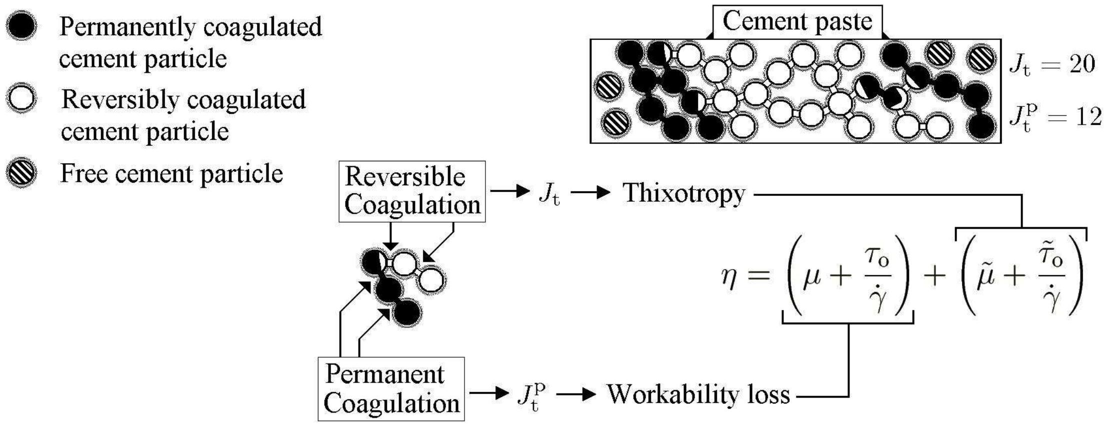

Figure 6 – Relationship between Equation (3.8) and the two terms J_t and J_t^p.

The second type of coagulation is the *permanent coagulation*, where the two cement particles cannot be separated for the given power available. In [5], its number is represented with J_t^p (*the reason for a permanent coagulation might be (for example) due to a damaged plasticizing polymer between the two corresponding cement particles*). Hence, the total number of junctions in the cement paste is $J_t^{tot} = J_t^p + J_t$. In Figure 6, the black cement particles demonstrate a permanent coagulation. The number J_t^p is always gradually increasing (i.e. cannot reduce), while J_t can both increase and decrease.

Just as the thixotropic yield value $\tilde{\tau}_o$ and plastic viscosity $\tilde{\mu}$ depends on the number of reversible junctions J_t, the yield value τ_o and plastic viscosity μ could be considered to depend on the permanent junction number J_t^p in similar manner as shown with Equations (3.9) and (3.10). As such, one could consider that permanent coagulation J_t^p contributes to the workability loss, while reversible coagulation J_t contributes to thixotropic behavior. This correlation is shown in Figure 6. Hence, the physical relationship between thixotropy and workability loss might be closer than one could imagine at first sight.

Figure 7 shows the numerical result when using the modified Hattori-Izumi theory. As shown, this theory can reproduce the measured torque much better relative to what is shown in any of the Figures 3, 4 and 5. The values used in this simulation are: μ = 0.5 Pa•s, τ_o = 110 Pa, ξ_1 = 67.5 Pa•s, ξ_2 = 22.5 Pa and U_o = 1. These values are attained by the method of trial and error, to give the best overlap between the measured torque T and the computed torque T_c (this approach was also used in Sections 3.1, 3.2 and 3.3). These values are not just a coincidence, but rather correspond to the cement paste rheological response as explained with the modified Hattori-Izumi theory (for further reading about this important issue, see [5], p.215). As indicated above, the degree of overlapping shown in Figure 7, is impossible to produce with any of the theories presented in Sections 3.1, 3.2 and 3.3.

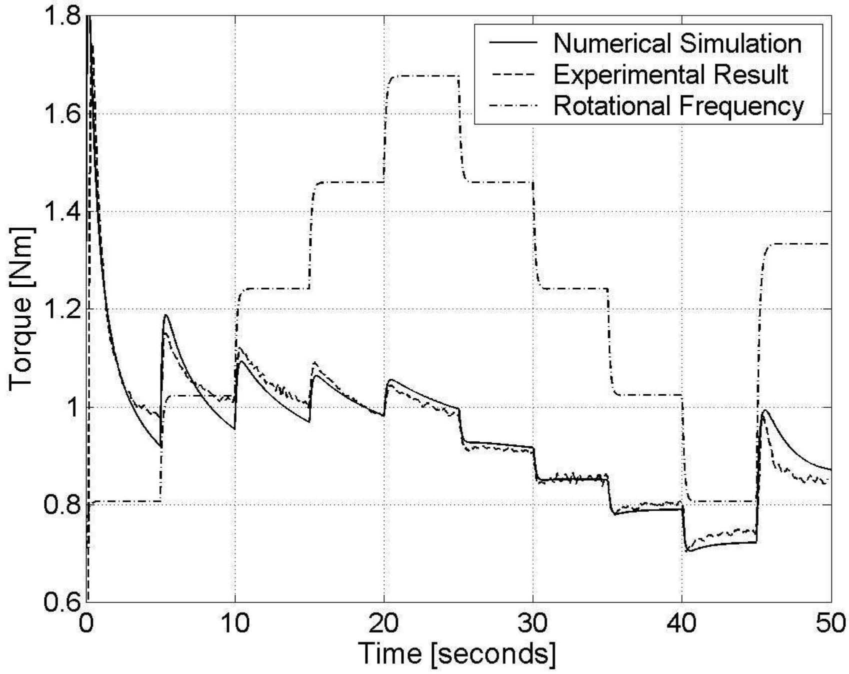

Figure 7 – Numerical result when using the modified Hattori-Izumi theory.

In the original Hattori-Izumi theory [1,2], it is assumed that the coagulation rate H is a constant, only dependent on Brownian motion. Such assumption cannot hold for non-zero shear rate condition. Under such condition, the stirring ($\dot{\gamma} > 0$) causes the cement particles to be thrown together at larger rate than the normal diffusion rate, resulting in increased coagulation [16] (see also [5], pp.45-47, pp.212-213). From this, it is clear that the coagulation rate coefficient is dependent on stirring, meaning $H = H(\dot{\gamma},t)$. After a large number of trials in simulating the measured torque, it became clear that the coagulation rate function had to have the functional form described with Equation (3.15). This equation is applies for the result shown in Figure 7.

$$H(\dot{\gamma}, t) = \frac{K(t)}{\dot{\gamma}^2 + l} \tag{3.15}$$

The term l in the above equation, is an empirical constant, equal to $l = 1\ \mathrm{s}^{-1}$. The function $K(t)$ is such that it holds a different value, depending on if the rotational frequency f_o is increasing or decreasing with time.

4. CONCLUSION

With the promising results shown in Figure 7, it has been demonstrated for one cement paste experiencing one shear history that the modified Hattori-Izumi theory can be used to adequately simulate the thixotropic torque response. As shown in Sections 3.1, 3.2 and 3.3, this was not possible with other selected models. In [5], the modified Hattori-Izumi theory is also used to simulate measured torque response of cement pastes using various types of lignosulfonates. There, in some cases, a complete match between the measured and the computed torque is gained, while in other cases, less acceptable results are gained. This indicates that the main theory presented here is not yet fully complete, although it gives satisfactory results in many cases.

In the modified Hattori-Izumi theory, thixotropy is basically governed by a combination of (reversible) coagulation, dispersion and re-coagulation of the cement particles. Also, in this theory, a close physical relationship is assumed between thixotropic behavior and workability loss. I.e. both processes are related to coagulation of the cement particles. More precisely, the former behavior depends on the reversible junction number J_t, while the latter on the permanent junction number J_t^p (see Figure 6). Of course, both thixotropy and workability loss are also dependent on other factors, for example like those mentioned below Equation (3.10).

ACKNOWLEDGMENTS

The work was carried out at the Norwegian University of Science and Technology, NTNU. This work was made possible by financial support from Borregaard LignoTech, Norway and the Research Council of Norway.

REFERENCES

1. Hattori, K., “Electrokinetics and Rheological Behavior of Cement Suspensions”, Department of Civil Engineering, Chuo University, Tokyo, Japan.

2. Hattori, K. and Izumi, K. (1991), “A New Viscosity Equation for Non-Newtonian Suspensions and Its Application, Rheology of Fresh Cement and Concrete”, Proceedings of The International Conference Organized by The British Society of Rheology, University of Liverpool, March 16-29 1990, Editor: Banfill, P. F. G., E & FN Spon, London, Great Britain.

3. Barnes, H. A. (1997), “Thixotropy - A Review”, Journal of Non-Newtonian Fluid Mechanics, Volume 70.

4. Wallevik, O. H. (1999), IBRI at Your Service, “The Rheology of Fresh Concrete”, The

Icelandic Building Research Institute (IBRI), Keldnaholti, IS-112 Reykjavik, Iceland.

5. Wallevik, J. E. (2003), “Rheology of Particle Suspensions, Fresh Concrete, Mortar and Cement Paste with Various Types of Lignosulfonates”. Ph.D. thesis, Department of Structural Engineering, The Norwegian University of Science and Technology. (download: www.ibri.is/rheocenter/download.html).

6. Mewis, J. (1979), “Thixotropy - A General Review”, Journal of Non-Newtonian Fluid Mechanics, Volume 6.

7. Barnes, H. A., Hutton, J. F. and Walters, K. (1989), “An Introduction to Rheology”, Elsevier Science B. V., Netherlands.

8. Mujumdar, A., Beris, A. N. and Metzner, A. B. (2002), “Transient Phenomena in Thixotropic Systems”, Journal of Non-Newtonian Fluid Mechanics, Volume 102.

9. Tanner, R. I. and Walters, K. (1998), “Rheology: An Historical Perspective”, Elsevier Science, Amsterdam.

10. Tattersall, G. H. and Banfill, P. F. G. (1983), “The Rheology of Fresh Concrete”, Pitman Books Limited, Great Britain.

11. Banfill, P. F. G. (1991), “The Rheology of Fresh Mortar”, Magazine of Concrete Research, Volume 43, Number 154.

12. Lapasin, R., Papo, A. and Rajgelj, S. (1983), “The Phenomenological Description of the Thixotropic Behavior of Fresh Cement Pastes”, Rheological Acta, Volume 22.

13. Langtangen, H. P. (1999), “Computational Partial Differential Equations, Numerical Methods and Diffpack Programming”, *Lecture Notes in Computational Science and Engineering,* Springer-Verlag, Germany.

14. Oldroyd, J. G. (1947), “A Rational Formulation of the Equations of Plastic Flow for a Bingham Solid”, Proc. Camb. Philos. Soc. Vol. 43.

15. Beverly, C. R. and Tanner, R. I. (1992), “Numerical Analysis of Three-Dimensional Bingham Plastic Flow”, Journal of Non-Newtonian Fluid Mechanics, Volume 42.

16. Hunter, R. J. (2001), “Foundations of Colloid Science”, 2nd edition, Oxford University Press, New York.

Long term experience with microsilica concrete in a marine environment.

Per Fidjestøl,
Elkem ASA Materials,
Box 8126, Kristiansand, Norway
e-mail: per.fidjestol@elkem.no

Harald Justnes,
Chief Research Engineer
SINTEF Civil and Environmental Engineering
Cement and Concrete, N-7034 Trondheim, Norway
e-mail: harald.justnes@civil.sintef.no

ABSTRACT

In 1977/78 three sections of a wharf in Gothenburg were cast in silica fume concrete of three different qualities, one with admixed chloride. At the same time companion sections were cast in conventional concrete – with similar target mechanical properties. The paper summarizes the results from an investigation of the four concrete qualities without admixed chloride. In summary: all concretes continue to gain strength, silica fume concrete is very resistant to chloride penetration, error function curve fitting is of dubious value for normal concrete, and silica fume content appears to be very important in controlling chloride ingress.

Key words: silica fume, microsilica, chloride, marine, field, strength.

1. INTRODUCTION

In 1977 and 1978 three sections of wharf were built in Gothenburg, Sweden. The wharf is described in a paper by Maage and Sellevold (1), reporting microstructural and mechanical properties. In 2000 a new set of samples were retrieved, taken from the same locations as previously. The investigations this time additionally included characterisation of chloride resistance properties and porosity. However, the results for strength and chloride resistance indicated that the nominal mixes reported in (1), taken from the construction reports, were incorrect. Thus, a fairly extensive analysis had to be performed in order to estimate the mixtures actually used – they were significantly different from the nominal mixtures reported.

The wharf is located at the mouth of the Gotha river on the west coast of Sweden (fig. 1). It is the outermost part of the massive port facilities of Gothenburg, and due to the dilution caused by the river is situated in slightly brackish water. The wharf is a massive structure and more than 600 meters long.

Five different concrete qualities were used, however, only four are reported here (the fifth used admixed chloride as accelerator). “Low” quality concrete was used in the lower part of the structure, while higher quality concrete was used in the upper part. Two separate mixtures were used for each of the exposure situations, with and without microsilica (silica fume). Thus, there is parallel exposure of otherwise (nominally) comparable concretes, giving unique opportunity to study the effect of microsilica addition.

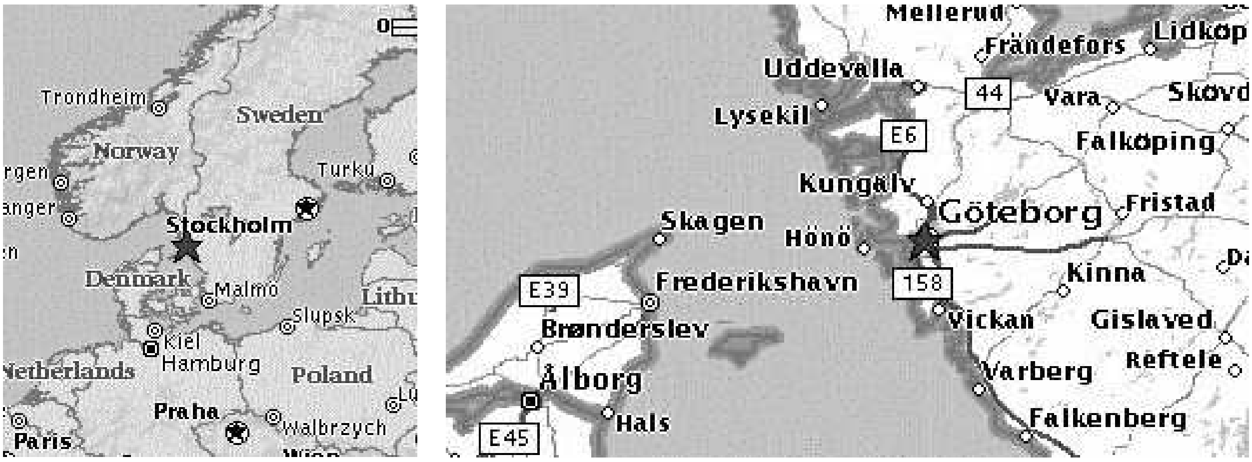

Figure 1. Location of the wharf

2. COLLECTION OF SAMPLES

2.1. Location of sampling areas.

The wharf has huge rubber bumpers to provide absorption of kinetic energy of. As can be seen from the photos the bumpers are fixed by brackets. These brackets have been sampled (See fig. 2). Because of the overhanging deck, the concrete in the brackets is protected from rain. Chloride exposure is from airborne chloride and splashing.

The lower half of the bracket is in K350 (35 MPa characteristic cube strength), while the upper part of the bracket is in K500 – 50MPa (Present-day nomenclature would be C25/30 and C45/50 respectively).

Figure 2A. Overview of wharves

Figure 2B & 2C. Overview and detail of wharves and bumper. Joint between concrete qualities can be seen.

2.2. Cores and their use

The cores that were drilled varied in length from 330 to 430 mm. After drilling, they were shipped to SINTEF in Trondheim, who performed the investigations (2).

Typical use of the cores was (SINTEF report 70161/1, (2)):

- Outer 120 mm from two cores: Chloride profile by grinding.
  (The concrete cylinder is placed in the chuck of a turning lathe, and milled layer by layer (e.g. 1 mm). The dust from each layer is collected, dissolved in nitric acid and the chloride content determined by a spectrophotometric method.)

- The outer 120-mm from the third core was used for plane and thin sections and for SEM.

- The next 100 mm from all cores were used for density and compressive strength (NS 3673 (density), NS3668 (compressive strength))

- The next 60-mm from each core was used for determination of chloride bulk diffusion according to Nordtest method NT Build 443

The final pieces were used for samples to determine capillary absorption according to an internal SINTEF procedure (3).

3. CONCRETE MIXTURE COMPOSITIONS

The nominal mixture compositions given in reference (1) were based on reports from the construction period. They were incompatible with the test results; even for such basic properties as strength and chloride ingress. It was therefore decided to attempt to estimate the recipes from analysis of the hardened concrete.

The procedures were extensive and involved DTG (Differential Thermal Gravimetry), wet chemistry and microstructural investigations. Fortunately the cement type was known (Gullhögen) as was its typical chemical composition at the time of construction. The silica fume that was likely to have been used at this location typically had a SiO_2 content of 92%, the value was used in the analysis. As it turned out, the differences between the nominal mixture designs and those determined by analysis were significant, and the mixtures determined in this testing are used in the rest of this report. The method used to determine the real mix has potential errors, but knowledge of the composition of component materials makes the determination more reliable. (The procedure is discussed in (3))

Table 1 gives the relevant details concerning the composition of the binder. The greyed out lines represent the nominal compositions.

Table 1. Nominal and estimated concrete composition (kg/m^3); nominal greyed out.

	1 (17/5-77)	2 (20/6-77)	3 (8-9/12-76)	5 (13-19/9-78)
Cement	370	445	270	315
	409	455	216	348
Silica fume	46 (12%)	0	40 (15%)	0
	22 (5.4%)	0	30 (13.7%)	0
Water	166	187	181	185
w/c	0,45	0,42	0,67	0,59
w/c+s	0,40	0,42	0,58	0,59
w/c+s	0.45	0.42	0.68	0.56

4. OBSERVATIONS

4.1. Compressive strength

Figure 3 shows that all concretes show consistent gain of strength over time, the effect of microsilica being approximately as expected – i.e. less relative strength increase from 28 days to 22 years.

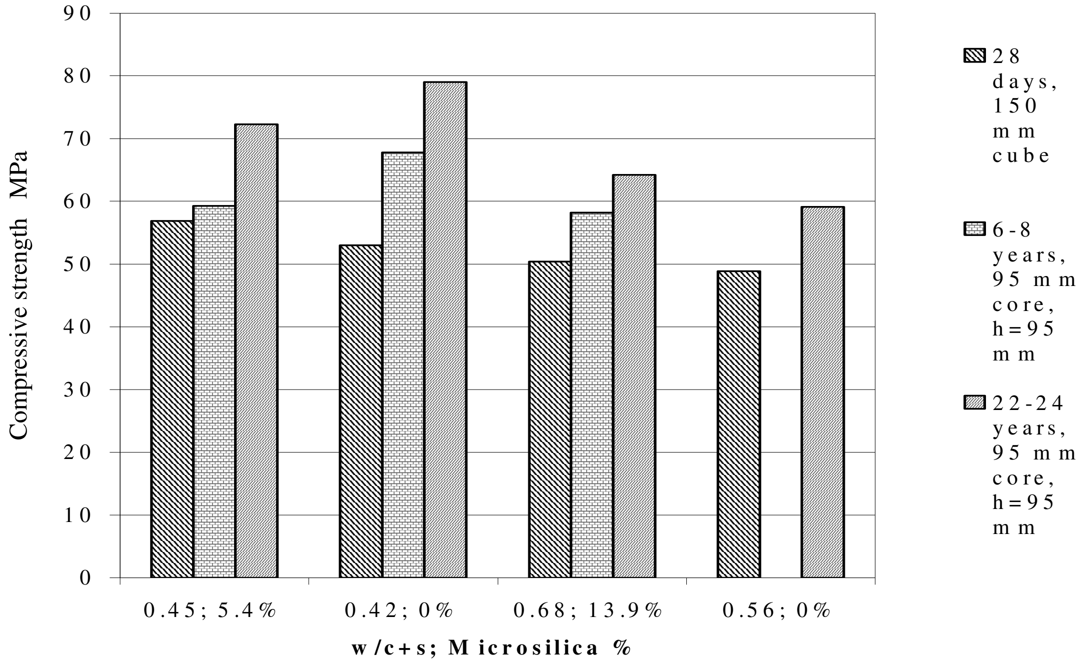

Figure 3. Development of compressive strength

4.2. In-situ chloride profile.

In situ chloride concentration profiles are given in figure 4.

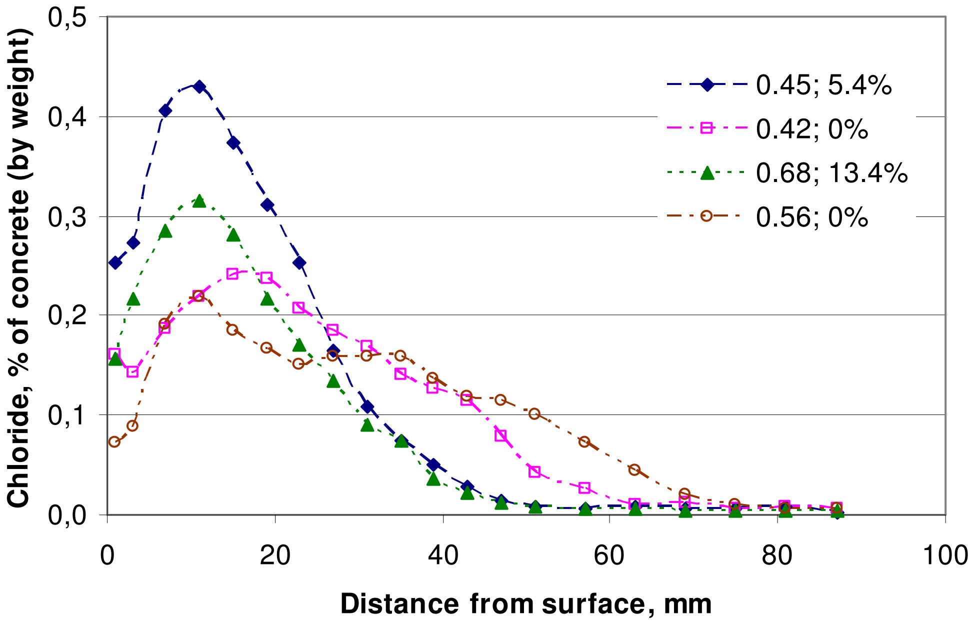

Figure 4. Observed chloride profiles

The most striking features are:

- The differences in shape between regular and microsilica concretes. Microsilica concretes have a shape reminiscent of concentration profiles in a diffusion process, conventional concretes look more like flow through capillary pores.

- The efficiency of microsilica in reducing chloride ingress.

- The important effect of microsilica on chloride ingress as seen on mixtures with w/c+s of 0.45 and 0.68 and microsilica content of 5.4 and 13.4% respectively. The graph shows that the efficiency factor of microsilica where chloride ingress is concerned is likely to be far higher than 2 that is used in EN 206. Pore refinement is the most likely contributor.

Also shown are the fitted curves (by least squares method) for determination of diffusion coefficient and surface concentration profile for two of the mixtures (fig. 5).

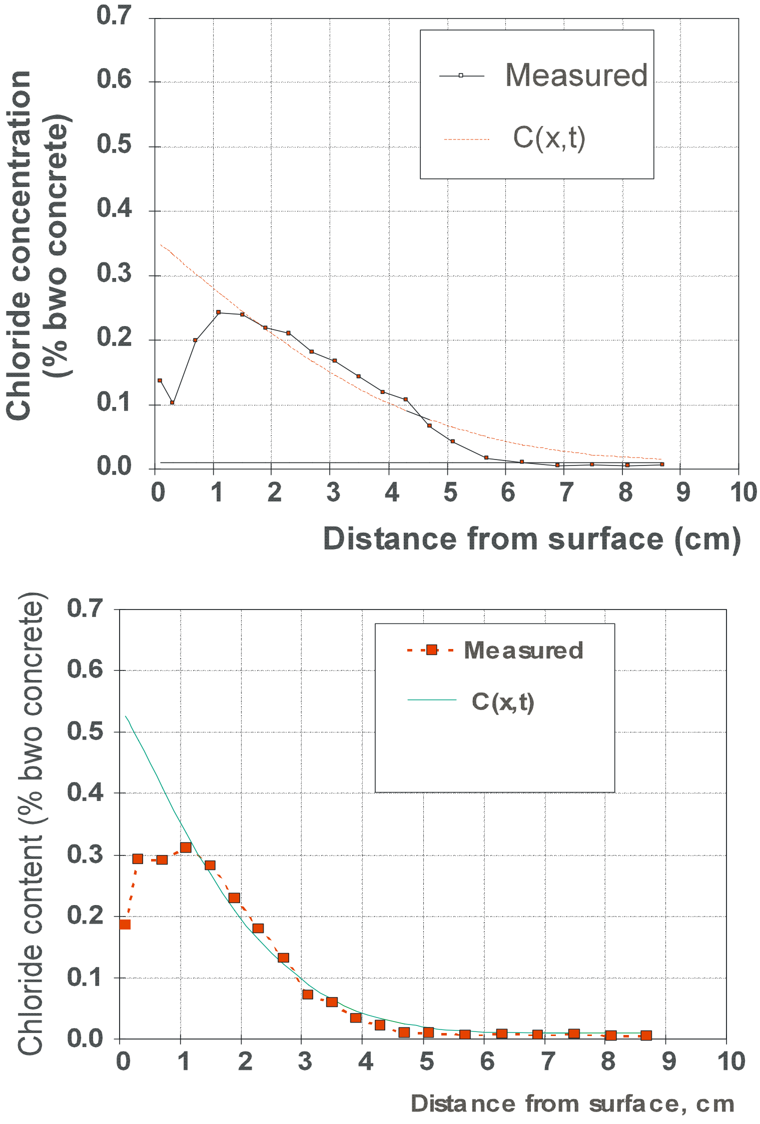

Figure 5. Fitting of error function curves
(Top: low w/c+s, no silica fume, Bottom: high w/c+s, 15% silica fume)

Table 2 shows estimated curve fitting parameters and corresponding regression

Table 2. Transport parameters by curve fitting to "Fick's 2^{nd} law"

Recipe	"Surface Concentration" C_0 (%)	Diffusion coefficient D_0 (10^{-12} m^2/s)	Regression coefficients
w/c+s=0.45, 5.4% microsilica	0.74	0.32	0.99, 0.97
w/c+s=0.42, no microsilica	0.37	0.90	0.95, 0.96
w/c+s=0.68, 13.8% microsilica	0.53	0.33	0.99, 0.99
w/c+s=0.56, no microsilica	0.26	1.9	0.92, 0.85

4.3. Laboratory chloride profiles (NT Build 443)

From the centre of the cores (i.e. most distant from the surface), specimens of 60 mm height were made. For all but one of the series, three parallels were tested. For the last series, two parallels were available. Determination of chloride resistance was performed according to NT Build 443 (table 3).

Table 3. Average transport coefficients from NTBuild 443

Recipe	"Surface Concentration" C_0 (%)	Diffusion coefficient D_0 (10^{-12} m^2/s)
w/c+s=0.45, 5.4% microsilica	0.97	3.5
w/c+s=0.42, no microsilica	0-99	17
w/c+s=0.68, 13.8% microsilica	0.95	3.2
w/c+s=0.56, no microsilica	0.73	31

4.4. Electrical resistivity

The electrical resistivity was determined using an internal SINTEF procedure where the ends of water saturated cylinders are coated with a conductive, water-based gel and the conductivity is determined at 1kHz. The results (mean of three samples) are in table 4.

Table 4. Electrical resistivity at 1kHz

Recipe	Specific resistance Ωm
w/c+s=0.45, 5.4% microsilica	156
w/c+s=0.42, no microsilica	52
w/c+s=0.68, 13.8% microsilica	301
w/c+s=0.56, no microsilica	62

4.5. Microstructural investigations

Plane and thin section.
These investigations showed that there were no signs of concrete deterioration for any of the samples. The microscopy indicated slightly lower w/c+s than the nominal mix specifications stated. The use of silica fume gave reduced portlandite content.

Carbonation was found in all samples, from 3.2 mm in the sample with 5% microsilica to a maximum of 6.7 mm in the sample from concrete with w/c+s=0.68 and 14% microsilica.

SEM
The investigation showed that the concrete with low w/c+s and 5% microsilica had significant amounts of unhydrated cement (fig. 6), indicating dry conditions inside the concrete. Such unhydrated cement was found close to the surface of the concrete. In this concrete, portlandite could not be identified, even if there should be a significant amount present, indicating that the portlandite is distributed throughout the matrix. Some microsilica agglomerates (about 10 microns diameter or less) were identified.

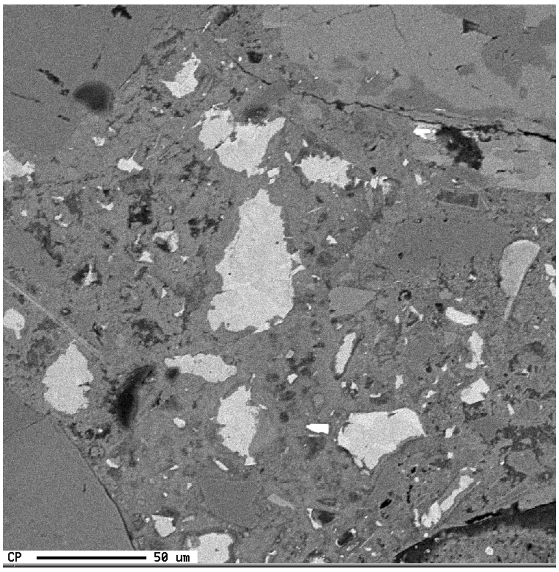

Fig.6. Unhydrated cement in low w/c+s, 5% MS concrete

In low w/c+s concrete without microsilica, portlandite was evident, especially in the paste/aggregate transition zone. The presence of ettringite in air voids indicates moist conditions.

High w/c+s concrete with 14% microsilica showed no portlandite (due to pozzolanic reaction). The cement appeared fully hydrated.

In the high w/c+s concrete without microsilica, much portlandite was found, both in the matrix and in pores.

Porosity and capillary absorption
Capillary suction and porosity were tested using internal SINTEF procedure KS 70 110. Table 5 gives average results (average of four parallel samples)

Table 5. Capillarity and porosity

Recipe	Resistance number $x\ 10^7$ s/m^2	Capillary number $x\ 10^2$ kg/m^{2}s$^{0.5}$	Suction porosity %	Open macro pores, %	Closed macro pores %
w/c+s=0.45, 5.4% microsilica	4.1	2.06	13.9	0.2	1.4
w/c+s=0.42, no microsilica	3.7	2.01	12.9	0.1	2.4
w/c+s=0.68, 13.8% microsilica	6.1	1.69	13.7	0.2	3.5
w/c+s=0.56, no microsilica	3.0	2.29	13.2	0.2	2.7

5. CONCLUSIONS AND SUMMARY

A main lesson to be learned is that old information should be checked as carefully as possible. The problems experienced concerning mixture design show this to be absolutely necessary.

This concrete has been exposed close to salt water, but protected from rain. Chloride exposure has been from airborne chlorides and possible splashing.

The results show a dramatic effect of microsilica on the resistance to chloride penetration; otherwise the most important observations are:

- Strength has consistently increased for all concrete qualities since 28 days.
- Chloride profiles for non-microsilica concrete indicate convection type chloride transport.
- Carbonation is likely to have influenced the shape of chloride profiles near the surface.
- After 22 years, the concrete with low w/c+s and microsilica still had unhydrated cement.
- Nominal and real mixture compositions were very different – especially for the microsilica concretes.
- Low chloride transport and high electrical resistivity of the microsilica concretes indicate that the corrosion protection of the steel reinforcement should be very good.

REFERENCES

1. Magne Maage and Erik J. Sellevold. Effect of microsilica on the durability of concrete structures. Concrete International, Volume: 9, Issue: 12. 1987
2. SINTEF reports 70161/1 through 70161/8. Various authors, Reports on various investigations on drilled cores from Älvsborgshamn wharf in Gothenburg (In Norwegian)
3. Harald Justnes. Effekt av silica – 25 års felteksponering. (Effect of silica – 25 years field exposure). Proc. Betonginformasjonsdagen 2001. Sintef Bygg og Miljø 2001. Trondheim. Page 50-52
4. NTBuild 443. Accelerated chloride penetration. Nordtest 1995. 5pp

Coefficient of Thermal Expansion (CTE) of Hardening Concrete

Erik Johan Sellevold
Ph.D., Professor
E-mail: erik.sellevold@bygg.ntnu.no

Øyvind Bjøntegaard
Ph.D., Postdoc
E-mail: oyvind.bjontegaard@bygg.ntnu.no

Both authors: Department of Structural Engineering, NTNU
7491 Trondheim, Norway

ABSTRACT

Crack sensitivity calculations for young concrete are strongly influenced by the coefficient of thermal expansion (CTE) values for the concrete. This paper demonstrates the strong effect of moisture content on CTE, and discusses the mechanism(s) behind. The temperature variation of the relative humidity (RH) exerted by the pore water is quantified and used to explain the high CTE of partly dried specimens. From a practical point of view crack sensitivities may be reduced by keeping the concrete as wet as possible during the early phase. This minimizes CTE and will largely eliminate autogenous shrinkage.

Key words: Cement paste, concrete, thermal expansion coefficient, moisture content, pore water thermodynamics

1. INTRODUCTION

The current worldwide interest in early age cracking problems in structures with High Performance Concrete (HPC) has led to intensive work on autogenous deformations. This concentration has resulted in neglect of the, normally even more important, thermally induced deformations. CTE is often just given a constant default value in calculation programs, while we know that it varies strongly both with concrete mix constituents (particularly aggregate type) and time (degree of self-desiccation). Fig. 1 (1, 2) shows typical behaviour from early times for a pure cement paste (a) and a concrete (b) with the same paste as binder (about 28 vol%). Note that "DCS" in the figure means degree of capillary saturation, which equals to degree of water saturation (and 10^{-6} = microstrain = μs). Both curves are for sealed hydration up to the time when the specimens are immersed in water. Before setting both cement paste and concrete have very high CTE values since no solid framework exists and the continuous water phase controls. CTE reduces as solids form, reaching a minimum value around the final set, which points are shown in Fig. 1. From then on CTE increases as self-desiccation proceeds. The increase for paste is about from 10 μs/°C to 22 μs/°C, and the reduction after water immersion back to 13 μs/°C. For concrete the equivalent numbers are about from 7 μs/°C to 11 μs/°C, and back to 7 μs/°C. These numbers demonstrate clearly the dominant influence of the water content on CTE; for the concrete CTE returns to the exact same value it had on setting after full saturation at an

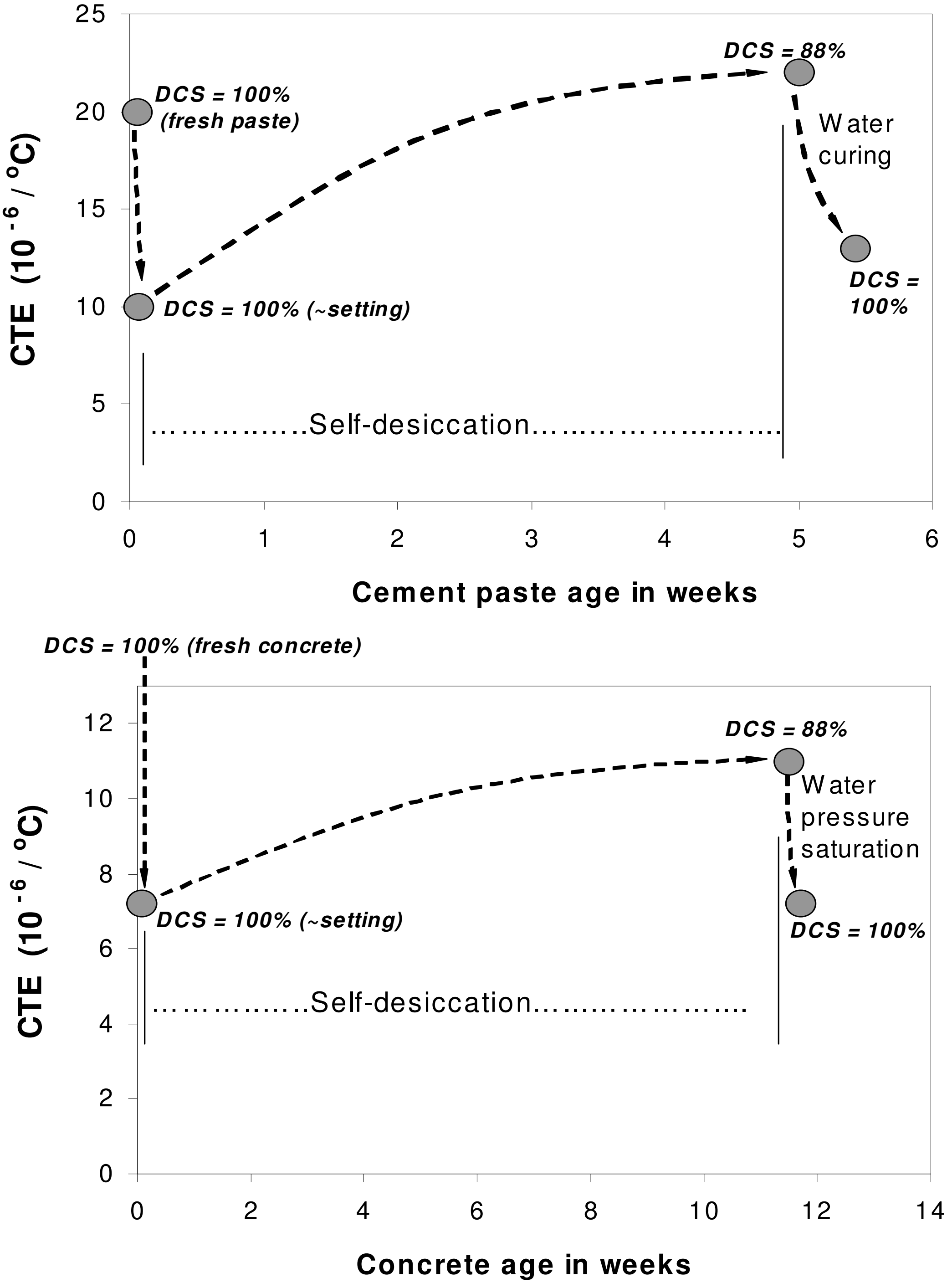

Figure 1 - Effect of the degree of capillary saturation (DCS) on the Coefficient of Thermal Expansion (CTE) of: a) cement paste (w/b = 0.40 and 5% silica fume) and b) concrete with the same paste as binder (28 vol%). Bjøntegaard (1)

age of 11 weeks, i.e. the hydration has no net effect on the CTE in saturated state (!). The moisture effect is clearly very important from a practical point of view, and simple in the sense that the CTE value of a given concrete can be controlled by controlling the moisture content. Minimum CTE is obtained in a wet state, i.e. by supplying an internal water source during curing two important benefits are obtained: the autogenous deformation is reduced or eliminated and CTE is minimized.

This dramatic effect of moisture content on CTE has been demonstrated repeatedly for mature cement pastes since the classic work by Meyers 1951 (3). Powers 1958 (15), Helmuth 1960 (4), Dettling 1964 (5) and Bazant 1970 (6) have made significant contributions to our, yet incomplete, understanding of the underlying mechanisms. This brief paper gives the authors' current view of the mechanisms as a basis for discussions.

CTE cannot be uniquely defined for concrete, since an imposed temperature change produces time dependent deformations. It is therefore a choice what is called immediate deformations (ID) and counted as CTE, and what is considered delayed deformation (DD) and, thus, not included in the CTE.

In practice thermal equilibrium in a test sample is reached much faster than deformation equilibrium, but still ½ - 1 hour is needed in most experimental setups before the temperature gradient is small enough to allow ID to be defined. Often in the literature CTE is found from dynamic experiments, i.e. deformations are recorded during heat-cool cycles. If there is no hysteresis then CTE is uniquely defined as the slope of the curve in a T vs. deformation plot; however, in practice there is hysteresis that depends both on the specimen size, the rate of temperature change and the magnitude of DD, producing a CTE value that may depend strongly on all the experimental conditions.

For hardening concrete an additional complication exists. Under realistic temperature development (heating followed by cooling) the total deformation can be measured relatively easily. To separate the total deformation into its thermal and autogenous components the best procedure is to calculate the thermal part by using the temperature history and the relevant CTE (1, 2). The thermal part is then subtracted from the total to produce the autogenous part. However, this autogenous part will also include a time dependent component (i.e. delayed deformation = DD), which is a function of the moisture content as discussed below. The consequence is that definition of the "pure" autogenous deformation under realistic temperature conditions is very complex. This "DD-complication" is probably the main reason why the autogenous deformation depends strongly on the temperature history, as discussed in (1, 2, 7).

2. MECHANISMS

There appears to be general agreement in the literature that both the strong dependence of CTE on moisture content and the existence of DD are related to temperature-induced redistribution of moisture in the pore system. We share this view and will discuss the mechanisms in three categories, roughly (but not entirely) corresponding to those proposed by Bazant (6).

1) Pure thermal dilation
2) Thermal shrinkage or swelling
3) Relative humidity change

2.1 Pure thermal dilation

Each constituent material (solid particles, adsorbed water, pore water etc.) has a CTE value. CTE of water is much higher than CTE of solids and water in small pores probably has higher CTE than bulk water. Thus, a very fast temperature increase followed by an isothermal period will lead to fast expansion (ID), followed by a time dependent contraction (DD) as the induced excess pressure in filled pores is dissipated by flow to the outside or to partly empty pores. Scherer (8) and Ai et al. (9) have used this phenomenon to measure water permeability in saturated cement pastes. Depending on the permeability of the paste and the distance to available "sinks", the pressure relief may be fast or slow, i.e. it may appear as ID and hence be counted in CTE, or as DD. The literature shows that DD is much more prevalent in saturated samples than in partly dried. Thus, for concrete in practice where the most normal moisture state is "natural self-desiccated condition" less DD is found, and any pressure relief mechanism is presumably very fast and counted as ID and part of CTE.

2.2 Thermal shrinkage and swelling

Pore water can roughly be divided into two types. Gel water, a collective term for water which is strongly influenced by its proximity to solid surfaces; i.e. interlayer water, adsorbed water and water in very small pores (gel pores). Capillary water is water in larger pores (smallest dimension over a few nm), and it is commonly treated as bulk water under the influence of capillary tension when the sample is not fully saturated, i.e. when curved water- air menisci exist. At saturation there is no capillary tension, but the water in these "larger" pores is still commonly referred to as capillary water and the pores as capillary pores.

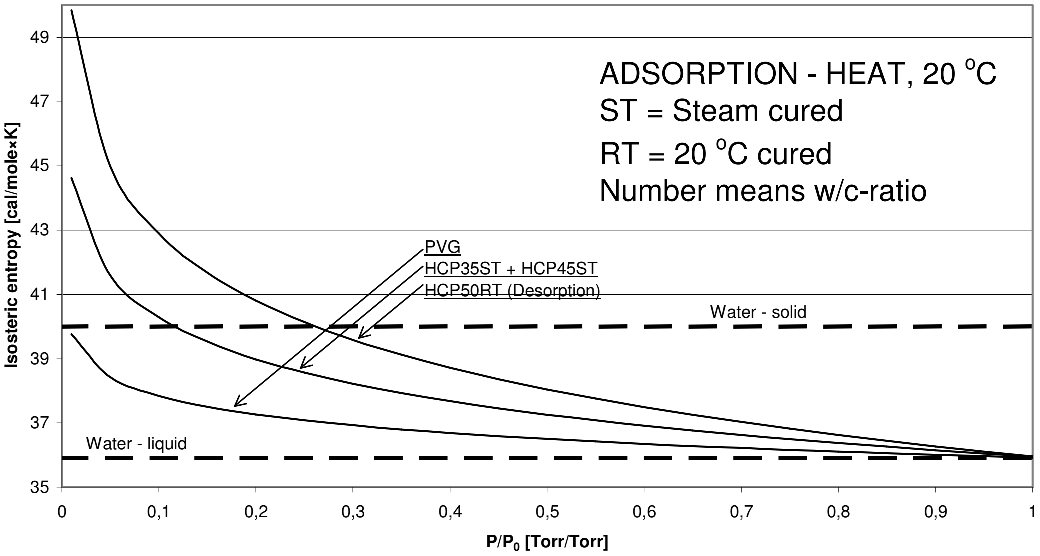

Figure 2 - Entropy of adsorbed water (relative to saturated vapor). HCP = Hardened Cement Paste, PVG = Porous Vycor Glass. Low relative vapor pressure is associated with gel water, higher values with capillary water. Note that large ordinate values mean large change from vapor state, i.e. low absolute entropy - as also demonstrated by the ref. water and ice lines. Radjy, Sellevold and Hansen (10).

Equilibrium requires that the chemical potential (molar Gibbs free energy) of coexisting water phases is equal both before and after a temperature change. The rate of change of the chemical potential of a water phase with respect to increasing temperature is the negative of the entropy. The entropy of gel water is lower than that of capillary water as shown in Fig. 2, Radjy, Sellevold and Hansen (10). Thus, a sudden increase in temperature leads to a higher chemical potential in gel water than in capillary water, setting up a driving force for an internal redistribution of water from gel to capillary pores. This is expected to lead to shrinkage, i.e. sudden heating of cement paste sample is expected to produce a sudden expansion followed by a time dependent contraction. On cooling the opposite effect is expected; a sudden contraction followed by a time dependent expansion as water moves from capillary pores to the gel. It is perhaps difficult to visualize how water can redistribute in a saturated sample, i.e. when there is no available space. The theory is that, for example, cooling will force water to the gel pores in an amount necessary to increase the local pressure (disjoining pressure) enough to establish equilibrium in chemical potential with the water in capillary pores. This pressure in the gel water will produce expansion.

In less than saturated samples the situation is that the gel pores are full, but the capillary pores partly empty and with the water under capillary tension. The redistribution takes place as for saturated samples, in theory, implying the possibility of a situation after cooling when the gel water is under pressure (disjoining) while the capillary water is under tension. This situation produces chemical potential equilibrium, but the physical reality of the situation is perhaps questionable. It should be added that it is impossible to calculate the magnitude of any of the redistribution effects with any reasonable certainty. The thermodynamic arguments tell us in which direction water moves, but quantification requires much more basic data than we have presently.

Powers (15) and Helmuth (4) explained DD results for saturated specimens only in terms of this gel-capillary redistribution mechanism, and did not consider the excess pressure mechanism due to high CTE of water discussed above. We consider that the gel-capillary mechanism is slow so that it mainly results in DD, and therefore cannot explain the very large effect of moisture content on CTE shown in Fig.1. Note that Helmuth did consider the gel-capillary mechanism responsible for the moisture effect on CTE, arguing that at 82% degree of water saturation there was "…not enough capillary water to allow redistribution" - i.e. it is the absence of redistribution that is responsible for the high CTE at 82% saturation. We do not share this view, and we recognize that the fact that there is very little DD in the 82% saturation sample is difficult to reconcile with the gel-capillary redistribution mechanism being primary responsible for the large DD in saturated samples. The excess pressure mechanism appears more consistent.

2.3 Relative humidity change

The raw data in the project to obtain enthalpy and entropy of pore water (10) was vapour pressure vs. temperature for a given cement paste at different moisture contents. Fig. 3 shows such data in a principle sketch. A characteristic of the results is that the curves are nearly straight lines, and that the slopes increase as the moisture contents are reduced, i.e. that the enthalpy of the pore water decreases with decreasing moisture content, see Fig. 4, as is true for all adsorbent/adsorbate systems. Fig. 3 illustrates clearly a very important aspect: If the lines were parallel then the RH would be independent of temperature (easy to prove mathematically, remembering that at any given temperature, RH equals the vapour pressure exerted at a certain moisture content divided by the saturation vapour pressure). When the lines are not parallel as in Fig. 3 the result of heating from T_1 to T_2 is that RH increases, since:

$$\frac{p_2}{p_2^o} > \frac{p_1}{p_1^o} \qquad \text{hence } RH_2 > RH_1$$

This effect has been measured by several researchers (6, 10, 11, 12, 14), and has important consequences for CTE. The effect is shown in Fig.5, which is taken from (10). The scatter between the three sources is large, but the magnitude of the effect is at least indicated. It should be noted that the data from (10), (11) and (12) were obtained using very different principles of measurement. New data by Nilsson (14) is roughly in line with the plot, but also shows a clear w/c-effect; the %RH/°C-factor decreases as the w/c increases. The phenomenon is further discussed in (10).

The consequences of the RH-increase on heating for CTE may be estimated using Fig.5 and isothermal shrinkage data, for example Hansen (13). A mature paste (w/c=0.4) cured isolated may self-desiccate to 85% RH (the value depends on the cement). The %RH/°C-factor may be about 0.2%/°C (Fig.5), and the slope of the shrinkage-RH curve about 60 μs (microstrain) per %RH (13). Then the apparent CTE from this mechanism becomes 0.2 x 60 = 12 μs/°C. Fig.1 showed CTE to be 22 μs/°C for the 88% saturated paste (roughly corresponding to RH=85%), of which then maybe 12 μs/°C are caused by the RH-effect.

P^o_2

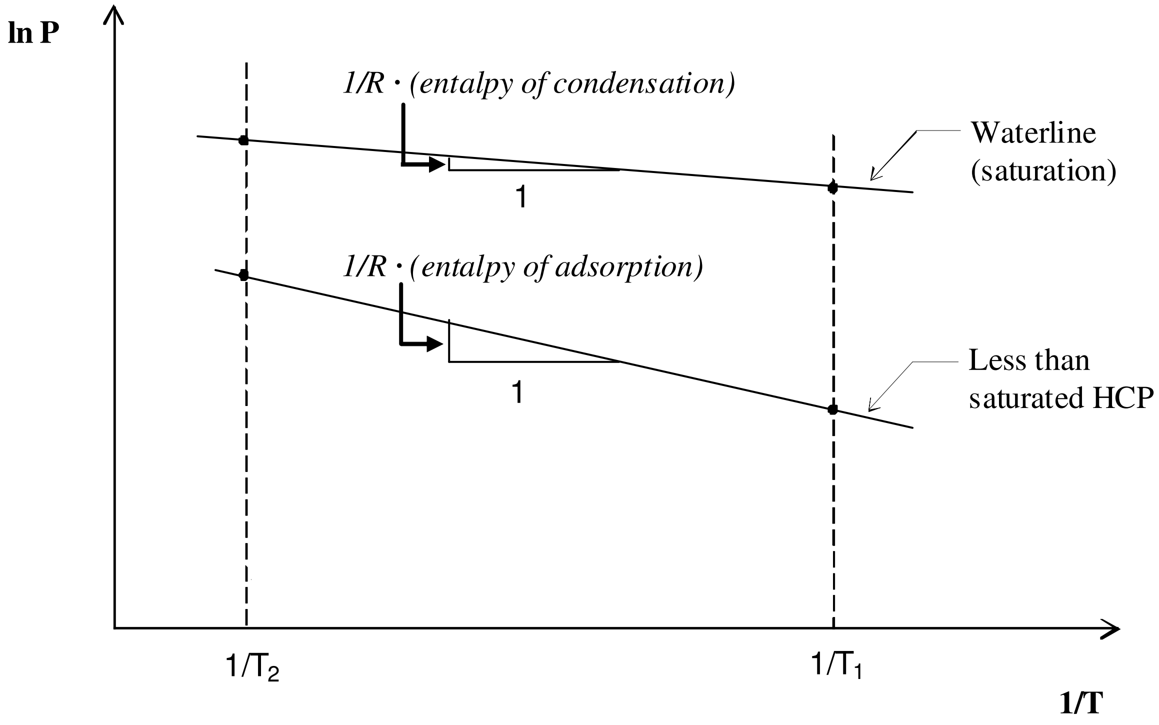

Figure 3 - Vapor pressure exerted by pore water in hardened cement paste vs. inverse of temperature for different constant water contents. Principle sketch.

P_2

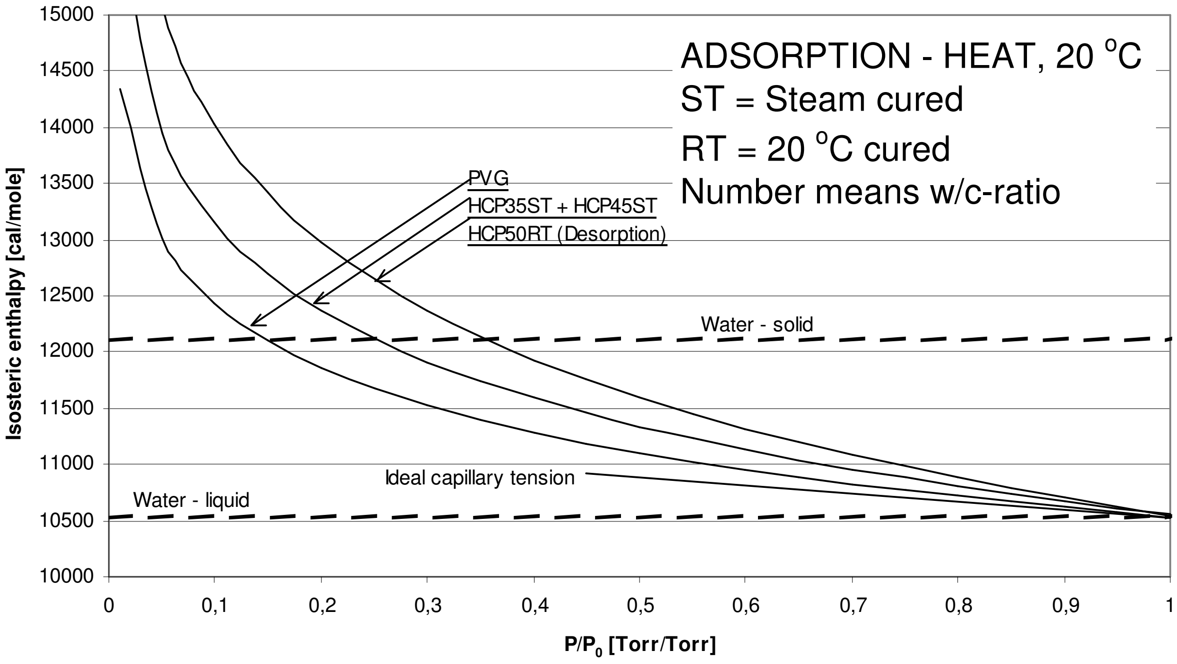

Figure 4 - Enthalpy of adsorbed water (relative to saturated vapor). HCP = Hardened Cement Paste, PVG = Porous Vycor Glass. Radjy and Sellevold (10)

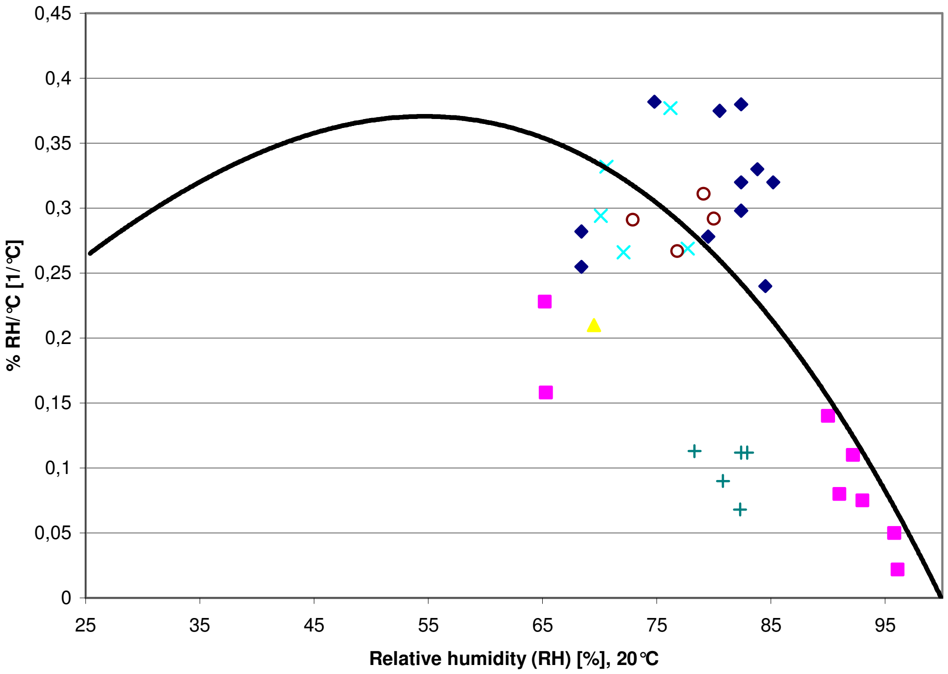

Figure 5 - The change in RH per ^{o}C at different RH-values exerted by the pore water in cement pastes. Solid line is for HCP50RT = a mature cement paste with w/c = 0.50 cured at 20 ^{o}C (10). Points are from Nilsson (11) and Persson (12).

Thus, the RH-mechanism alone is able to explain the whole moisture content effect on CTE. However, note the uncertainty in the value 0.2%/°C taken from Fig.5, *i.e.* the explanation should only be considered a possibility since it works in principle and has the right order of magnitude. It is of course implied that the RH-effect is fast and the resulting deformation is ID - and hence recorded as part of the CTE. How this RH-mechanism works in physical detail is not obvious. One model is sketched here: At 88% saturation the paste certainly contains water under capillary tension due to existence of air-water menisci. Possibly is each meniscus the interface between the air and a significant volume of pore water. A temperature increase will lead to expansion of this water, which again can result in increased radius of the meniscus as the waterfront moves outward. The increased radius leads to an increased RH according to the Kelvin equation. The increased temperature also leads to reduction of the air-water interfacial tension - again increasing the RH. Thus, the RH-increase due to heating at constant moisture content can be explained. The model is discussed in more detail in (1) and (10).

3. CONCLUSIONS

Crack sensitivity calculations for young concrete are strongly influenced by CTE values for the concrete, since in most cases the thermal deformations are more important than the autogenous in generating stresses. This paper demonstrates the strong effect of moisture content on CTE, and discusses the mechanism(s) behind. From a practical point of view crack sensitivities may be reduced by keeping the concrete as wet as possible during the early phase. This minimizes CTE and will largely eliminate autogenous shrinkage.

From a fundamental point of view the situation is less clear. It is satisfactory that the RH-mechanism apparently alone is able to explain the effects of moisture content on CTE. However, the role of the different mechanisms at various moisture contents, and in particular their relationship to DD, cannot be coherently explained today. In our view the most urgent need is for more experimental data, starting with mature hardened cement pastes in well defined moisture conditions. This is a necessary first step before introducing the complexities of changing temperatures in hydrating systems.

ACKNOWLEDGEMENTS

This paper is a product of the Norwegian NOR-CRACK project. The financial contribution of the Norwegian Research Council and the project partners are gratefully acknowledged. The partners in the project are the Norwegian Public Roads Administration, Selmer-Skanska ASA, Norcem A.S., Elkem ASA and Fesil A.S., and NTNU-Department of Structural Engineering (project leader).

REFERENCES

1. Bjøntegaard, Ø., Thermal Dilation and Autogenous Deformation as Driving Forces to Self-Induced Stresses in HPC, Doctoral thesis, NTNU, Dec. 1999.
2. Bjøntegaard Ø. and Sellevold E.J., Interaction between Thermal Dilation and Autogenous Deformation in HPC, Matr. and Str., Vol.34, June 2001, pp 266-272

3. Meyers S.L., How Temperature and Moisture Changes May Affect the Durability of Concrete, Rock Products, August 1951, pp. 153-178
4. Helmuth R.A., Dimensional Changes of Hardened Portland Cement Pastes Caused by Temperature Changes, Highway Research Board, 40, 1960, pp. 315-336
5. Dettling H., “Die Wärmedehnung des Zementstaines, der Gesteine und der Betone” (thermal dilation of cement paste, aggregate and concrete), Deutscher Ausschuss für Stahlbeton, Heft 164, Berlin 1964 (in German)
6. Bazant Z.P., Delayed Thermal Dilatations of Cement Paste and Concrete due to Mass Transport, Nuclear Eng. and Design, 1970, pp. 308-318
7. Bjøntegaard Ø. and Sellevold E.J., Thermal Dilation and Autogenous Deformation, Proc. of the RILEM Int. Conf. on Early Age Cracking in Cementitious Systems, Ed. by K.Kovler and A.Bentur, Haifa, Israel, March 12 - 14, 2001, pp.63-70
8. Scherer G.W., Measuring Permeability of Rigid Materials by a Beam-Bending Method: I, Theory, J. Am. Ceram. Soc., 83, 9, 2000, pp 2231-2239
9. Ai H., Young J.F. and Scherer G.W., Thermal Expansion Kinetics: Methods to Measure Permeability of Cementitious Materials: II, Application to Hardened Cement Pastes, J. Am. Ceram. Soc., 84, 2, 2001, pp. 385-391
10. Radjy F., Sellevold E.J. and Hansen K.K., Isosteric Vapor Pressure - Temperature Data for Water Sorption in Hardened Cement Paste: Enthalpy, Entropy and Sorption Isotherms at Different Temperatures, Report BYG-DTU R-057, Techn. Univ. of Denmark, Lyngby, 2003. Available at http://www.byg.dtu.dk/publicering/rapporter/R-057.pdf
11. Nilsson L.-O., Temperature Effects in RH Measurements on Concrete - Some Preliminary Studies. The Moisture Group. Report 1987:1, BFR. 1987, pp. 84
12. Persson B., Compatibility Between Flooring Material on Concrete and Moisture, Volatile Organic Compound, and Adhesion, Working Report, Division of Building Materials, Lund Institute of Technology, Lund 2001, pp. 29 (in Swedish)
13. Hansen W., Drying Shrinkage Mechanisms in Portland Cement Paste, J. Am. Ceram. Soc., 70, 5, 1987, pp. 323-328
14. Sjøberg A., Nilsson, L.-O. and Rapp T., Publikation P-o2:1, Fuktmätning i betonggolv med golvärme. Etapp 1: Förstudie, Inst. for Byggnadsmaterial, Chalmers Tekn. Høgskola, Gøteborg, Sweden, 2002 (in Swedish)
15. Powers, T.C., The Physical Structure and Engineering Properties of Concrete, Research Dep. Bulletin 90, Portland Cement Association, Chicago, July 1958

Accelerated Carbonated Concrete as Corrosion Environment

Saija Varjonen
M.Sc., Research Engineer
Tampere University of Technology
E-mail: saija.varjonen@tut.fi

ABSTRACT

The corrosion of steel in concrete may occur when carbonation has destroyed the protective passivation layer on the steel. Carbonation of concrete is a slow phenomenon and in laboratory studies special treatments are often used to accelerate carbonation to enable the corrosion of steel to start earlier. With accelerated methods it may be, however, not possible to achieve exactly the same result as due to the natural carbonation. This study investigated the effects of accelerated carbonation on the concrete and the potential differences between naturally carbonated concrete especially from the corrosion point of view. Corrosion rate and corrosion potential of steel bars in naturally and accelerated carbonated concrete was measured with computer-aided monitoring system. According to electrochemical measurements the corrosion rate in accelerated carbonated concrete may be smaller than in naturally carbonated concrete.

Keywords: carbonation, corrosion, accelerated carbonation, concrete

1. INTRODUCTION

1.1 Background

Among the most pressing concerns for the durability of structural concrete is the corrosion of reinforcement. It has recently received much attention as a topic of numerous experimental studies.

Reinforcing bars in alkaline concrete are protected from corrosion by a thin passivation layer. Corrosion may start when this passivation layer is destroyed, either by chloride penetration or due to the lowering of the pH by the carbonated concrete. Only carbonation is dealt with in this study.

Carbonation of concrete is a chemical reaction where atmospheric CO_2 diffuses into the pore system of concrete through the pores of concrete and causes changes into the chemical composition of concrete. In carbonation the carbon dioxide reacts principally with calcium hydroxide to form calcium carbonate [1][2]:

$$Ca(OH)_2 + CO_2 \rightarrow CaCO_3 + H_2O$$

The calcium hydroxide is not the only substance that reacts with CO_2; the other hydration products and even the residual unhydrated cement compounds also take part into carbonation reactions [3].

Due to carbonation, the alkalinity of the pore fluid drops from a pH value exceeding 12.6 to a value about of 8.0. A critical pH value, where the passive layer cannot protect the steel anymore is around 11.4 [1]. Below that level corrosion starts if there is enough moisture and oxygen present.

The volume of formed calcium carbonate exceeds that of the parent hydrate. This is why carbonation reaction generally causes a reduction in porosity [1]. According to [4] smaller pore diameters are reduced in diameter in carbonation. The effect does not seem to be significant in larger pores. The reduction of permeability due to carbonation is generally agreed, but also contradictory results, especially concerning specimens with low strength, have been published [5].

Carbonation of concrete is relatively slow under natural conditions. The progress of carbonation depth can be modelled by the following equation [6]:

$$x = k \cdot \sqrt{t}$$

where x is carbonation depth [mm]
k is carbonation coefficient [mm/a$^{0.5}$]
t is time [a]

Because of the slow phenomenon, the investigation of carbonation is usually conducted under accelerated conditions, with higher CO_2-concentrations, for example 4 %-vol, to speed up the process. Four weeks of accelerated carbonation in 4 %-vol is often considered as equivalent to approximately 4 years in natural conditions [7] [8].

The various factors influences carbonation [1] [4] [9]:

- The permeability of concrete
  The permeability of hardened cement paste is affected by the type of cement, the water/cement ratio, the degree of hydration (curing) and the compaction of the concrete. Correspondingly the moisture content of the concrete is also a substantial factor. The presence of water is necessary for carbonation. On the other hand, if the pores of concrete are saturated, the diffusion of carbon dioxide is slow. The diffusion rate of CO_2 in water is about four decades lower than in the air. According to [1], the rate of carbonation reaches its maximum at the range of the relative humidity of 50 to 70 %.
- The amount or reactive material
  Cement content, type and quality affect the carbonation; the more the cement, the more calcium hydroxide and the longer it takes to carbonate. Also the total alkalinity available to react with CO_2 influences carbonation.
- The content of CO_2 in the air.
  For most of the concretes studied in [7], increase of the carbon dioxide concentration beyond 4 % had little effect on carbonation rates.
- Temperature
  According to [10] the rate of carbonation is very weakly sensitive to temperature (RH 65 %).

The corrosion of steel in concrete is an electrochemical reaction where corroding steel acts as an anode (where steel dissolves as positive ions into the electrolyte) and cathode (where water reacts with oxygen producing hydroxyl ions). The reaction requires also an electrolyte in which ions migrate towards each other to form corrosion products (rust). An electron conductor between anodic and cathodic areas (steel) is also essential for the reaction [1] [11] [12].

The electrochemical sub-reactions are (Fig. 1)[12]:

Anodic: $Fe \rightarrow Fe^{2+} + 2e^{-}$
Cathodic: $2H_2O + O_2 + 4e^{-} \rightarrow 4OH^{-}$

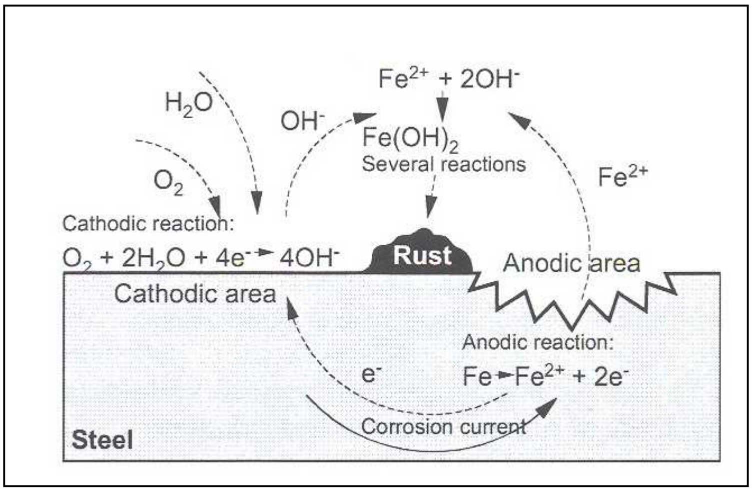

Figure 1 - Electrochemical reactions of steel corrosion in neutral or alkaline solution [12].

The rate of corrosion in chloride-free concrete depends on [12]:
- pH of pore solution
- Resistivity of electrolyte
- Oxygen supply
- Temperature.

1.2 Objective

The aim of this study was to establish whether representative specimens can be prepared by accelerated carbonation for studying active corrosion of reinforcement.

The study was limited to the effects of carbonation and carbonation induced corrosion in specimens which contain OPC. Chloride-induced corrosion, the effects of admixtures and different cementitious materials, like fly ash, ground granulated blast furnace slag and silica fume, were excluded.

2. TEST PROGRAMME

The protective properties of concrete specimens against corrosion and the corrosion rate of steel in carbonated concrete were tested using electrochemical methods. The samples were carbonated either in natural environment or under accelerated conditions. The effects of carbonation on the pore structure of concrete were determined with cup tests. Water absorption tests were used to study the capillarity of the specimens.
Carbonation chamber

Accelerated carbonation has been used at least since 1968 [12]. Curing and test conditions have varied between different laboratories because there has not been standardised method for this test. The accelerated carbonation testing of concrete was reviewed by BRE in 2000 [7]. Based on this research, standard recommendations for carbonation system have been given:

- CO_2 level 4 %
- Relative humidity 65 %
- Temperature 20 °C
- Active CO_2 control
- Efficient circulation fan
- Calibration and logging
- Reference mix.

The carbonation chamber used in this study satisfies most of the requirements. The relative humidity was 75±5 % and no reference mix was used. The progress of carbonation was followed using the phenolphthalein test.

The carbonation in the accelerated conditions used in this study can be considered to be roughly 50 times faster than in normal conditions [8].

2.1 Electrochemical measurements

The potential measurements can be used to evaluate whether the corrosion of steel takes place. When passivation layer protects the steel, the anodic reaction is prevented and the mixed potential of steel is relatively high. After the passivation layer is disrupted, the mixed potential decreases. The potential can be monitored by half-cell measurements using a simple reference electrode. The practical measurement is described for example in [13].

There are guidelines for interpreting the results of corrosion potential measurements. The connection between corrosion potential and probability of corrosion with copper-copper sulphate reference electrode is presented in Table 1 [12].

Table 1 – Correlation between half-cell potential and probability of corrosion [13].

Half-cell potential vs. CSE	Probability of corrosion
> -200 mV	Less than 10 %
-200…-350 mV	Uncertain
< -350 mV	Higher than 90 %

The corrosion rate can be evaluated by polarisation resistance method. In this method the current change is examined by the function of electrode potential (polarisation curve). The polarisation curve is close to linear near the rest potential. The slope of this linear part is called polarisation resistance ($\Delta E/\Delta I$). The corrosion rate (i_{corr}) can be evaluated by the equation [14]:

$$i_{corr} = \frac{B}{R_p \cdot A}$$

where B = coefficient that depends on the Tafel slopes
R_p = the polarisation resistance [Ω]
A = the area of polarised metal [m²]

In the case of steel in concrete 26 mV can be used as the coefficient B when corrosion is in active state and 52 mV when corrosion is still in passive state [14].

As for potentials, there are also guidelines to interpret the results of corrosion rates (Table 2):

Table 2 – Levels of corrosion rate [15].

Attack penetration (µm/year)	Corrosion rate (µA/cm²)	Corrosion level
< 1	< 0.1	Negligible
1-5	0.1-0.5	Low
5-10	0.5-1	Moderate
> 10	> 1	High

The theoretical background for electrochemical measurements is presented for example in [12].

The electrochemical measurements in this study were performed with computer-aided measurement system, which has been prepared in the Laboratory of Structural Engineering at Tampere University of Technology. In this system, the potential is controlled and the passing current is recorded. The measurements were carried out using a CSE reference electrode with a potential of +318 mV vs. SHE. Passive steel was also used as a reference electrode for short term polarisation purposes. The potential shift used for determining R_p was +10 mV and the waiting time 40 s. The ohmic drop was compensated by the current interruption method.

Specimens of type 1:

A thin layer (2.5 mm) of OPC mortar was cast on one face of a flat section of steel. The area of the specimen exposed to corrosion was 40*75 mm² the rest of the surface being sealed by adhesive tape.

Two kinds of mortar mixes were used. The first (Mix 1) contained OPC and sand (0-0.6 mm) in the weight proportions of 1:4.5. The water/cement ratio of the mix was 1.08. The second (Mix 2) contained OPC and filler (< 0.125 mm) in the weight proportions of 1:1.6. The water/cement ratio of the second mix was 0.74. The reason for the high water/cement ratios was to enable fast carbonation. Specimens were cured on wet cloth (the cloth was in contact with water 40 °C) for one week after which they were stored at RH 75 % with minimal content of CO_2 for at least 2 weeks. After curing the specimens were covered so that only the area of 20*50 mm² was exposed (Fig. 2).

The specimens were divided into three groups (five parallel specimens in each group). One third of the specimens were retained alkaline (RH 75 %, CO_2 ~ 0 %). One third was carbonated in natural conditions (RH 75 %, CO_2 0.04 %) for 10 months. The rest was carbonated accelerated in 4 % CO_2 and 75 % relative humidity for 6 months after which they were stored at natural conditions (RH 75 %, CO_2 0.04 %) for one month.

Three specimens were sealed throughout with the adhesive tape to reveal the possible current leaks through the sealing. No measurable corrosion occurred in these specimens during the tests.

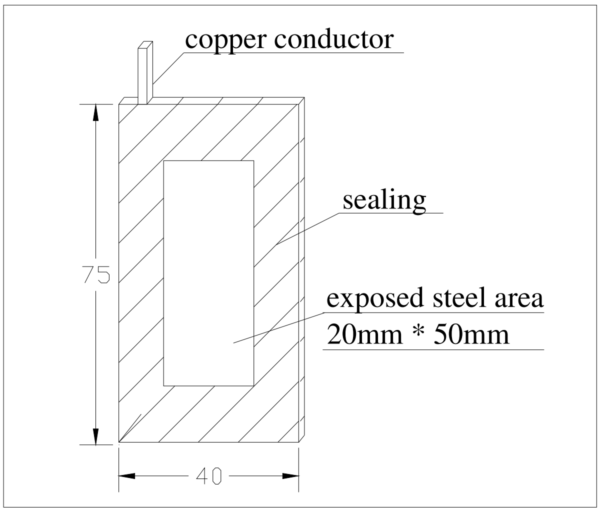

Figure 2 – Diagram of specimens of type 1.

Specimens of type 2:

Specimens of type 2 were prepared from pieces taken from a demolished concrete shelter built in 1950s-1960s. The maximum aggregate size of the concrete was 25 - 35 mm. The specimens contained reinforcing steel in alkaline and in carbonated concrete. The specimens with alkaline concrete were carbonated accelerated for 15 weeks.

For electrochemical measurements an extra layer of mortar (w/c = 0.78) was cast on the rear side of the specimens to allow the embedment of steel bars acting as counter and reference electrodes. These were steel bars with a diameter of 4 mm and nominal yield strength of 500 N/mm² (B500K) (Fig. 3).

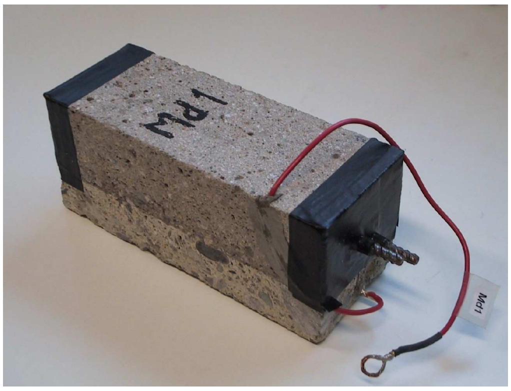

Figure 3 – Specimens of type 2.

2.2 Cup tests

Water vapour permeability of the specimens was measured by the simple cup tests. In this study the cup test were conducted to find out potential differences in porosity between normally carbonated and accelerated carbonated specimens.

The cup tests were performed in a chamber with temperature of 20 °C and RH of 75 % produced by saturated sodium chloride solution. The chamber was equipped with a blower to ensure even humidity everywhere in the chamber. The relative humidity in the cups was intended to be 97 %

(saturated potassium sulphate solution in the cup). According to measurements the RH in the cups was around 95 %.

The permeability was determined by weighing the cup periodically until the steady-state was reached. In steady-state the rate of change in weight during 7 days was measured and the water permeability calculated according to the following equation:

$$\delta = g\frac{d}{\Delta p} = \frac{\Delta m}{At} \cdot \frac{d}{\Delta p},$$

where δ = water vapour permeability [kg/(Pa·s·m)]
Δm = change in weight [kg]
A = the area of the specimen [m²]
t = time [s]
d = thickness of the specimen [m]
Δp = partial pressure gradient

The mix of the mortar was the same than used in the electrochemical measurements (Mix 1): The mortar mix contained OPC and sand (0-0.6 mm) in the weight proportions of 1:4.5. The water/cement ratio of the mix was 1.08. To enable fast carbonation the thickness of the specimens was minimised. The specimens were 103 mm in diameter and the thickness was 2.7 mm ± 0.2 mm (Fig. 4).

After a 3 weeks curing in water immersion (water 40 °C) and subsequent drying the specimens were placed in rings with inner diameter of 103 mm with melt glue. The rings were placed on the top of the cups. The joints were sealed with adhesive tape. Two "blind" cups with impermeable specimens were also prepared to reveal the possible leaks through the joints.

During the first measurements the specimens were alkaline. One half of the specimens were then carbonated accelerated in 4 % CO_2 and 75 ± 5 % relative humidity for 3 months. The other half of the specimens were carbonated normally in 0.04 %-vol CO_2 and 70 % relative humidity for 6 months. The progress of carbonation depths was determined by the means of phenolphthalein test. The 2nd test was started when the specimens were carbonated through. All the specimens were stored at 0.04 %-vol CO_2 and 70 % RH for one week before testing.

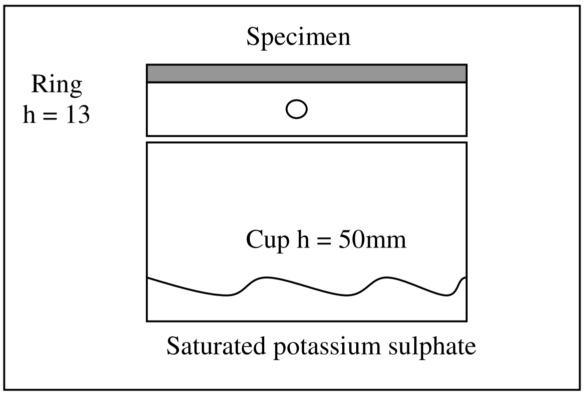

Figure 4 – Specimens of type 3.

2.3 Water absorption test

In water absorption tests dry specimens are immersed in water completely or partly. The water suction is determined by weighing the specimens periodically. Water absorption coefficient is calculated according to the following equation:

$$A = \frac{m}{\sqrt{t}},$$

where A = water absorption coefficient [kg/m^{2}s]
m = the change in weight /the area of the specimen [kg/m^2]
t = time [$\sqrt{\text{s}}$]

In this research the specimens were stored at RH ~ 0 %, and the drying was followed by weighing the specimens. When the change in weight had become steady, the specimens were placed in vacuum to finish the drying.

The specimens were prepared of the same pieces from a demolished concrete shelter than specimens of type 2 used in the electrochemical measurements. The carbonation front was measured and the specimens were sawed to specified size. A piece of concrete containing both alkaline and carbonated concrete was cut from the carbonation zone. The opposite surfaces (in two different specimens) with similar properties were reached: the other specimen was alkaline and the other carbonated. The water absorption tests were performed for the both specimens. After this the alkaline specimens were accelerated carbonated for 10-12 weeks and the tests were performed again.

The dry specimens were covered with water vapour impermeable covering. Only the sawed surface was exposed to moisture by capillary contact to free water. The specimens were weighted in the time of 1 min, 2 min, 3 min, 4 min, 5 min, 7 min, 10 min, 15 min, 20 min, 30 min, 45 min and 1 h.

The water suction to the alkaline parts of the specimens is affecting the results after the first minutes, so the emphasis was in the first 5 minutes of the test.

3. RESULTS

3.1 Corrosion potential and corrosion rate

The corrosion potential of specimens, which were carbonated in two kinds of conditions were monitored to find out any differences between their corrosion tendencies. The corrosion rates of specimens were monitored by the polarisation resistance method.

3.1.1 Specimens of type 1, Mix 1

The specimens were monitored when immersed in water. The corrosion potential measurements were carried out using a standard SCE electrode. The monitoring was made in three periods. At first, the specimens were monitored after 30 min, 3 h and 6 h immersion in water. After the first test the specimens were dried up for one week in RH 75 % after which the measurements were performed again. This time the readings were taken after 20 h and 1 week immersion. Before the 3rd monitoring the specimens were stored at RH 75 % for one week. The specimens were then monitored after 30 min, 3 h, 6 h, 24 h and 7d immersion in water.

The results from potential monitoring are presented in Figure 5 and the results from corrosion rate monitoring in Figure 6. All presented values are means of measurements on five specimens.

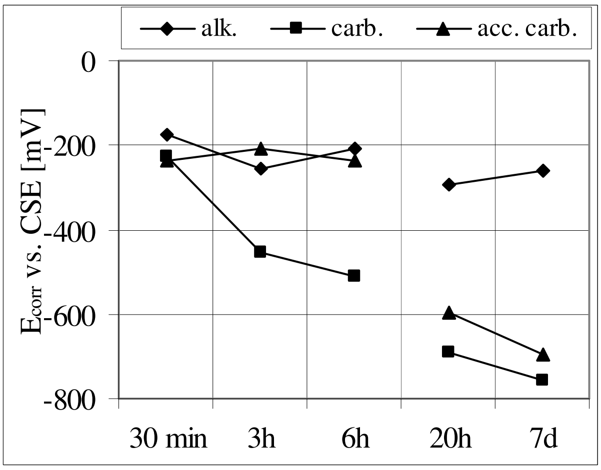

Figure 5 – The potentials of Specimens 1, Mix 1. (alk.=alkaline, carb.=carbonated in 0.04 %-vol CO_2, acc. carb.=accelerated carbonated in 4 %-vol CO_2).

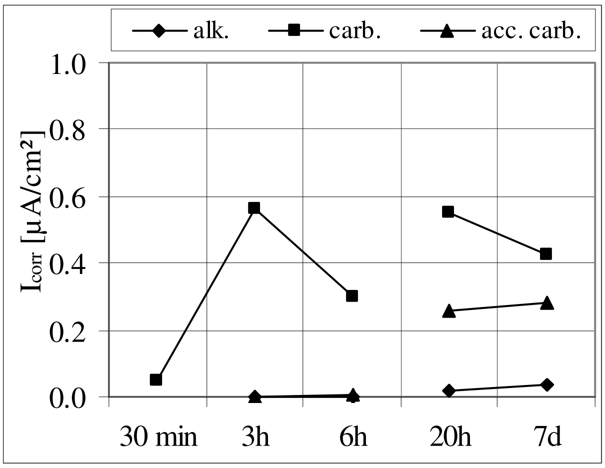

Figure 6 – The corrosion rates of Specimens 1, Mix 1. (alk.=alkaline, carb.=carbonated in 0.04 %-vol CO_2, acc. carb.=accelerated carbonated in 4 %-vol CO_2).

In the beginning of the test, the specimens were relatively dry (stored at RH 75 %) and after 30 minutes immersion the potentials were still high. Potentials of alkaline specimens were in the passive zone (>-200 mV vs. CSE) and during the test they fell into the uncertain range (-200 … -350 mV vs. CSE). The results of corrosion rate monitoring were congruent with the results of potential. The corrosion rates of alkaline specimens were below 0.1 µA/cm² (negligible corrosion) and grew a little by the end. It is possible that the passive layer weakened during the long immersion due to depletion of oxygen.

During the 1st monitoring, the potentials of carbonated specimens were in the uncertain range (-200 … -350 mV vs. CSE) after 30 minutes. The corrosion protection due to the passivation was rapidly lost in normally carbonated specimens: After 3 hours immersion in water, the potentials were below –350 mV and the corrosion rates > 0.5 µA/cm² (moderate).

At first, the corrosion was slow in accelerated carbonated specimens. The potentials remained high (>-200 mV or –200 … -350 mV) i.e. the corrosion protection was not lost during the first monitoring. The accelerated carbonated specimens lost their corrosion protection ability during the 2nd test. After 20 hours immersion the potentials were below –350 mV and the corrosion rates were observable.

The specimens were stored at RH 75 % for one week before the 3rd test started (results in Figures 7 and 8). In this time, the corrosion rates of carbonated specimens were immediately quite high (>1.0 µA/cm², high corrosion rate). There was no significant difference between normally and accelerated carbonated specimens after 30 minutes immersion. The corrosion started to decrease in time: in accelerated carbonated specimens after 30 minutes and in normally carbonated specimens after 6 hours. After 7 days the mean corrosion rate of normally carbonated specimens was 0.9 µA/cm² and in accelerated carbonated 0.8 µA/cm² (representing both moderate corrosion). Also the corrosion potentials decreased during the second test.

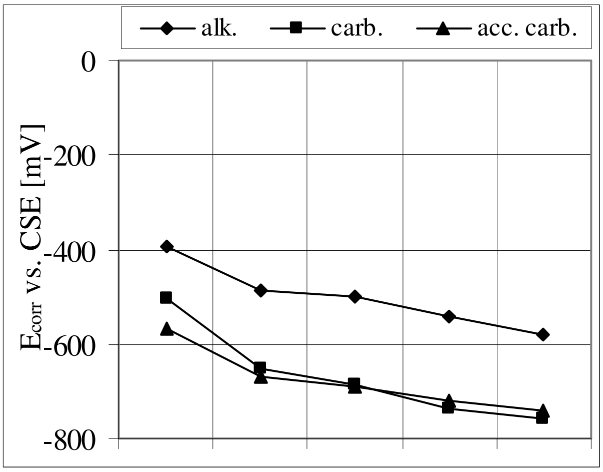

Figure 7 – The potentials of Specimens 1, Mix 1 during 3rd test.
(alk.=alkaline, carb.=carbonated in 0.04 %-vol CO_2, acc. carb.=accelerated carbonated in 4 %-vol CO_2).

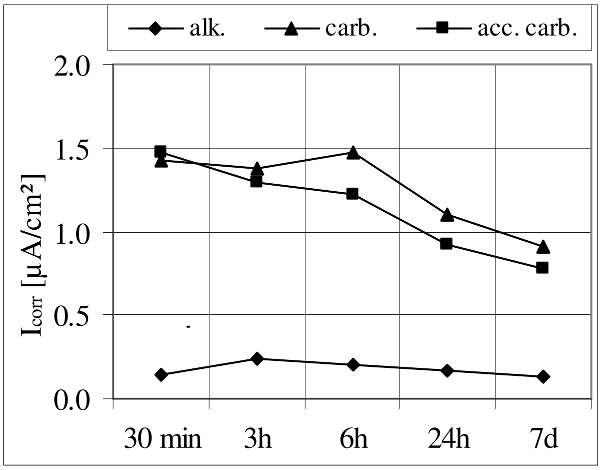

Figure 8 – The corrosion rates of Specimens 1, Mix 1 during 3rd test.
(alk.=alkaline, carb.=carbonated in 0.04 %-vol CO_2, acc. carb.=accelerated carbonated in 4 %-vol CO_2).

3.1.2 Specimens of type 1, Mix 2

The curing, carbonation and storing of the specimens were similar than with specimens of Mix 1.

The results from potential monitoring are presented in Figure 9 and the results of corrosion rate monitoring in Figure 10. All presented values are means of measurements on five specimens.

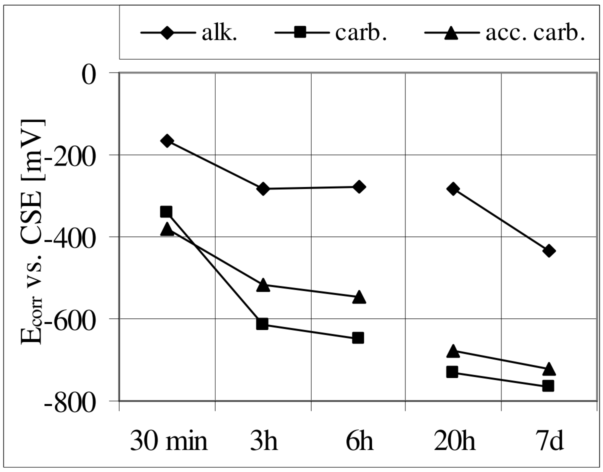

Figure10 – The corrosion rates of Specimens 1, Mix 2.
(alk.=alkaline, carb.=carbonated in 0.04 %-vol CO_2, acc. carb.=accelerated carbonated in 4 %-vol CO_2).

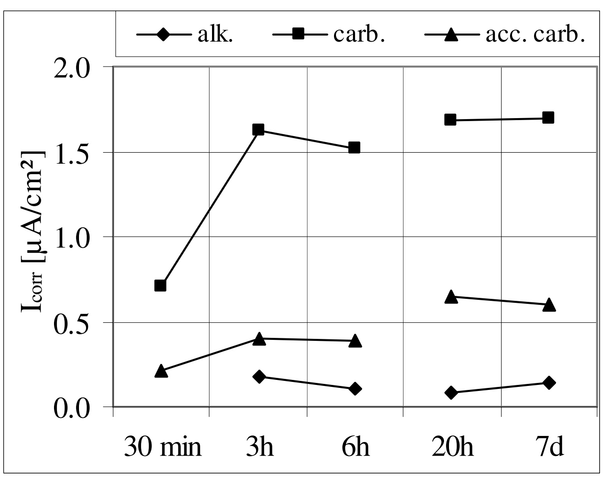

The loss of corrosion protection by depassivation was very similar with normally and accelerated carbonated specimens. Within 3 hours the corrosion potentials of them had dropped to zone < -350 mV.

Corrosion in the normally carbonated specimens was fast (> 1.0 µA/cm²) after 3 hours. Even after 30 minutes, the corrosion rate was higher than 0.50 µA/cm² (moderate corrosion).

The corrosion rate in accelerated carbonated specimens was much slower: < 0.50 µA/cm² during the 1st test and around 0.6 µA/cm² during the 2nd test.

Corrosion in the alkaline specimens was negligible.

The results from 3rd potential and corrosion rate monitoring are presented Figures 11 and 12. The corrosion rates of carbonated specimens were immediately after 30 minutes really high (>3.0 µA/cm²). The corrosion in the normally carbonated specimens was faster than in accelerated carbonated specimens. The corrosion started to decrease in time. After 7 days the mean corrosion rate of normally carbonated specimens was 2.4 µA/cm² and 1.2 µA/cm² in the accelerated carbonated specimens (both fast corrosion). The corrosion potentials decreased during the third test.

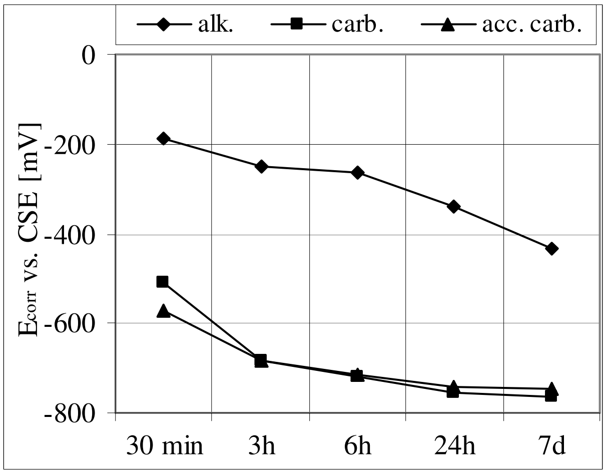

Figure 11 – The potentials of Specimens 1, Mix 2 during 3rd test.
(alk.=alkaline, carb.=carbonated in 0.04 %-vol CO_2, acc. carb.=accelerated carbonated in 4 %-vol CO_2).

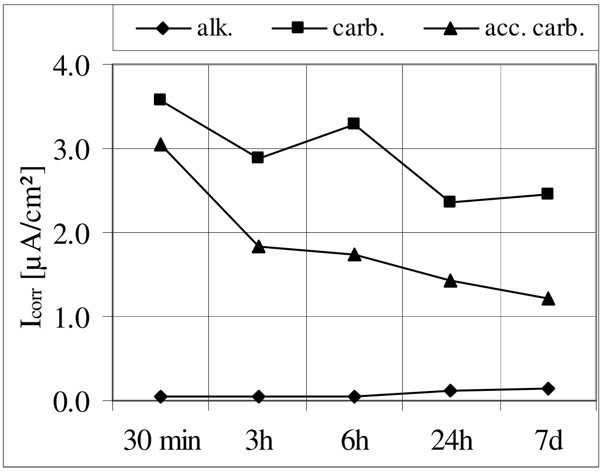

Figure 12 – The corrosion rates of Specimens 1, Mix 2 during 3rd test.
(alk.=alkaline, carb.=carbonated in 0.04 %-vol CO_2, acc. carb.=accelerated carbonated in 4 %-vol CO_2).

3.1.3 Specimens of type 2

With these specimens it was impossible to compare the initiation of the corrosion because of the different thickness of the concrete covering. The objective was to found out whether the corrosion is in longer term as fast in accelerated carbonated concrete than in naturally carbonated concrete.

Corrosion potentials of working electrodes were monitored unconventionally by using passive steel bars in alkaline concrete as a reference.

Before testing the specimens were stored at RH 75 % and 20 °C. The monitoring was made in two parts. First the specimens were laid down on wet cloths which were in contact with water (air RH 75 %, 20 °C). The specimens were monitored after 4 h, 1 d, 2 d, 4 d and 1 week contact with water. After the first test the specimens were removed to conditions of RH 97 % with no water contact. This time the readings were taken after 1, 2, 3 and 4 weeks after moving in 97 % RH.

The results of corrosion potential monitoring are presented in Figure 13. The results of corrosion rate monitoring are presented in Figure 14. Presented values are means of measurements on 8-10 specimens.

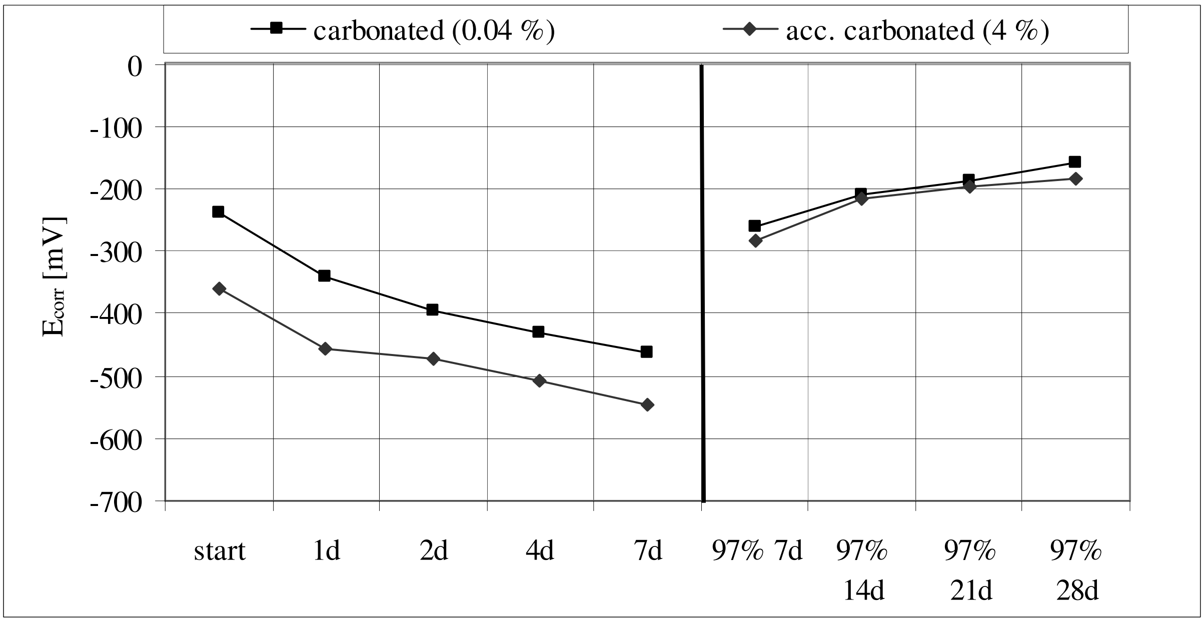

Figure 13 – The results of potential measurements (Specimens of type 2).

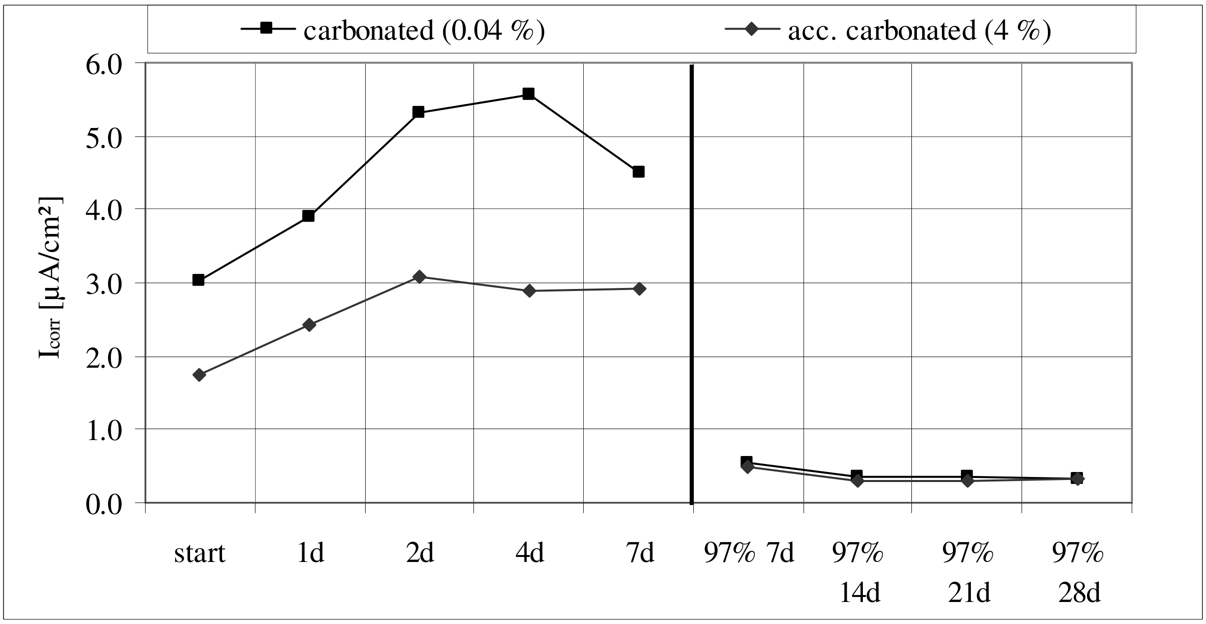

Figure 14 – The results of corrosion rate measurements (Specimens of type 2).

The corrosion potentials dropped to the level -450 … -550 mV in one week. After the water contact was removed and the specimens were stored at RH 97 %, the corrosion potentials raised remarkably. After 4 weeks the corrosion potential was so high that the probability of corrosion was minor.

The maximum corrosion rate was achieved rapidly after the specimens were laid in contact with water. The corrosion in naturally carbonated specimens was somewhat higher than in acceleratedly carbonated specimens. The corrosion rate of accelerated carbonated specimens was about 35 % smaller after 7 days than in normally carbonated specimens.

In RH 97 % the corrosion was low in both cases.

3.2 Cup tests

The results of cup tests are presented in Table 3. All the values presented in the table are means of measurements on four identical specimens.

Table 3 – The permeability related quantities calculated from the results of cup tests.

		CO_2 0.04 %		CO_2 4 %	
		alkal.	carb.	alkal.	carb.
Water vapour diffusion resistance (Z)	10^9 [m²sPa/kg]	1.58	1.08	1.67	1.24
Water vapour permeability (δ)	10^{-12} [kg/msPa]	1.77	2.56	1.62	2.16

The water vapour permeability is known to be a moisture-dependent material property. To determine an exact value, the cup test should be performed in different moisture levels. In this study the aim was not to determine the exact value, but to find differences between specimens.

The mean δ of normally carbonated specimens was 2.6 kg/msPa and mean δ of accelerated carbonated specimens 2.2 kg/msPa. The changes during carbonation were correspondingly 45 % and 34 %. The results of single specimens are presented in Table 4.

The other blind cup had a little leakage. This may have influenced the results.

Table 4 – The single results of cup test method.

		Water vapour permeability [δ] 10^{-12} [kg/msPa]		Water vapour diffusion resistance [Z] 10^{9} [m²sPa/kg]	
		alkaline	carbonated	alkaline	carbonated
CO_2 0.04%	1d	1.72	2.50	1.69	1.16
	1e	1.94	2.45	1.27	1.01
	1f	1.59	2.59	1.78	1.10
	1g	1.83	2.72	1.58	1.07
CO_2 4%	2d	2.00	2.62	1.30	0.99
	2e	1.33	1.92	2.10	1.46
	2f	1.39	1.83	1.84	1.40
	2g	1.75	2.29	1.45	1.11
Blind cups	T1	0.02	0.12	117.66	17.08
	T2	0.00	0.01	∞	168.34

3.3 Water absorption test

The curves of water absorption were determined for each specimen and the water absorption coefficients were calculated. The curve of one specimen is presented as an example in Figure 15. The other curves were almost identical. It can be seen from the curve, that the change in weight was the fastest when the specimen was alkaline. Carbonation clearly retarded water absorption. The effect was bigger when accelerated carbonation was used.

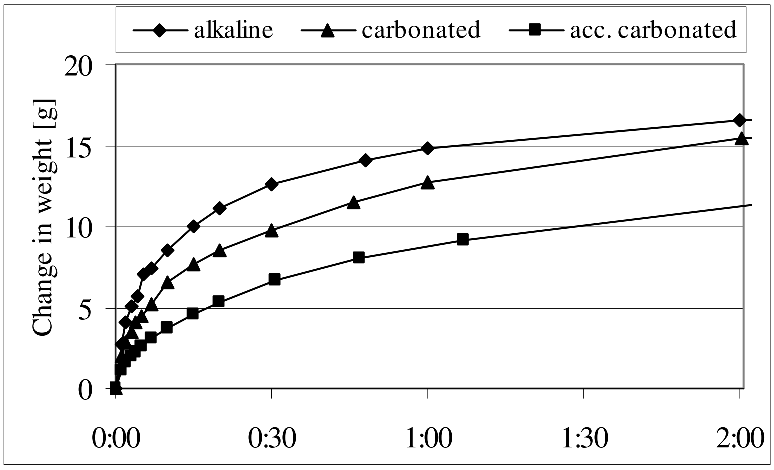

Figure 15 – The curve of water absorption.

The water absorption coefficients of each specimen after 1 and 5 minutes are presented in Figures 16 and 17. The carbonated and the alkaline surfaces are reached from same pieces of concrete (Fa…Vd) by removing concrete from the carbonation zone. The accelerated carbonated surface is the alkaline surface after carbonation.

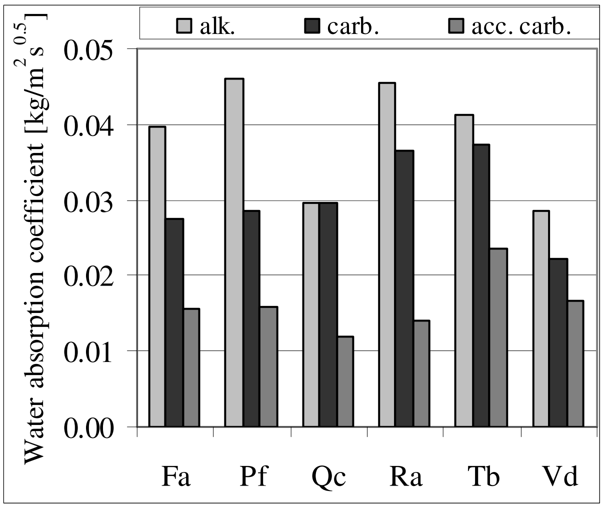

Figure 16 – The water absorption coefficients recorded after 1 minute.
(alk.=alkaline, carb.=carbonated in 0.04 %-vol CO_2, acc. carb.=accelerated carbonated in 4 %-vol CO_2).

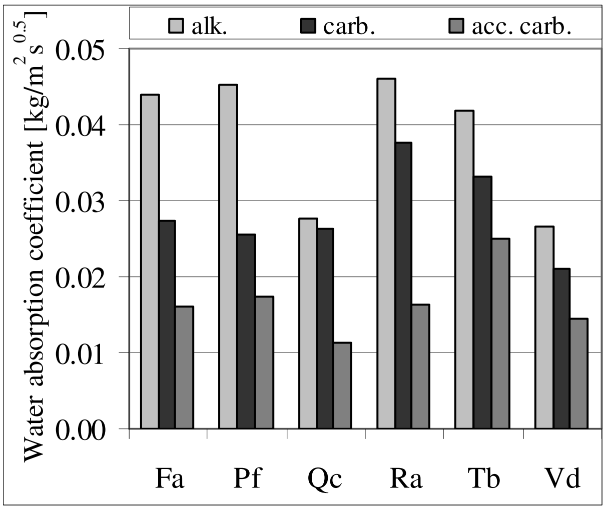

Figure 17 – The water absorption coefficients recorded after 5 minutes.
(alk.=alkaline, carb.=carbonated in 0.04 %-vol CO_2, acc. carb.=accelerated carbonated in 4 %-vol CO_2).

After 1 hour the water front had reached the alkaline parts of the specimens and the water absorption coefficients of carbonated specimens were higher.

4. DISCUSSION

The corrosion rate of specimens made of Mix 1 was slower in accelerated carbonated specimens than in naturally carbonated specimens. In the 1st test, the mean rate of accelerated carbonated specimens was 34 – 38 % smaller than in normally carbonated specimens. In the 2nd test the mean rate of accelerated carbonated specimens ended up to be 15 – 20 % smaller than in normally carbonated specimens.

During the 1st test the corrosion rates increased during the tests because the corrosion was starting. Immediately in the beginning of the 2nd test the corrosion rates reached their maximum and decreased by time possible due to depletion of oxygen.

The corrosion in specimens made of Mix 2 was much faster than in specimens made of Mix 1. In the 1st test, the mean rate of normally carbonated specimens was 3-4 times faster during the first 6 hours and later 2-3 times faster than in accelerated carbonated specimens. In the 2nd test the difference was smaller: mean rate of normally carbonated specimens was 1.2-2 times of that in accelerated carbonated specimens.

Monitoring of specimens 2 indicated also that corrosion is faster in naturally carbonated specimens: the mean corrosion rate in accelerated carbonated specimens was 35 % slower than in naturally carbonated specimens.

The water vapour permeability of the specimens increased during carbonation. This is contradictory with the common understanding, but also corresponding results are being introduced /5/. There were no significant differences between accelerated and normally carbonated specimens. The water vapour permeability of accelerated carbonated specimens was 16 % smaller than in normally carbonated specimens. The scatter of the results was quite wide which may have been caused by leakages from the cups or by measuring errors. In small number of specimens even one difference may affect the results remarkable.

According to the water absorption tests, the carbonation makes the concrete denser. This effect is more pronounced in accelerated carbonated specimens than in naturally carbonated ones. The water absorption coefficients of accelerated carbonated parts were approximately 40 % smaller than in naturally carbonated parts during the first 5 minutes. It was impossible to perform the tests to all groups of specimens in the same time because of the frequent weighing. That's why the results may have been affected for example by the drying of the specimens and different initial moisture content.

5. CONCLUSIONS

The data of this study shows that there are some differences between natural and accelerated carbonation.

Carbonation reaction generally causes a reduction in porosity. According to this study the effect may be more pronounced when using accelerated methods. The water vapour permeability and water absorption coefficients of accelerated carbonated specimens were smaller than in normally carbonated specimens. The effect was also observed as differences in resistivity: The corrosion rate was 15-50 % smaller in accelerated carbonated specimens (4 %-vol CO_2) than in naturally carbonated specimens (0.04 %-vol CO_2).

According to the results of this study, the corrosion rate results received with accelerated carbonation may be 15 - 40 % smaller than in naturally carbonated concrete. This should be taken into consideration when using accelerated carbonation for studying corrosion. However accelerated carbonation enables corrosion of steel to start much earlier which is a remarkable benefit when studying corrosion of steel.

REFERENCES

1. Parrot L.J., “A review of carbonation in reinforced concrete”, Cement and Concrete Association, Wexham Springs, 1987.
2. Bakker R., “Initiation period,” Schiessl P. (editor), Corrosion of steel in concrete, Chapman and Hall, London, 1988
3. Claisse et al., ”Permeability and Pore Volume of Carbonated concrete” European concerted action, Final report, Brussels, 1997
4. Richardsson M.G., “Carbonation of reinforced concrete: Its Causes and Management” Civil Engineering Department, Ireland, 1988
5. Häkkinen T., “Influence of high slag content on the basic mechanical properties and carbonation of concrete” VTT Building Materials Laboratory, Espoo, 1993 (in Finnish)
6. Tuutti, K., “Corrosion of Steel in Concrete” Swedish Cement and Concrete Institute, Stockholm, 1982
7. Dunster, A.M., “Accelerated carbonation testing of concrete” BRE, Information paper, December, 2000

8. Sulankivi H., Tiililaatan vaikutus betonin karbonatisoitumiseen, diplomityö, Tampere, 1993 (in Finnish)
9. Neville, A.M., “Properties of Concrete” Longman Scientific & Technical, Singapore, 1988
10. Papadagis V.G. et al., “Fundamental Modelling and Experimental Investigation of Concrete Carbonation” ACI Materials Journal, V. 88, NO. 4, July-August, 1991
11. Page C. L., “Basic Principles of Corrosion” Schiessl P. (editor), Corrosion of steel in concrete, Chapman and Hall, London, 1988
12. Mattila J., “On the Durability of Cement-Based Patch Repairs on Finnish Concrete Facades and Balconies” Doctoral thesis, Tampere University of Technology, Structural Engineering, Tampere, 2003
13. Anon., “Standard test method for half-cell potentials of uncoated reinforcing steel in concrete” ASTM C876-91, The American Society for Testing and Materials, 1999
14. COST 509, Corrosion and protection of metals in contact with concrete, European concerted action, Final report, Brussels, 1997
15. Andrade C., “Measurement of Polarization Resistance on-site” COST Action 521, Corrosion of steel in reinforced concrete structures, Final report, 2003

Limestone Filler as Addition in Cement Mortars: Influence on the Early-Age Strength Development at Low Temperature

Monica Lundgren
M. Sc. Civ. Eng.
SP Swedish National Testing and Research Institute
P.O. Box 857, SE-501 15 Borås
E-mail: monica.lundgren@sp.se

ABSTRACT

Limestone filler is increasingly used, among other things as replacement for clinker in cement and as addition to self-compacting concrete. There are research results presented in the literature on how limestone filler affects the material properties of concrete but still much knowledge is lacking. This is relevant not least for young concrete used at low temperatures under winter conditions. This paper presents results from an investigation aiming to increase knowledge on the performance of limestone filler under cold, severe climatic conditions. The main focus is on the strength development of young concrete.

The results clearly indicate that curing temperature significantly influences the efficiency of limestone filler. The efficiency increases with decreasing temperature.

Key words: cement, early-age, efficiency, limestone filler, low temperature, strength.

1. INTRODUCTION

1.1 Background

The use of limestone filler in concrete has increased considerably during the last decade. Limestone is partly used as replacement for clinker in cement. In Sweden, for example, the most common cement today is a Portland-limestone cement with a limestone content of about 15 %, corresponding to CEM II/A-LL in EN197-1 [1]. Limestone filler is also used in self-compacting concrete (SCC) in order to improve the rheological properties and the stability. Typical quantities for SCC are about 100 kg limestone filler per m^3 of concrete.

It has been observed that limestone filler sometimes has a positive effect on strength and strength development. A so-called "filler effect" is given as reason for this influence. The mechanisms behind this effect are not fully understood but they are mostly considered to be of a physical nature, e.g. by filling voids between grains of cement clinker. Goldman and Bentur [2] suggest that a fine filler, with particle size smaller than 0.073 µm, even though inert, increases strength in concrete because the transition zone between the paste and the aggregates becomes denser. According to the authors this effect of physical nature, called "microfiller effect", is present also when reactive fillers are used, e.g. silica fume, and can be at least as significant as the pozzolanic effect on the development of strength in concrete.

Limestone filler is normally considered to be an inert material, although its effects may also be of chemical nature [3], implying among other things increased rate of reaction of the C_3S. A chemical activity of the limestone filler when used in cement and concrete is also sustained by some more recent studies. Bonavetti et al [4] indicated an increased degree of hydration in cement pastes due to the presence of limestone filler. Tsivilis et al [5] found increased amount of CH and of non-evaporable water in limestone cement paste, which would imply an improved hydration of the alite. Studies by Péra et al [6] suggest an accelerating effect of limestone on the hydration of cement and show that different hydration products are formed due to the presence of $CaCO_3$. A general observation is that transformation of ettringite into monosulfate is delayed by the calcium carbonate [3, 7, 8].

Although a number of studies have been dealing with limestone as filler in concrete it is still not fully understood how the use of limestone filler influences the concrete strength, or which are the mechanisms behind the effect of limestone filler on the strength development in concrete. Almost all the studies presented in the literature are carried out at room temperature and at an age of about a month. Very little, if anything, is presented about the effect of limestone filler on the strength development at temperatures below 20 °C and at early age.

This paper presents results from a project where the early-age strength development at low temperature has been studied for concrete containing limestone filler. Limestone filler produced of carbonated rocks from different quarries and with different finenesses have been studied, in combination with parameters like the water-binder ratio of the mixture, age and temperature.

In EN 206-1 [9] the efficiency of type II additions, i.e. reactive ones such as most fly ashes and slags, is given by the *k*-value. The *k*-value defines how many parts by weight of ordinary Portland cement can be replaced by one part of a specified mineral addition without changing the concrete properties, especially where durability aspects are concerned. In this paper, however, the *k*-value concept is used also for limestone filler in order to be able to compare quantitatively the efficiency of different types and qualities of fillers and how they influence the early-age strength development at low temperature.

Tests have been carried out at two different temperatures: 5 °C as the main low temperature and 20 °C as a reference. The reason is that for structures in many regions, for example in the Nordic countries, the temperature at casting and curing lies many degrees below the standard laboratory temperature 20–23 °C. In order to perform efficient and safe construction it must be possible to estimate the strength development at early ages and low temperatures for all types of concrete, also for those containing limestone filler and other types of materials substituting cement and aggregates in concrete.

2. EXPERIMENTAL PROGRAMME

2.1 Materials

Ordinary Portland cement (**OPC**) of type CEM I 52.5 R was used as main binder in cement mortars, manufactured with Portland cement as the only binder, and in blended mortars, manufactured with cement and limestone filler. Limestone filler was studied as an addition to the mortar. It was included as part of the total amount of binder, replacing part of the cement on the basis of percent by mass of the total amount of binder. The binder content is defined in this paper as the total mass of cement and limestone filler.

Mortar mixtures were manufactured with CEN standard sand and deionised water, in principle according to EN 196-1 [10]. No chemical admixtures were used. The cement and the limestone filler qualities used are described in Tables 1 and 2.

Table 1 – Cement: clinker composition and physical properties.

Cement	C_3S (%)	C_2S (%)	C_3A (%)	C_4AF (%)	Particle size Top cut $d_{98\%}$ (μm)	Mean $d_{50\%}$ (μm)	Specific surface Blaine (m^2/kg)	BET (m^2/kg)
CEM I 52.5R (**OPC**)	62.8	12.4	5.5	8.3	~ 32	~ 7.5	541	1760

Limestone is a sedimentary calcium carbonate rock formed through sedimentation. Despite identical chemical composition, rocks from different deposits may vary considerably. Crystal shape and size, porosity, hardness and reactivity during processing may be very different in rocks formed in different environments. A characterization of some of these parameters is given in [11]. There are three distinct types of limestone:

- chalk, a younger, microcrystalline rock, produced by the sedimentation of shells of small fossils
- limestone, a more compact sedimentary rock, with a crystal size between that of chalk and that of marble
- marble, a metamorphic rock with coarse crystals, formed when chalk or limestone recrystallised under conditions of high temperature and high pressure.

In order to analyse if differences in mineral properties have any influence on the early-age strength development, blended mortars were manufactured with cement and each of these types of limestone, as addition. Powders of high-purity chalk (**CH**), limestone (**LL**) and marble (**MA**), with a particle size distribution close to the particle size distribution of the cement used (**OPC**), were used for a comparison independent on fineness.

Table 2 – Limestone: chemical composition and physical properties.

Limestone	$CaCO_3$ (%)	Particle size Top cut $d_{98\%}$ (μm)	Mean $d_{50\%}$ (μm)	Specific surface BET (m^2/kg)
Chalk (**CH**)	≥ 98%	~ 30	~ 2.3	2200
Marble (**MA**)	≥ 98%	~ 30	~ 7	1500
Limestone (**LL**)	≥ 98%	~ 30	~ 5.5	1000
Limestone, coarse fraction (**LLC**)	≥ 98%	~ 70	~ 22	700
Limestone, fine fraction (**LLF**)	≥ 98%	~ 3	~ 0.44	15000

For the study of the influence of the fineness of the limestone two more powders were studied:
- a very fine fraction (**LLF**), comparable with the limestone fraction found in the Swedish Portland-limestone cement of type CEM II/A-LL, and a coarse fraction (**LLC**) comparable with the particle size distribution of a common limestone filler used in self compacting concrete. The two fractions LLC and LLF are of same type and from the same quarry as limestone LL.

2.2 Mixtures and tests

The use of limestone as addition was studied primarily on mortar mixtures with 24% limestone, tested for compressive strength at the age of 2 days and 7 days, at 5 °C and 20 °C respectively. Limestone type LL was studied over a range of water-binder ratio of 0.4 to 0.7. Comparison was made between cement mortars with *W/C* = 0.4–0.7 and blended mortars manufactured with the same amounts of water, sand and binder, but by using a mixture of cement and limestone filler as binder.

Comparisons between limestone (LL) and marble (MA) or chalk (CH) and the influence of the fineness (LL versus LLF and LLC) were made on mixtures with *W/B* = 0.5. This comparison between different type and fineness of limestone filler was also made at 12% limestone content, however only limited at the test temperature of 5 °C.

A content of 12% limestone filler is comparable with the amount of limestone in the Swedish Portland-limestone cement CEM II/A-LL 42.5 R. 24% limestone is slightly higher than the amount of limestone allowed in a cement CEM II/A-L, but the reason for studying this amount was based on the assumption that, at a higher amount, the efficiency of limestone addition could be better recognized due to a smaller scatter of the results, see for example [12].

Mortar prisms, 40 x 40 x 160 (mm), were manufactured and tested in principle by following the procedures in EN 196-1 [10]. However, some deviations from the standard procedures were made, to adjust to the purpose of this investigation:

- mixture proportions were changed, to be able to test mixtures with *W/B* = 0.4–0.7 and having similar consistence,
- the temperature at manufacture, curing and test was 5 °C and, for some test alternatives, also 20 °C for comparison,
- the binder consisted of cement and limestone (parts of the cement replaced by limestone, 1:1 by mass).

The proportions of the mixtures were chosen with consideration to the consistence of the fresh mortar. This was measured on a flow table according to EN 1015-3. Starting with the consistence obtained at 20 °C for a standard mortar with the proportions water:cement:sand 225:450:1350 (g), new mixtures were set up to reach similar consistence at *W/C* = 0.4, 0.6 and 0.7. Then new mixture proportions were determined at 5 °C, to obtain mortars with same consistence for these *W/C*.

However, for the purpose of this research it was more suitable to use the same proportions at both 5 °C and 20 °C for each *W/C*. Therefore the intermediary proportions shown in Table 3 were chosen, yielding not the same but comparable consistence. Blended cement-limestone filler mixtures with *W/B* = 0.4–0.7 were manufactured with the same proportions water:powder:sand as the mixtures, but with parts of the cement replaced with limestone.

Table 3 shows the mixture composition of the tested mortars. Cement mixtures were labelled according to the rule *binder-W/C*. Blended mixtures were labelled according to the rule *limestone type and amount - W/B*. The type of limestone filler was coded LL, LLF, LLC, MA or CH and the amount of filler (12 or 24) as percent of the total amount of binder.

Table 3 – Mixture composition. Amounts per batch needed for the manufacture of three mortar prisms 40mm x40mm x160mm.

Cement mortars	W/C	Water (g)	Cement (g)	Sand 1) (g)	Blended mortars	W/B 2)	Cement (g)	Limestone (g)	W/C
OPC-0.4	0.4	288	720	1350	LL24-0.4	0.4	547.2	172.8	0.53
OPC-0.5	0.5	240	480	1350	LL12-0.5, LLF12-0.5, LLC12-0.5, MA12-0.5, CH12-0.5	0.5	422.4	57.6	0.57
					LL24-0.5, LLF24-0.5, LLC24-0.5, MA24-0.5, CH24-0.5	0.5	364.8	115.2	0.66
OPC-0.6	0.6	217.5	362.5	1350	LL24-0.6	0.6	275.5	87	0.79
OPC-0.7	0.7	210	300	1350	LL24-0.7	0.7	228	72	0.92

1) Same amount of sand was used in both cement mortars and blended mortars.
2) Water/binder ratio = water/(cement + limestone), by mass.

All the constituent materials were pre-stored at 5 °C or 20 °C before starting manufacturing the specimens. The prisms were manufactured, compacted, stored and tested in climate rooms with constant temperatures, 5 °C or 20 °C respectively. After mixing, the prisms were compacted while in mould, on a vibrating table: 2 times 60 s, at a frequency of 50 Hz and an amplitude of 0.75 mm. The prisms were cured in moulds for one day, sealed against evaporation, and then stored in lime-saturated water until testing.

The main test temperature was 5 °C, but most mixtures were tested at 20 °C as well, for comparison with the standard laboratory temperature. The test alternatives are shown in Table 4.

Table 4 – Test alternatives: type of binder and W/B per test age and test temperature.

Temperature	Binder	Test age 2 days	Test age 7 days	Test age 28 days
5 °C	OPC	0.4, 0.5, 0.6, 0.7	0.4, 0.5, 0.6, 0.7	0.4, 0.5, 0.6, 0.7
	OPC 88% Limestone 12%	LL, LLF, LLC, MA, CH 0.5	LL, LLF, LLC, MA, CH 0.5	LL 0.5
	OPC 76% Limestone 24%	LL 0.4, 0.5, 0.6, 0.7 LLF, LLC, MA, CH 0.5	LL 0.4, 0.5, 0.6, 0.7 LLF, LLC, MA, CH 0.5	LL 0.5
20 °C	OPC	0.4, 0.5, 0.6, 0.7	0.4, 0.5, 0.6, 0.7	0.4, 0.5, 0.6, 0.7
	OPC 88% Limestone 12%	LL 0.5	LL 0.5	LL 0.5
	OPC 76% Limestone 24%	LL 0.4, 0.5, 0.6, 0.7 LLF, LLC, MA, CH 0.5	LL 0.4, 0.5, 0.6, 0.7 LLF, LLC, MA, CH 0.5	LL 0.5

Strength was determined according to EN 196-1. Three prisms per mixture were tested by three-point flexure test, followed by compressive strength testing on the resulting six half-prisms. The test ages were 2 days and 7 days, ± 10 minutes. Tests at 28 days were beyond the purpose of this research. However, for a comparison with the standard age, cement mixtures and blended mixtures LL24-0.5 and LL12-0.5 were tested at 28 days as well. See Table 4.

3 RESULTS

This paper presents the test results of the compressive strength (f_c). Based on the compressive strength, the efficiency coefficients (*k*-values) for the different types of limestone fillers were calculated.

Table 5 shows the compressive strength for the cement mortars, as mean of six values per mixture, and the variation between the lowest and highest test values.

Table 5 – Test results: compressive strength for cement mortars.

Cement mortars	W/C	Air1) %	f_c mean value (MPa)	f_c min-max (MPa)	Air1) %	f_c mean value (MPa)	f_c min-max (MPa)
			2 days 5°C			**2 days 20°C**	
OPC-0.4	0.4	1.7	46.4	44.7-46.9	1.6	62.4	62.1-63.7
OPC-0.5	0.5	2.3	28.0	27.5-28.6	2.2	46.8	44.7-47.5
OPC-0.6	0.6	2.5	17.6	17.0-18.3	1.8	34.8	33.6-35.5
OPC-0.7	0.7	2.5	11.0	10.7-11.2	1.7	25.0	24.4-25.6
			7 days 5°C			**7 days 20°C**	
OPC-0.4	0.4	1.7	71.6	70.4-73.2	1.7	71.6	70.1-73.1
OPC-0.5	0.5	2.2	53.7	53.1-54.2	1.9	58.8	58.3-59.6
OPC-0.6	0.6	2.6	38.5	38.5-39.1	1.9	45.2	44.4-46.2
OPC-0.7	0.7	3.2	26.2	25.6-27.1	1.5	33.8	33.2-34.1
			28 days 5 °C			**28 days 20°C**	
OPC-0.4	0.4	2.5	84.0	80.7-86.2	1.7	83.2	81.8-84.2
OPC-0.5	0.5	2.6	67.4	66.6-68.1	2.2	65.45	64.9-66.2
OPC-0.6	0.6	2.4	52.7	50.9-53.7	2.3	50.40	48.9-51.7
OPC-0.7	0.7	1.9	39.3	38.7-39.7	1.8	40.33	39.3-41.2

1) Natural air content in the mortar.

Table 6 shows the results for the blended mortars. Strength results are shown as mean, lowest and highest test value. The natural air content in the blended mortars was similar, of same magnitude, as the air content in the cement mortars. Therefore these values are not shown, for the sake of simplicity of the table.

Table 6 shows also the efficiency coefficients, *k*-values, of the different fillers in different mixtures.

Table 6 – Test results: compressive strength for blended mortars and k-values for limestone.

Blended mortars	W/B	f_c mean (MPa)	f_c min-max (MPa)	k 1) mean	k 1) min-max	f_c mean (MPa)	f_c min-max (MPa)	k 1) mean	k 1) min-max
			2 days 5 °C				**2 days 20 °C**		
LL12-0.5	0.5	23.7	23.5-24.0	0.43	0.37-0.46	40.3	40.1-40.7	0.28	
LLF12-0.5	0.5	29.6	29.2-30.0	1.17	1.12-1.21				
LLC12-0.5	0.5	22.2	21.7-22.6	0.22	0.13-0.25				
MA12-0.5	0.5	24.7	24.3-25.4	0.52	0.49-0.64				
CH12-0.5	0.5	24.8	24.3-26.0	0.55	0.49-0.72				
LL24-0.4	0.4	32.5	31.7-33.1	0.35	0.32-0.39	47.6	46.8-48.7	0.19	0.17-0.28
LL24-0.5	0.5	19.0	18.6-19.3	0.38	0.36-0.42	32.8	32.5-33.1	0.19	0.19-0.23
LL24-0.6	0.6	11.8	11.6-12.0	0.46	0.45-0.49	23.2	22.7-23.8	(0.29)	(0.26-0.33)
LL24-0.7	0.7	7.7	7.6-8.0	(0.64)	(0.63-0.69)	17.1	16.7-17.5	(0.43)	(0.40-0.46)
MA24-0.5	0.5	20.2	19.8-20.7	0.48	0.43-0.51	34.4	33.9-35.2	0.27	0.26-0.32
CH24-0.5	0.5	21.4	20.7-22.1	0.56	0.51-0.60	34.6	33.9-35.1	0.29	0.26-0.32
LLF24-0.5	0.5	26.0	25.5-26.5	0.87	0.84-0.89	36.8	36.0-38.0	0.42	0.36-0.48
LLC24-0.5	0.5	16.4	15.8-17.2	0.21	0.15-0.27	31.8	31.3-32.2	0.15	0.13-0.17
			7 days 5 °C				**7 days 20 °C**		
LL12-0.5	0.5	49.0	47.7-49.7	0.57	0.44-0.62	50.9	50.4-51.7	0.17	
LLF12-0.5	0.5	54.4	53.3-55.6	1.08	0.96-1.21				
LLC12-0.5	0.5	46.3	45.1-47.5	0.33	0.20-0.43				
MA12-0.5	0.5	48.6	47.4-50.0	0.52	0.41-0.65				
CH12-0.5	0.5	50.8	50.3-51.5	0.75	0.70-0.79				
LL24-0.4	0.4	58.5	57.2-59.6	0.36	0.33-0.44	58.6	57.9-60.1	0.14	0.12-0.25
LL24-0.5	0.5	40.5	39.8-40.9	0.39	0.36-0.41	42.3	41.5-43.1	0.17	0.15-0.21
LL24-0.6	0.6	28.2	27.7-28.7	0.48	0.47-0.52	31.5	30.7-32.0	(0.26)	(0.22-0.30)
LL24-0.7	0.7	19.9	19.5-20.5	(0.63)	(0.61-0.66)	22.8	22.1-23.5	(0.30)	(0.26-0.35)
MA24-0.5	0.5	40.4	39.6-41.1	0.39	0.34-0.42	43.5	42.8-43.8	0.23	0.21-0.26
CH24-0.5	0.5	43.9	42.1-45.1	0.55	0.48-0.61	43.2	43.0-44.0	0.21	0.19-0.24
LLF24-0.5	0.5	44.1	43.4-44.9	0.57	0.54-0.60	44.5	43.3-45.9	0.27	0.23-0.34
LLC24-0.5	0.5	37.9	37.1-38.7	0.28	0.25-0.32	42.4	41.6-43.2	0.19	0.15-0.22
			28 days 5 °C				**28 days 20 °C**		
LL12-0.5	0.5	62.2	60.5-64.4	0.50		58.5	57.4-59.4	0.36	0.25-0.43
LL24-0.5	0.5	52.3	51.4-52.7	0.29		49.7	48.7-50.6	0.27	0.21-0.31

1) Values in brackets are uncertain because they are calculated for low strength levels, below the strength range of experimental values for the Portland cement mortars; see Figures 1 to 3.

Figures 1 and 2 show the early-age strength of the limestone mixtures LL24-0.4 to LL24-0.7 and OPC-0.4 to OPC-0.7 mixtures. There seems to be a fairly linear relationship between the compressive strength (f_c) and the inverse of the water-binder ratio for both cement and blended mortars. This indicates that a linear equation as proposed by Bolomey, Eq. (1), could be used for calculations, but with different empirical parameters *a* and *b* to be determined for each specific age and temperature.

$$f_c = a\left(\frac{1}{W/B} - b\right) \tag{1}$$

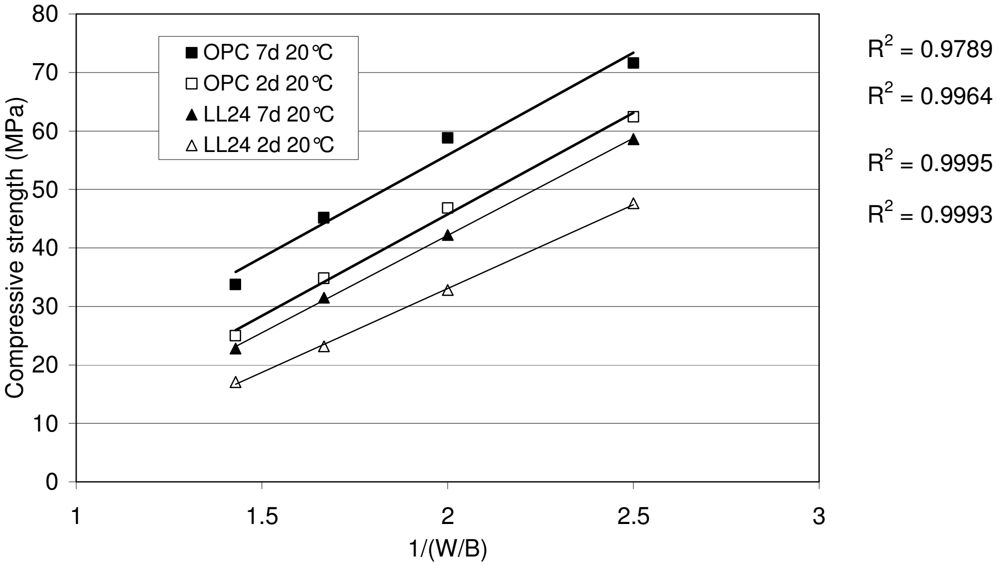

Figure 1 – Mean compressive strength at 20 °C (dots) and relationship versus 1/(W/B) (lines).

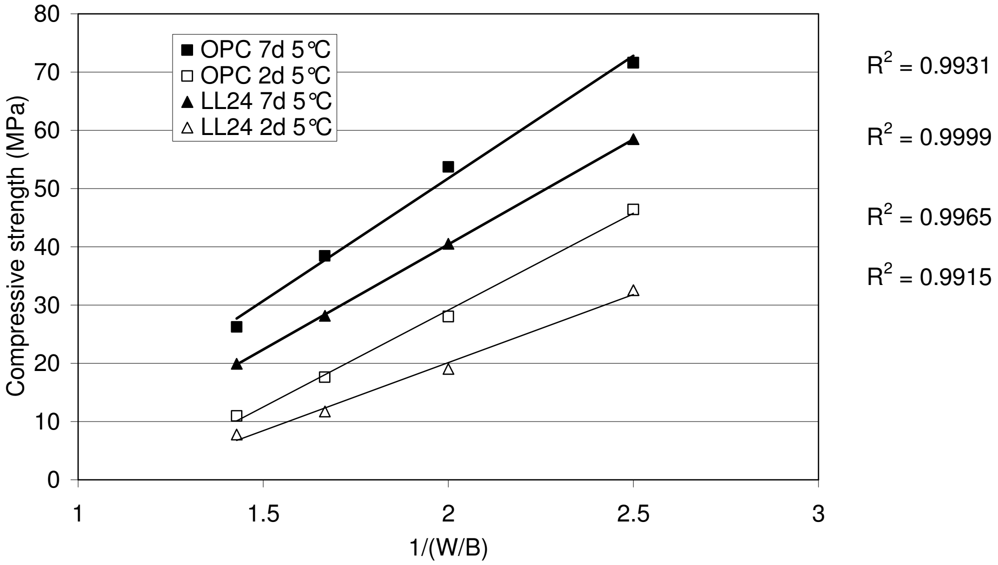

Figure 2 – Mean compressive strength at 5 °C (dots) and relationship versus 1/(W/B) (lines).

The calculation of the *k*-value for an addition is made by finding a replacement for the water/binder ratio – an equivalent water-cement ratio $(W/C)_{eq}$ – that the mixture with addition should have in order to obtain the same compressive strength as the mixture without addition.

The equivalent water-cement ratio is defined as:

$$(W/C)_{eq} = \frac{W}{C + kR} \tag{2}$$

where: W = water content, by mass; R = addition content, by mass
C = cement content, by mass; *k* = efficiency coefficient

From Eq. (2) it should be noted that the calculation of the *k*-value is sensitive to small variations of the $(W/C)_{eq}$, in particular when the amount of addition is small; see [12].

$(W/C)_{eq}$ can be calculated by using empirical relationships between strength and *W/C* for OPC mixtures, as e.g. trend lines according to Eq. (1), or they can be found out graphically from the real experimental data graphs.

In the present attempt to evaluate the efficiency of limestone filler the graphical alternative was used. The reason for this was primarily that the distribution of the results for OPC mortars deviated slightly from a straight trend line, especially at 7 days and 20 °C. See the correlation coefficients in Fig.1.

The *k*-values given in Table 6 were calculated by using Eq. (2) and the $(W/C)_{eq}$ determined from the experimental data graphs shown in Figure 3. A graphical extension, defined by the slope between *W/C* 0.6 and 0.7, was added for the lower strength values.

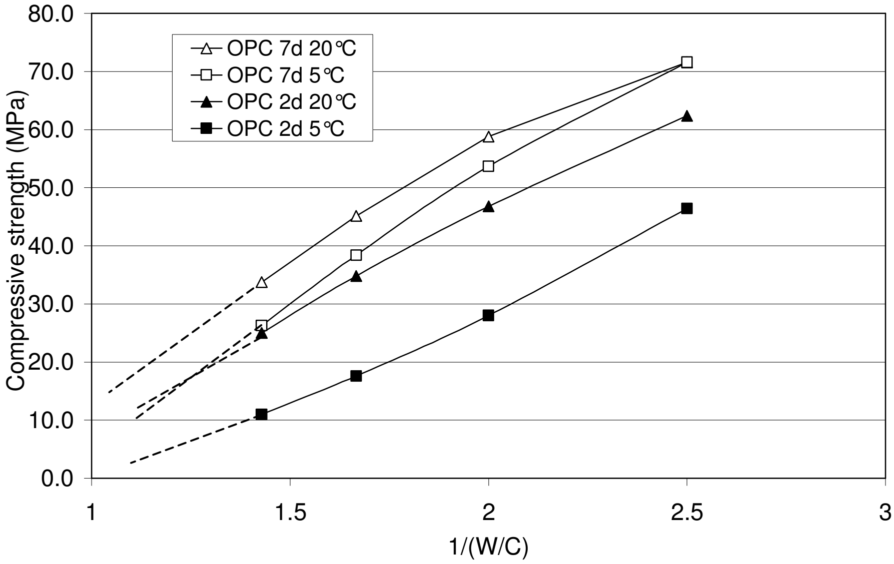

Figure 3 – The relationships between compressive strength and 1/(W/C) for cement mortars, used for the graphical estimation of $(W/C)_{eq}$ for mortars containing limestone filler.

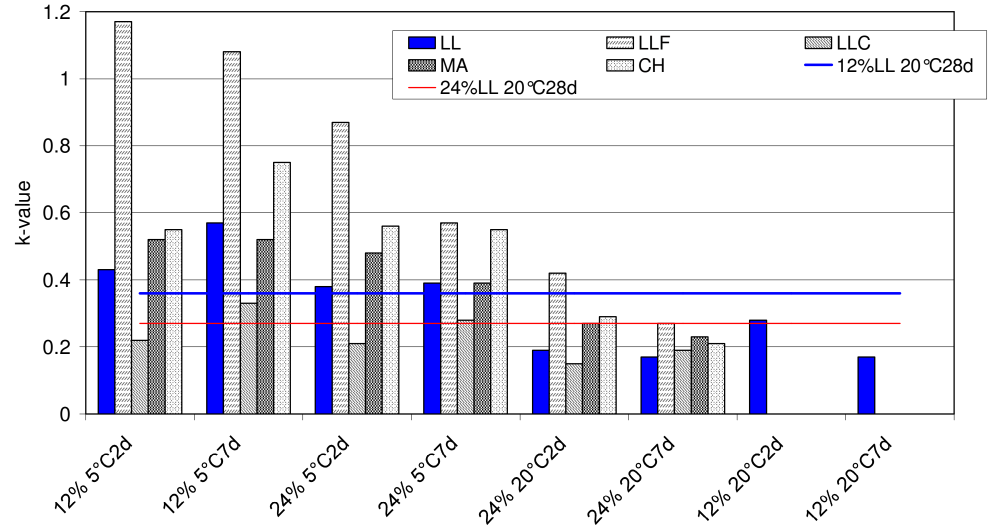

Figure 4 – k-values for different qualities of limestone in mortars with W/B 0.5

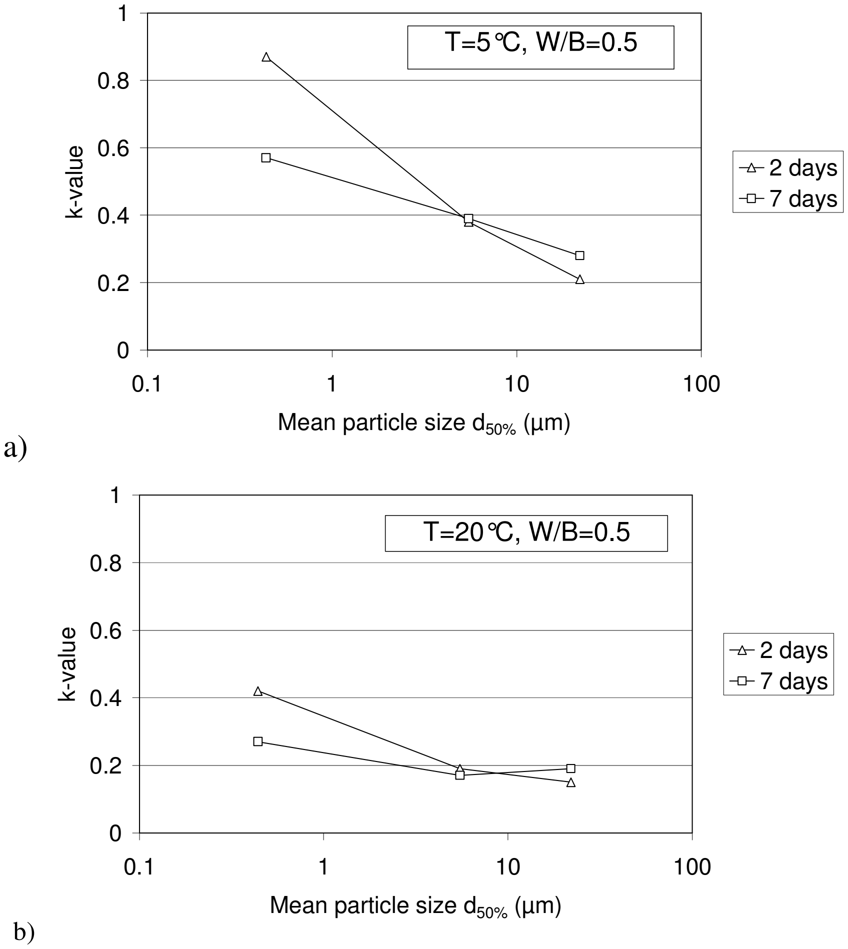

Figure 5 – Influence of the fineness of the filler on the coefficient of efficiency at early age at 5 °C (a) and at 20 °C (b). Values for mortar with W/B 0.5 and 24% limestone filler type LL.

A general indication shown by the results in Table 6 is that efficiency coefficients for strength can be applied to limestone. However, the values are rather low, with the exception of the very fine limestone fraction LLF. An overall comparison of *k*-values for limestone is shown in Figure 4.

The *k*-values as a function of the mean particle size of the filler ($d_{50\%}$), in mortars with 24% limestone filler, are shown in Figure 5. The fineness of the filler seems to be a significant parameter regarding the efficiency coefficient, especially at low temperature. The finest limestone filler in this investigation has a *k*-value of almost 1 at 5 °C and early age, but it decreases to 0.2-0.3 for the coarse filler fraction. The fineness of the filler has an influence on the compressive strength also at 20 °C, at least for two days old mortar, but less significant as at low temperature.

A comparison between *k*-values for limestone fillers produced with different types of carbonated rock, CH, LL and MA, are presented in Figure 6 below.

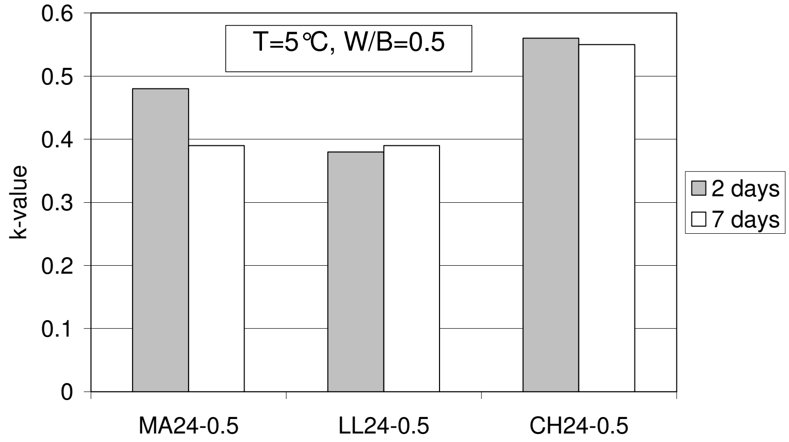

a)

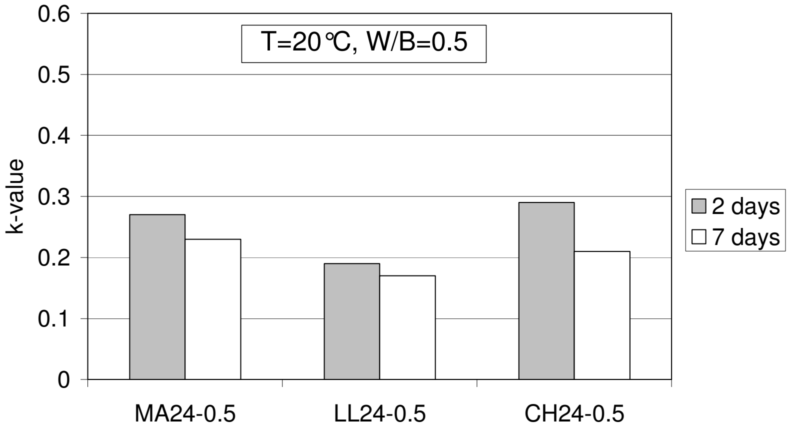

b)

Figure 6 – Influence of the type of the carbonated on the coefficient of efficiency of the limestone filler. Values at 5 °C (a) and at 20 °C (b) for mortar with 24% limestone and W/B 0.5.

According to the results, there does not seem to be any significant influence of the type of carbonated rock used on the *k*-value of the filler. This can be observed at both 5 °C and 20 °C, for 2 days as well as for 7 days old mortars. The small differences between these three types of carbonated rocks may be due to some differences in finesses. The mean particle size was 2.3, 5.5 and 7.0 respectively for CH, LL and MA. Probably the value for CH24 in Figure 6 would have been slightly lower if its fineness would have been the same as for LL24.

Figure 7 shows a comparison between the *k*-values for limestone filler (LL) and the *k*-values for two qualities of reactive additions – silica fume (SF) and ground granulated blastfurnace slag (SG) – as function of age, at 5 °C and 20 °C.

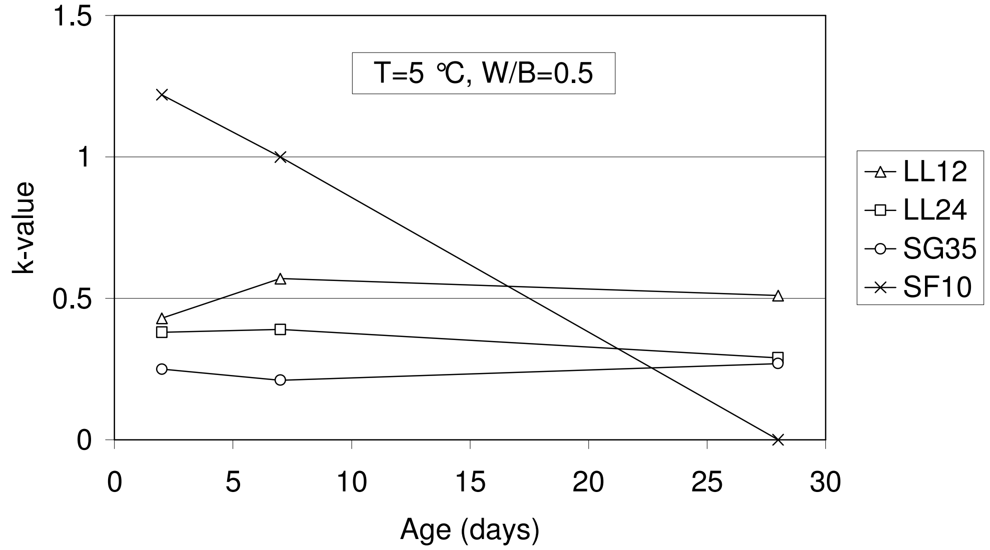

a)

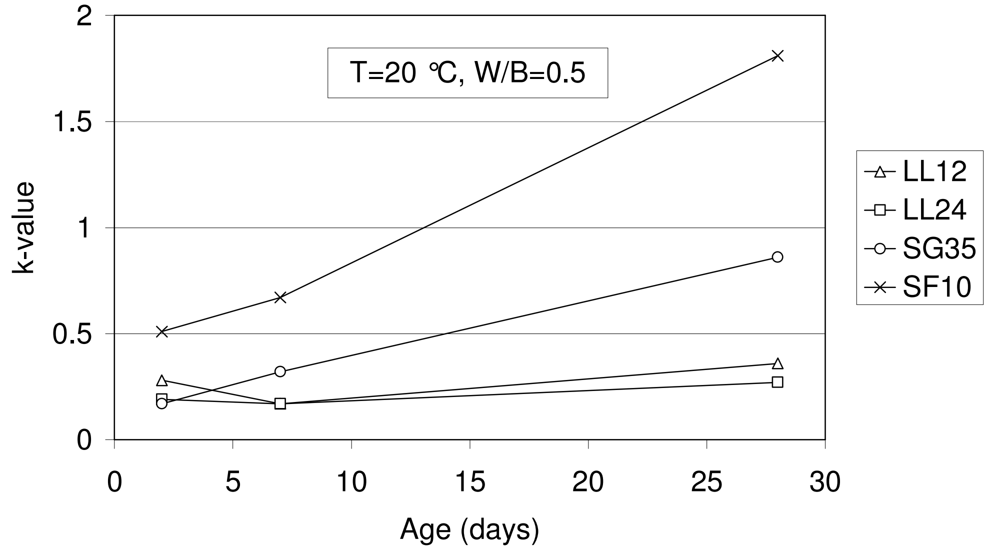

b)

Figure 7 – Coefficients of efficiency as a function of age, for limestone (LL), silica fume (SF) and ground granulated blastfurnace slag (SG), at 5 °C (a) and 20 °C (b). Results for mortars with W/B 0.5 and 12% or 24% limestone, 10% silica fume or 35% slag as part of the binder.

The results for slag and silica fume were determined in a complementary part of the investigation presented in this paper. The tests were performed exactly as the tests presented in this paper, but with the use of silica fume or ground granulated blastfurnace slag instead of limestone filler. Details about the studies on SF and SG can be found in [13].

Considering the *k*-value of silica fume 1 or 2 according to EN 206-1 [9] and the *k*-value for slag 0.6 according to the Swedish Standard SS 13 70 03 [14], this investigation found that the 28-day values for slag and silica fume correspond well with the standard values, if the curing temperature is 20 °C. However, at earlier ages the *k*-values for these two additions are considerably lower, at both 5 °C and 20 °C.

At early age limestone filler and slag have comparable coefficients of efficiency in mortars cured at 20 °C, but in mortars cured at 5 °C limestone shows higher efficiency than slag: *k*-values are about 0.4 or higher, compared to about 0.2 for slag. On the other hand neither limestone nor slag reach the efficiency of silica fume at early age, regardless the curing temperature.

The comparison in Figure 7 shows that if a low temperature can lead to higher early-age coefficient of efficiency compared to 20 °C, not least for limestone, the development up to 28 days is very different at different temperatures. At 20 °C slag shows a significant increase in efficiency, reaching a *k*-value of about 0.8 at 28 days, while limestone only reaches values of about 0.3. At 5 °C on the other hand the efficiency of both slag and limestone seems to remain more or less unchanged after 7 days, though at a higher level for limestone compared with slag. These observations refer to the addition qualities used in this study, in mortars with W/B 0.5.

Limestone compared with silica fume shows significant differences. The early-age *k*-values for silica fume are higher than for limestone, much higher at 5 °C compared to 20 °C. Later at 28 days, where the *k*-values for limestone show small changes compared to early-age values, silica fume shows considerably increased values at 20 °C and an opposite development at 5 °C. After 7 days the efficiency of silica fume in mortars cured at 5 °C decreases rapidly, showing zero efficiency for compressive strength at 28 days.

Similar observations, that a low temperature may with time reduce the strength-increasing effect of silica fume, have been mentioned in other studies [15, 16]. This performance is however not fully explained or understood.

4 CONCLUSIONS

Based on the results found in this investigation, the following conclusions can be drawn:

- All the types of limestone filler used in this investigation showed a positive effect, compared with what could be expected from a completely inert material, on the mortar compression strength. This effect can be quantified by the coefficient of efficiency or *k*-value. For the limestone fillers the *k*-value was normally in the range of 0.2-0.5, with the highest values when cured at low temperature. For a very fine-grained limestone filler, however, a *k*-value of about 1 was found for young mortar cured at 5 °C.

- The *k*-value is strongly influenced by the fineness of the limestone filler, especially at low temperatures and young age.

- The type of carbonated rock used for producing the limestone filler, with regard to the metamorphose level, does not seem to significantly influence the *k*-value. This is relevant at least for the three types of carbonated rock used in this investigation.

- Traditional type II additions such as silica fume and ground granulated blast furnace slag show, as expected, higher *k*-values than limestone filler at 20 °C and 28 days. At young ages (below 7 days), however, the *k*-value of the limestone fillers used in this study are comparable or even higher than the corresponding values for slag. These limestone fillers show also lower *k*-values than silica fume at early ages, but after a longer curing time at low temperature limestone maintains its efficiency for compressive strength while the efficiency of silica fume is decreasing.

REFERENCES

1. EN 197-1, Cement–Part 1: Composition, specifications and conformity criteria for common cements. *European standard*, 2000.
2. Goldman, A., Bentur, A.,“The influence of microfillers on enhancement of concrete strength”. *Cem. Conc. Res.* **23** (1993) pp. 962-972.
3. Taylor, H. F. W., Cement Chemistry, second edition. *Thomas Telford Publishing*, 1997.
4. Bonavetti, V. Donza, H., Menédez, G. Cabrera, O., Irassar, E. F., “Limestone filler in cement in low w/c concrete: A rational use of energy”. *Cem. Conc. Res.* **33** (2003) pp. 865-871
5. Tsivilis, S., Chaniotakis, E., Kakali, G., Batis,G., ”An analysis of the properties of Portland limestone cements and concrete”. *Cem. Conc. Comp.* **24** (2002) pp. 371-378.
6. Péra, J., Husson, S., Guilhot, B., ”Influence of finely ground limestone on cement hydration”. Cem. Conc. Comp. **21** (1999) pp. 99-105.
7. Bonavetti, V. L., Rahhal, V. F., Irassar, E. F., “Studies on the carboaluminate formation in limestone filler-blended cements”. *Cem. Conc. Res.* **31** (2001) pp. 853-859.
8. Kakali, G., Tsivilis, S., Aggeli, E., Bati, M., ”Hydration products of C_3A, C_3S and Portland cement in the presence of $CaCO_3$”. *Cem. Conc. Res.* **30** (2000) pp. 1073-1077.
9. EN 206-1, Concrete–Part 1: Specification, performance, production and conformity. *European standard*, 2000.
10. EN 196-1, Methods of testing cement–Part 1: Determination of strength. *European standard*, 1994.
11. Moosberg-Bustnes, H., “Fine particulate by-products from mineral as metallurgical industries as filler in cement-based materials”. *Ph.D Thesis*, Luleå University of Technology, 2003.
12. Petersson, P-E., “Determination of coefficients of activity for mineral additions in mortar”. Report SP-RAPP 1983:11, Swedish National Testing and research Institute, Borås, 1983 (in Swedish).
13. Lundgren, M., “ Early-age strength development at low temperatures in concrete with mineral additions–efficiency coefficients for slag and silica fume”. Accepted for publication in the proceedings of the Eighth CANMET/ACI International Conference on Fly Ash, Silica Fume, Slag and Natural Pozzolans in Concrete, Las Vegas, May 24-29 2004.
14. SS 13 70 03, Concrete – Application of EN 206-1 in Sweden. Swedish standard.
15. Marzouk, H. M., Hussein, A., “Properties of high-strength concrete at low temperature”. *ACI Mat. Journ.* March-April 1990, pp.167-171.
16. Chakraborty, K. A., Dutta, S. C., “ Study on silica fume modified mortar with various Indian cements cured at different temperatures”. *Building and Environment* **36** (2000) pp. 375-382.

Applicability of FRP confinement to strengthen concrete columns.

Laura De Lorenzis
Department of Innovation Engineering
University of Lecce
I-73100 Lecce, Italy
Laura.delorenzis@unile.it

Ralejs Tepfers
Concrete Structures
Department of Structural Engineering and Mechanics
Chalmers University of Technology
SE-412 96 Gothenburg Sweden
ralejs.tepfers@sem.chalmers.se

ABSTRACT

The bearing capacity of concrete cylinders in compression can be increased manifold by confining them with FRP sheets or tubes. The stress-strain relationship for an FRP-confined cylinder is approximately bi-linear. The first branch may be simplified as linear with a slope E_1 equal to the secant modulus of the unconfined concrete in compression. At the level of the concrete unconfined strength, a transition zone follows after which the tangent stiffness stabilizes at a constant value, E_2, until reaching the ultimate strength. When transferring these data to the design of concrete columns, the stability problem must be accounted for. The buckling load is determined by the moment of inertia and the elastic modulus of the column. The moment of inertia is not increased by unidirectional tangential wraps around the column and the elastic modulus of the column decreases above failure load of unwrapped column. Consequently, the increase in strength due to wrapping cannot be utilized unless the slenderness ratio is lower than a limiting value, function of the confinement parameters and of the unconfined strength. Furthermore, when the confined strength can be used in design, it is necessary to ensure that the wrapping material cannot be damaged during the lifetime of column. Such damage can result, for instance, from the hit of a vehicle or from fire. In such a case the column will fail because the confined concrete within the wrap/tube in the second branch of the stress-strain curve is degraded. Therefore the load on confined column should be limited by long term sustained load on unconfined column.

Keywords: FRP, concrete, confinement, compressive strength, buckling.

1 INTRODUCTION

Numerous investigations have shown that the bearing capacity of concrete cylinders in compression can be increased manifold by confining them with FRP sheets or tubes. Research efforts have been mainly directed towards quantification of the strength and ductility increase on standard size cylindrical specimens (with 150-mm diameter and 300-mm height).

Performed axial compression tests with FRP-confined concrete cylinders have in general stress-strain relations as shown in Figure 1, Rousakis [4]. It can be seen that the axial stress-strain response is distinctly bilinear. The first branch is very close to the ascending portion of the unconfined concrete stress-strain relationship. The latter may be simplified as linear with a slope E_1 equal to the secant modulus of concrete in compression. At the level of the concrete unconfined strength, *f'*, a transition zone follows after which the tangent stiffness stabilizes at a constant value, E_2, until reaching the ultimate strength, *f'*. Thus, a simplified stress-strain response of FRP-confined concrete can be as shown in Figure 2. The peak point coincides with the ultimate point and they both correspond to tensile rupture of the FRP confining device. Increased confinement stiffness (that is, increased number of wrapping layers and fiber modulus of elasticity) increases the value of the second slope, E_2.

The failure compressive load for wrapped concrete cylinder can be several times that of unwrapped cylinder. The question is if and when this strength increase can be exploited in concrete columns when the stability problem is accounted for.

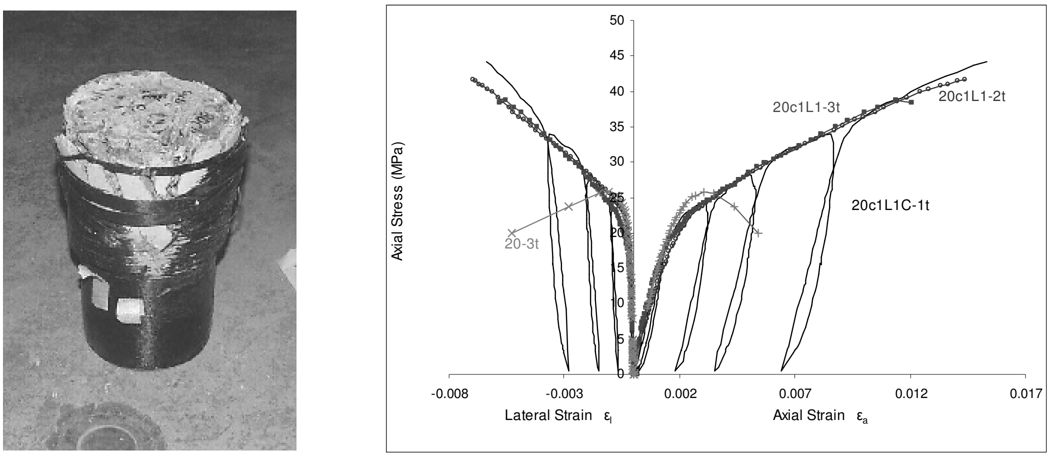

Figure 1. Compressive test of one layer carbon fiber sheet confined concrete cylinder. Stress – strain behavior of specimens from 25.2 MPa concrete, confined with 3 layers of CFRP sheet under monotonic and cyclic axial load. Rousakis [4].

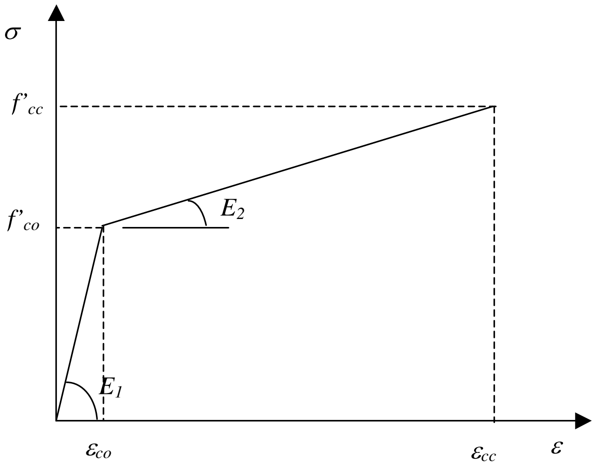

Figure 2. Simplified axial stress-strain relationship of confined concrete cylinders

Mirmiran et al [3] tested columns made of FRP tubes filled with concrete of 22.4-MPa compressive strength. Columns with different slenderness were tested and their buckling load was experimentally determined. From a theoretical standpoint, the authors calculated the Euler buckling load using the tangent stiffness approach. As they used for confined concrete the non-linear stress-strain relationship proposed by Saaman et al. [5], they were forced to compute the buckling load with a numerical step-by-step procedure. By using the simplified relationship in Figure 2, a closed-form solution for limiting slenderness ratios and buckling load can be easily obtained, while introducing no appreciable error in results. This will be done as follows.

2 ANALYSIS OF BUCKLING OF FRP-CONFINED COLUMNS

2.1 Euler buckling load and limiting slenderness ratios

The Euler buckling load of a column is given by:

$$P_{cr} = \frac{\pi^2 EI}{(kl)^2} \tag{1}$$

where E is the modulus of elasticity of the constituent material; I is the moment of inertia of the cross-section; l the length of the column; k a factor depending on the restraint conditions of the column at both ends. Diving (1) by the cross-sectional area, A, the Euler buckling stress is obtained as:

$$\sigma_{cr} = \frac{\pi^2 E}{\lambda^2} \tag{2}$$

where:

$$\lambda = \frac{kl}{r} \tag{3}$$

is the slenderness ratio of the column. In equation (3), r is the radius of gyration:

$$r = \sqrt{\frac{I}{A}} \tag{4}$$

When an FRP-confined column is considered, moment of inertia and cross-sectional area to introduce in the formulae should be gross values, including the contribution of the FRP confining device. However, the thickness of the FRP is in practical cases very small; furthermore, the fiber orientation is typically as close as possible to the circumferential direction to maximize the confinement action and the elastic modulus of the laminate transverse to the fibers is very close to that of the resin matrix (i.e., very small). This implies that calculating I and A as those pertaining to the concrete only does not lead to appreciable error.

More importantly, equation (2) is valid for a linearly elastic material with modulus of elasticity E, and needs to be suitably modified for a stress-strain curve as that of Figure 1. For this purpose, the approach suggested by Fr. Engesser already in 1889 and then validated by Shanley [6] can be adopted. Such approach suggests substituting E in equation (2) with the tangent elastic modulus of the material, equal to the local slope E_t of the stress-strain curve:

$$\sigma_{cr} = \frac{\pi^2 E_t}{\lambda^2} \tag{5}$$

As E_t must be evaluated on the stress-strain curve for a value of stress equal to σ_{cr}, equation (5) gives σ_{cr} in implicit form. For the stress-strain curve in Figure 2, it is:

$$\begin{cases} E_t = E_1 & \text{if} \quad \sigma < f'_{co} \quad (\text{or } \varepsilon < \varepsilon_{co}) \\ E_t = E_2 & \text{if} \quad f'_{co} < \sigma < f'_{cc} \quad (\text{or } \varepsilon_{co} < \varepsilon < \varepsilon_{cc}) \end{cases} \tag{6}$$

Therefore:

$$\begin{cases} \sigma_{cr} = \dfrac{\pi^2 E_1}{\lambda^2} \quad \text{if} \quad \sigma_{\mathrm{cr}} < f'_{co}, \quad \text{i.e. if } \lambda > \lambda_{l1} = \pi\sqrt{\dfrac{E_1}{f'_{co}}} & \text{(7a)} \\ \sigma_{cr} = f'_{co} \quad \text{if} \quad \lambda_{l2} < \lambda < \lambda_{l1} & \text{(7b)} \\ \sigma_{cr} = \dfrac{\pi^2 E_2}{\lambda^2} \quad \text{if} \quad \sigma_{\mathrm{cr}} > f'_{co}, \quad \text{i.e. if } \lambda < \lambda_{l2} = \pi\sqrt{\dfrac{E_2}{f'_{co}}} & \text{(7c)} \end{cases}$$

The graphical solution of equation (5) is illustrated in Figure 3. Both members of (5) are known functions of the axial strain ε:

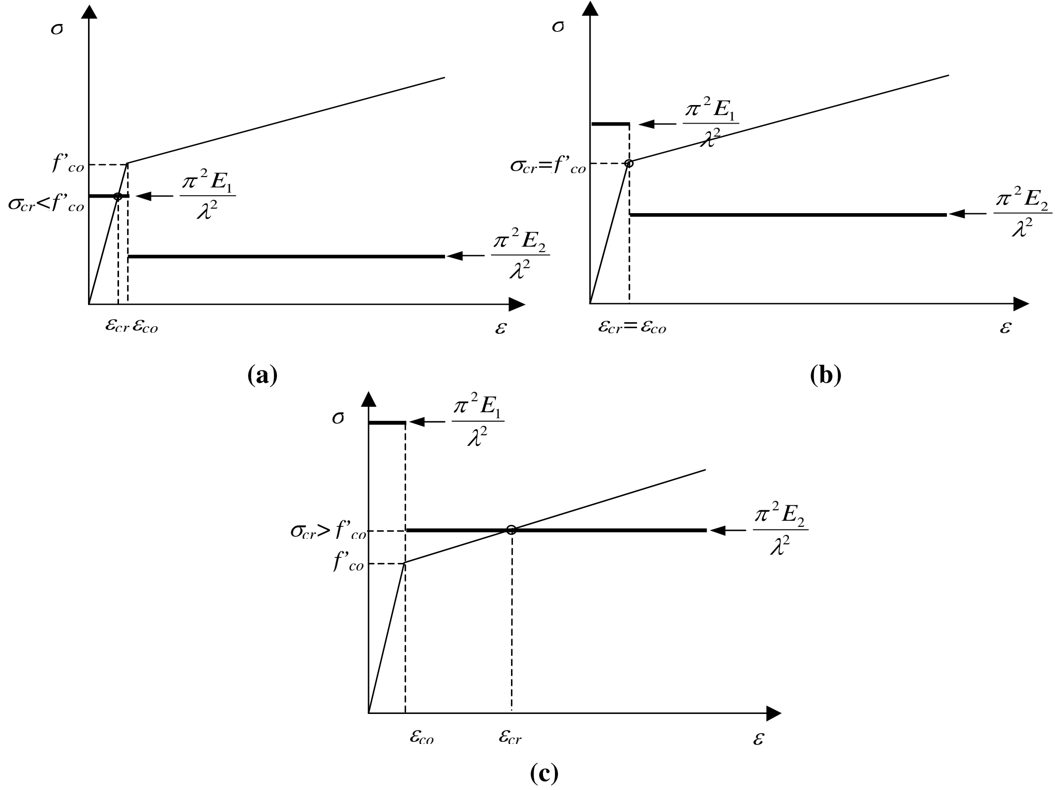

(a) **(b)**

(c)

Figure 3. Euler buckling stress for $\lambda > \lambda_{l1}$ *(a),* $\lambda_{l2} < \lambda < \lambda_{l1}$ *(b) and* $\lambda < \lambda_{l2}$ *(c)*

$$\sigma = \sigma(\varepsilon) \tag{8a}$$

$$\frac{\pi^2 E_t}{\lambda^2} = \frac{\pi^2 E_t(\varepsilon)}{\lambda^2} = \frac{\pi^2}{\lambda^2}\frac{d\sigma(\varepsilon)}{d\varepsilon} \tag{8b}$$

The intersection point between (8a) and (8b) defines the critical strain ε_{cr} to which σ_{cr} corresponds.

Summarizing, for $\lambda > \lambda_{l1}$ the column is so slender that instability occurs for a value of axial stress lower than the unconfined concrete strength, f'. For $\lambda_{l2} < \lambda < \lambda_{l1}$, the buckling stress coincides with the unconfined concrete strength. In both ranges of slenderness, the contribution of the FRP confinement to the concrete strength is not exploited at all. For $\lambda < \lambda_{l2}$, the buckling stress is higher than the unconfined concrete strength and the enhancement in strength due to FRP confinement can thus be exploited. In particular, defining:

$$\lambda_{l3} = \pi\sqrt{\frac{E_2}{f'_{cc}}} \tag{9}$$

it is also:

$$\begin{cases} f'_{co} < \sigma_{cr} = \dfrac{\pi^2 E_2}{\lambda^2} \leq f_{cc} & \text{if} \quad \lambda_{l3} \leq \lambda < \lambda_{l2} \\ \sigma_{cr} = \dfrac{\pi^2 E_2}{\lambda^2} \geq f_{cc} & \text{if} \quad \lambda \leq \lambda_{l3} \end{cases} \tag{10}$$

For $\lambda_{l3} < \lambda < \lambda_{l2}$, buckling is still the governing mode of failure. Only when $\lambda < \lambda_{l3}$ the column fails in compression before buckling occurs and the FRP confinement is fully effective. In Figure 4 the ratio of the buckling load to the ultimate compressive load of the column is plotted vs. the slenderness ratio.

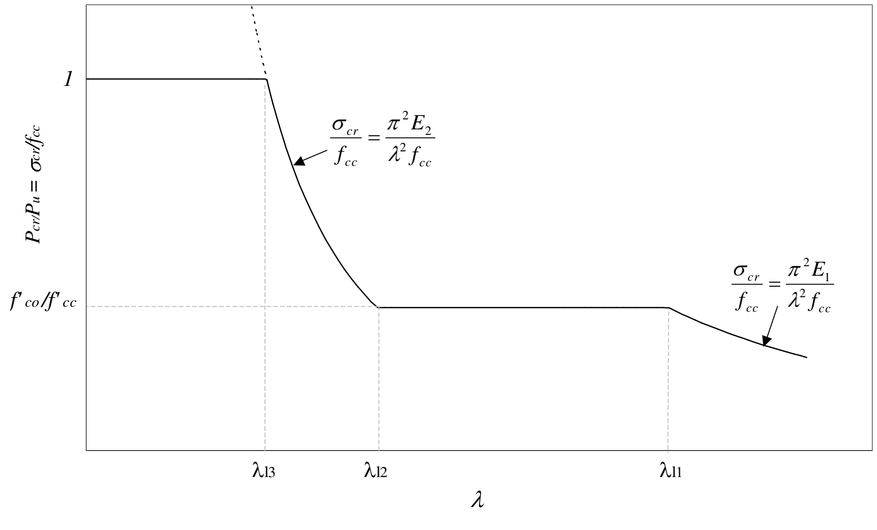

Figure 4. Combined normalized buckling load as function of slenderness.

2.2 Computation of the limiting slenderness ratios

The values of the limiting slenderness ratios λ_{l1}, λ_{l2} and λ_{l3} can be computed as follows.

The secant modulus of concrete in compression, E_1, can be computed according to Ahmad and Shah [1]:

$$E_1 = 3950\sqrt{f'_{co}} \tag{11}$$

from which:

$$\lambda_{l1} = \pi \sqrt{\frac{E_1}{f'_{co}}} \cong \frac{197.45}{\sqrt[4]{f'_{co}}} \tag{12}$$

For the computation of λ_{l2}, the second slope E_2 of FRP-confined concrete can be evaluated by means of several models available in the literature (De Lorenzis, [2]). For instance, the model by Saaman et al. [5] expresses E_2 as function of the stiffness of the confining jacket and, to a lesser extent, of the unconfined concrete strength:

$$E_2 = 245.61 f'^{\,0.2}_{co} + 0.6728 E_l \tag{13}$$

where:

$$E_l = \frac{2 E_f nt}{D} \tag{14}$$

sometimes called confinement modulus or lateral modulus, is a measure of the stiffness of the confining device. In (14) E_f is the FRP Young's modulus in the hoop direction, nt is the thickness of the FRP and D the column diameter.

Finally, calculation of λ_{l3} requires also an expression for the confined concrete strength f'. According to the model by Saaman et al.[5]:

$$f'_{cc} = f'_{co} + 6.0 p_u^{0.7} \tag{15}$$

where:

$$p_u = \frac{2 f_f nt}{D} \tag{16}$$

is the maximum value of the confinement pressure that the FRP can exert before rupturing in tension. In (16) f_f is the FRP tensile strength in the hoop direction.

From what shown previously it is evident that, in order for the confinement effect to be fully exploited, the slenderness ratio must be lower than or equal to λ_{l3} given by (9). The latter may be rewritten as follows:

$$\lambda_{l3} = \pi \sqrt{\frac{E_2(E_l, f'_{co})}{f'_{cc}(p_u, f'_{co})}} \tag{17}$$

From (17) it is evident that λ_{l3} increases as the confinement *stiffness* increases (because this raises the second slope of the stress-strain curve) and decreases as the maximum confinement *pressure* increases, because this leads to a higher compressive strength. Therefore:

- for a given tensile strength and Young's modulus of the FRP, λ_{l3} decreases as the number and thickness of FRP plies decreases, that is, as the *D/nt* ratio increases;
- for a given *D/nt* ratio, λ_{l3} increases with the elastic modulus of the FRP and decreases with its tensile strength;
- for given *D/nt* ratio and FRP mechanical properties, λ_{l3} decreases as the unconfined concrete strength increases.

The variation of λ_{l3} with the FRP and concrete parameters is illustrated in Figure 5, where the *D/nt* ratio is varied between 25 and 100, the concrete unconfined strength between 20 and 80 MPa and three combinations of FRP mechanical properties (tensile strength f_f and Young's modulus E_f) are chosen.

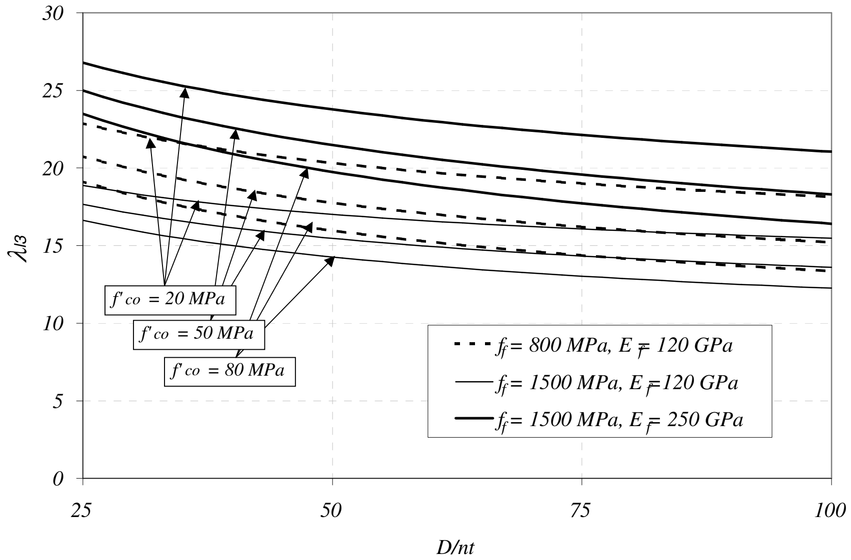

Figure 5. Variation of λ_{l3} with the FRP and concrete parameters

Strength increase by FRP confinement is most effective for columns with circular section. For square columns confinement is effective only in regions of corners and these should be rounded for better effect. For rectangular columns, as the second slope is typically very low due to the low effectively-confined portion of the cross-section, the values of λ_{l2} and λ_{l3} are very close to each other and very low.

3 DISCUSSION ABOUT SAFETY

3.1 Accidental damage of columns

To be able to use the wrapping strengthening effect of column it is necessary to ensure that the confining FRP cannot easily be damaged during the lifetime of column. The column might be hit by a vehicle and the wraps damaged or just locally scraped off. As the concrete within the confining wraps in the second part of the stress-strain curve is degraded, it will blow out where the damage is and a collapse of column follow. In case of fire, when the resin of wrap along the whole column is affected, the risk of collapse is increased considerably. Concrete cover with a thickness say 30 mm may be used for protection. This cover will increase the loaded column area and moment of inertia considerably. If the diameter of the wrapped column is 150 mm, the column with cover will have diameter 210 mm. The area will increase with factor 1.96 and the moment of inertia with factor 3.84 increasing the buckling load with the same amount. Up to ultimate unwrapped concrete load the covers will be active in load taking. Then the covers will fall off and the deformations of the column will increase considerably. It is doubtful if the second part of the stress-strain curve with modulus E_2 for the column can be used. For safety reason, if the wraps are accidentally damaged, a wrapped column should not be designed for more than 75% of the ultimate short term un-wrapped column load, which is the long term sustained load.

3.2 Performance of column under cycling load

In Figure 1 it is seen that at cycling of load the stress-strain curves have about the same inclination as the first part of the curve with modulus E_1. A certain recovery of expanded and degraded concrete within the wraps can be observed at unloading. Probably the unloading slope of the stress-strain curve will not influence the buckling load. At column buckling the side, where compression increases, wraps will be stressed more and less at opposite side, where compression is reduced. The action of wraps at buckling is a field for investigation. Further, if a wrapped concrete column is prevented to buckle and is loaded in compression almost up to failure and then unloaded, the tangent modulus for this column, now loaded without side support, is about the same as for the first part of curve with modulus E_1. Will this column now have higher buckling load and can this procedure be used for improving properties of column? Is this a way of introducing prestress in the confining filaments?

4 CONCLUSIONS

When performing tests on FRP-confined concrete cylinders, researchers have paid much interest to the considerable increase in strength. However, most columns have to be designed for stability and confinement of columns with unidirectional composites with fibers along the hoop direction does not improve the buckling resistance parameters. The favor of increased confined concrete strength in many cases cannot be used. Wraps can easily be damaged. The load on column should not exceed the long term sustained load on unwrapped column.

ACKNOWLEDGEMENTS

The investigation was sponsored by European Commission - TMR - Network, ConFibreCrete "Research leading to the Development of Design Guidelines for the use of FRP in Concrete Structures” and Chalmers University of Technology and Åke and Greta Lissheds Foundation, SEB Bank, 106 40 Stockholm.

REFERENCES

1 Ahmad and Shah S. (1982). “Stress-strain curves of concrete confined by spiral reinforcement”, *Journal of the American Concrete Institute*, v. 79, No. 6, pp. 484-490.

2 De Lorenzis L. (2001). “A Comparative Study of Models on Confinement of Concrete Cylinders with FRP Composites”. Chalmers University of Technology, Division of Building Technology, Work No 46. Publication 01:4. Göteborg, 2001-06-30. p.73. http://www.bm.chalmers.se/bm9707/Division/Dindex.htm

3 Mirmiran A., Shahawy M., Beitleman T. (2001). “Slenderness Limit for Hybrid FRP-Concrete Columns”, ASCE Journal of Composites for Construction, Vol. 5, No, 1, February 2001. pp. 26-34.

4 Rousakis T. (2001). “Experimental Investigation of Concrete Cylinders Confined by Carbon FRP Sheets, under Monotonic and cyclic Axial Compressive Load”. Chalmers University of Technology, Division of Building Technology, Ongoing investigation, Work No 44. Göteborg, 2001-3-08. p. 87.

5 Samaan M., Mirmiram A., Shahawy M. (1998). “Model of Concrete Confined by Fiber Composites”. ASCE Journal of Structural Engineering, V. 124, No 9, September 1998. pp. 1025-1031.

6 F.R. Shanley (1947), “Inelastic column theory”, Journal of Aeronautical Sciences Vol. 14, No. 5, pp. 261-267.

Behavior of concrete confined by high E-modulus carbon FRP sheets, subjected to monotonic and cyclic axial compressive load

Theodoros Rousakis
Laboratory of Reinforced Concrete, Engineering Faculty
Demokritus University of Thrace
Xanthi GR-67100 Greece
trousak@civil.duth.gr

Ralejs Tepfers
Department of Structural Engineering and Mechanics
Concrete Structures
Chalmers University of Technology
SE-412 96 Gothenburg Sweden
ralejs.tepfers@ste.chalmers.se

Abstract

A systematic investigation is performed on the mechanical behavior of concrete cylinders (with compressive cylinder strength 25.2 MPa and 51.8 MPa), confined by high E-modulus carbon fiber sheet (377 GPa). The concrete cylinders were wrapped with 1, 2, 3 and 5 layers of carbon FRP (fiber reinforced polymer) sheet and subjected to monotonic and cyclic axial compressive loading. Teflon sheets were used between concrete and steel loading plates to reduce friction. Pretests were made to estimate the proper overlap length of the external layer. The confining effect is addressed in terms of concrete strength, ductility and expansion. Considerable increase in levels of strength and strain at failure were achieved even for high strength concrete for monotonic and cyclic mode of loading.

Keywords: Concrete, FRP fiber reinforced polymer, confinement, cyclic, strength, ductility

1 INTRODUCTION

Carbon FRP tube or sheet (jacket) reinforcement has linear elastic behavior up to failure and exerts an ever increasing confining pressure on wrapped concrete cylinder loaded in compression. Concrete subjected to the tri-axial stress state described above, reveals remarkable enhancement of strength as well as ductility [1-5]. Shear cone failure of the concrete was observed in most reported experiments with FRP confined concrete with axial compressive load, as no attempt was made to reduce friction between the concrete and the steel loading plates. With use of teflon sheets, the friction can be reduced and the variation of lateral strain became uniform along concrete specimen height [6]. Shear cone failure is replaced by rather columnar type of failure.

In literature available, the overlap length of the FRP sheet varies and is taken without any calculation or pretests [7-9]. At wrapping the sheet is turned around the cylinder the necessary number of layers and then is the end overlapped the place where the wraps began. If the overlap does not fail the strength is determined by the not overlapped part of confinement. The configuration of the overlap as well as the overlap length affects the confinement volumetric ratio of the cross-section and the results obtained. With volumetric relation is meant the volume of FRP divided by the volume of concrete cylinder.

FRP confined concrete fails with the fracture of FRP jacket. Usually in modeling, the strain of the jacket at fracture is chosen according to the tensile ultimate strain of its fibers. Experiments have shown that the measured tensile ultimate strain (ε_{ju}) taken from FRP coupon tests is slightly lower than the ultimate strain of the fibers (given by the manufacturer). For FRP confined specimens this strain is lower than both values.

A systematic experimental investigation has been performed to study the behavior of carbon FRP confined concrete subjected to axial compressive load and to address identified gaps from previous research [10]. In this paper only a part of this investigation is presented consisting of 32 (of them 5 pretests) concrete cylinders in total with compressive strength 25.2 MPa and 51.8 MPa, confined by high modulus (377 GPa) carbon FRP sheet, in volumetric ratios (ρ_j) ranging from 0.31% ~ 1.56% and subjected to monotonic and cyclic load. Also pretests of five concrete cylinders are presented performed to estimate the proper overlap length. The enhanced mechanical behavior of carbon FRP sheet confined concrete is studied in terms of strength, ductility and expansion.

2 EXPERIMENTS

Three concrete mixtures were used. Target compressive strengths were 20 MPa and 60 MPa (two mixtures with different slump). The concrete composition, strength and modulus of elasticity of the used plain cylindrical specimens (diameter 150mm, height 300mm) are presented in table 1. The cube (side 150 mm) strength of concrete obtained was 33.4 MPa and 75.9 MPa respectively.

TABLE 1. Concrete mixtures, cylinder strength and E-modulus

Concrete									Average	
Target concrete strength (MPa)	Proportion of the mixture (/ m^3)							w/c	Strength MPa (cylindrical)	Modulus of Elasticity (GPa)
	c (kg)	k (kg)			w (liters)	Air %	slump (s) (mm)			
		Sand 0 -8 mm	Gravel 8-12 mm	Gravel 11-16 mm						
20	201	1205.3	364.4	364.4	189.5	2.4	10	0.94	25.2	17.3
60 a	496	887.7	399.4	399.4	189.4	2.4	13	0.38	51.8	24.6
60 b	496	887.7	399.4	399.4	189.4	2.4	15	0.38	56.9	25.3

The concrete cylinders were wrapped with unidirectional carbon fiber sheet BPE Composite 300M, made of Toray M40J carbon fibers and epoxy resin for the impregnation. The mechanical properties of the high E-modulus (377 GPa) sheet, table 2, were provided by the supplier.

TABLE 2. Carbon fiber properties

Toray M40J carbon fiber				BPE Composite 300M carbon sheet			
Tensile Strength, (MPa)	Tensile Modulus, (GPa)	Elongation, %	Density, kg/m^3	Type	Thickness, (mm)	Width, (mm)	Weight, (g/m^2)
4410	377	1,2	1770	Unidirectional	0,17	300	300

A total of 27 cylinders of the 20 and 60a (target strength) batch were tested under axial compressive load. The plain specimens, 3 in each of the groups, were subjected to monotonic compressive load up to failure. One specimen in each group of tree equal specimen, see table 3, was tested without use of teflon. The wrapped specimens (21) were tested under axial monotonic or cyclic load up to failure with use of teflon. In addition, three specimens of the 60b concrete batch were wrapped for pretests designed to estimate the proper overlap length of the carbon sheet. They were confined by one layer of carbon sheet with orientation perpendicular to their axis and had overlap lengths of 50 mm, 100 mm and 150 mm. The pretests confirmed the quality of wrapping performance, as well as the beneficial use of teflon sheets between the specimen and the loading plates in reducing friction.

Each group of cylinders consisted of three identical cylinders. The cylinders were wrapped with 1, 2 and 3 layers of carbon fiber sheet with orientation perpendicular to their axis and an overlap of 150 mm in external layer. From the 60a batch three more specimens were wrapped with 5 layers of carbon fiber sheet with confining reinforcement ratio (ρ_j) of 1.56%. Two of every three identical specimens were tested under monotonic load. The third one was tested under repeated load with the same load-unload rate.

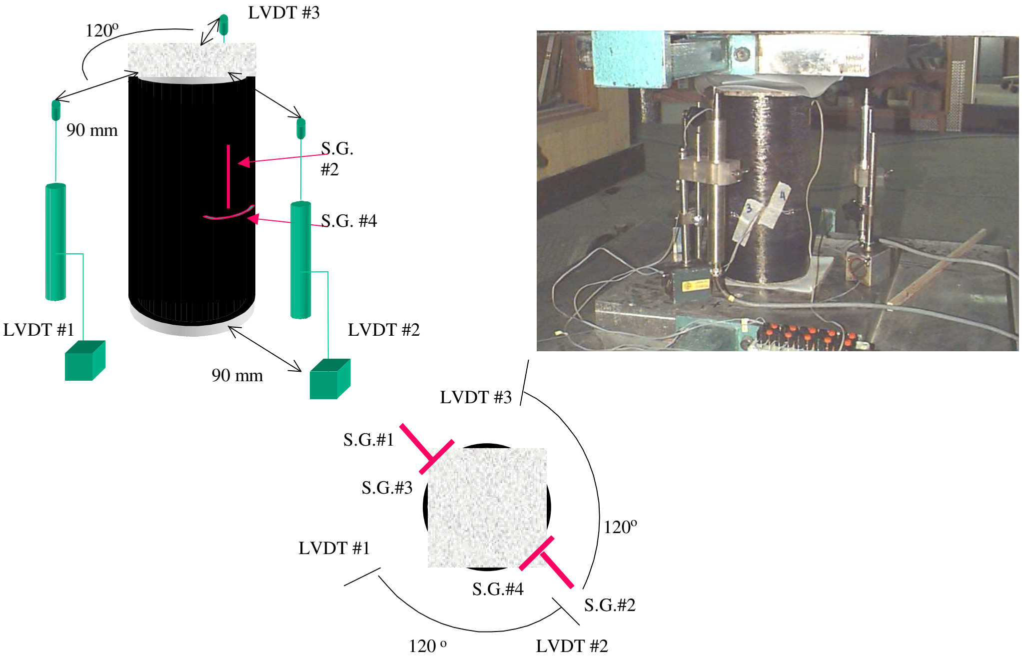

Figure 1. Instrumentation of specimens.

The load, axial displacement (LVDTs), axial strain and lateral strain (strain gauges, S.G.) were measured according to figure 1. The LVTD:s registered the change in distance between the loading plates and the contact surface deformations could be disregarded, as it turned out. The strain gauge measurements were influenced somewhat by the bending of the cylinders sides for cylinders with friction between loaded ends and loading plates.

All specimens were cured at 20^{o}C and 50% relative humidity and tested three and a half months after casting. For specimens with teflon caps, four teflon sheets with thickness 0.2 mm each were used. The loading machine capacity was 10000 kN. The rate was 10 MPa/minute at monotonic and cyclic loading, similar to that of ASTM C 39/C 39M–99 standards. The load–unload cycles were related to the unconfined concrete strength f_c and the ultimate strength of confined concrete f_{cc}. The load of each cycle was successively increased up to $0.5f_c$, $0.8f_c$, f_c, $\{f_c + 0.33(f_{cc} - f_c)\}$, $\{f_c + 0.66(f_{cc} - f_c)\}$ and finally up to failure.

3 EXPERIMENTAL RESULTS

3.1 Pretests - effect of the overlap length.

Three specimens of the 60b batch were wrapped with one layer of carbon sheet having different overlap lengths of 50 mm, 100 mm and 150 mm. For the specimen with 50 mm overlap length, teflon sheets were used between the steel loading plates and concrete surface. A premature failure occurred for this specimen with debonding of the carbon sheet due to inadequate overlap length, figure 2.a, developing an ultimate stress of 67.4 MPa (higher than strength of plain concrete 56.9 MPa). The other two specimens showed no overlap failure with ultimate stress 79.3 MPa and 78.7 MPa for 100 mm, figure 2.b, and 150 mm overlap length respectively. To be sure of avoiding lap failure 150mm overlap length was chosen for the tests.

Figure2.a. Debonding of specimen with 50 mm overlap length and use of teflon.

Figure2.b. Shear cone failure of specimen with 100 mm overlap length. (Without teflon)

Fig 3. Unconfined specimen 60a-3t (with teflon) after failure. Vertical cracks.

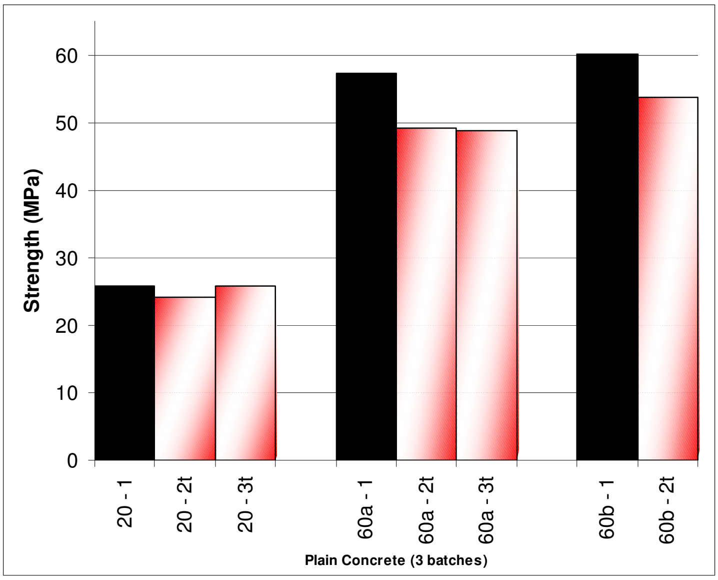

Fig. 4. Effect of the use of teflon sheet on concrete strength. Black column – without teflon.

3.2 Tests.

All tested plain concrete cylinders showed a relatively brittle type of failure. The specimens without teflon had a rather conical type of failure. The use of teflon reduced base friction and showed a rather columnar type of concrete fracture with a lot of vertical cracks formed, figure 3. Cylinders of 60a batch with teflon sheet developed lower strength than cylinders without (black column), figure 4.

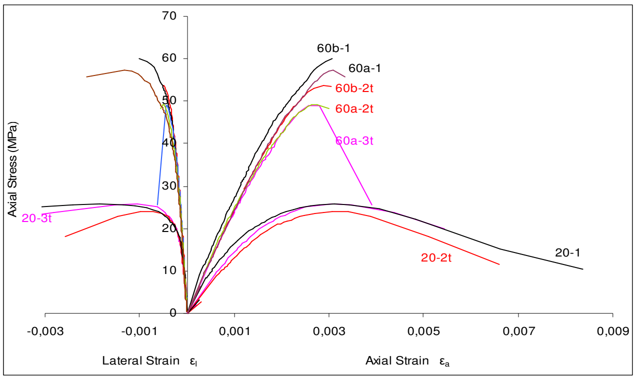

Figure 5. Axial and lateral stress–strain behavior of plain specimens from 20, 60a and 60b MPa concrete batches.

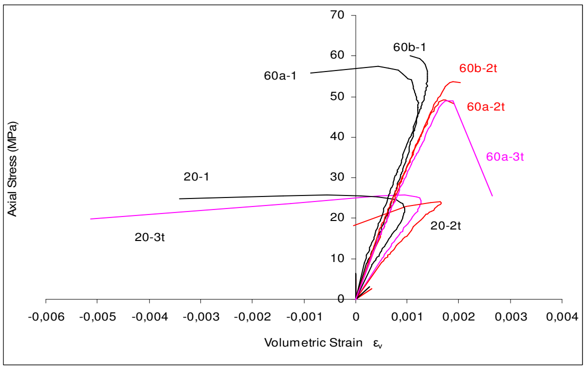

Fig. 6. Stress – volumetric strain behavior of plain specimens from 20, 60a and 60b MPa concrete batches.

The stress–strain response curves for plain specimens are presented in figures 5 and 6. The modulus of elasticity was 17.3 GPa for 25.2 MPa concrete strength and 24.6 GPa for 51.8 MPa concrete strength. The axial strain at ultimate stress was about 0.003 for all specimens and lateral strain about 0.001. Considering the dilation properties of unconfined concrete there was a rather stable volume reduction up to 0.87 – 0.93 of concrete strength for both concretes. After this characteristic level of stress the concrete expanded with an increasing rate. Experimental results are shown in table 3.

The behavior of carbon FRP confined specimens for the early stage of loading and around the ultimate load of unconfined concrete was similar to that of plain concrete. No differences in behavior could be observed between monotonic and cyclic mode of loading. Just before failure of many specimens, about 0.95 of the ultimate strength of confined concrete, a slight debonding at the overlap edge was observed, figure 7. a and b. This slight debonding was observed in several specimens regardless of the strength of concrete, the number of carbon sheet layers of confinement or the mode of loading. This slight debonding did not cause a reduction of load capacity of the specimens and couldn't be characterized as the initiation of failure as it was not growing. Sudden failure occurred in all the specimens after the fracture of the carbon FRP jacket. The absence of friction resulted in vertical cracks in the concrete core, figure 7.d.

Fig.7.a. Specimen 20c1L1C-1t after failure. Detection of the slight debonding at the overlap edge.

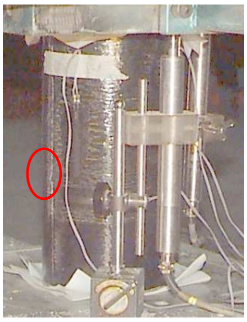

Fig. 7.b. Specimen 40(60a)c1L1-3t during occurrence of the slight debonding at the overlap edge.

Fig. 7.c. Specimen 20c1L1-3t after failure.

Fig. 7.d Specimen 60ac1L3-3t after failure.

In figures 8 to 11 is noticed for all the specimens that the confining effect gives an ever increasing strength response to expanding concrete up to failure for monotonic and cyclic mode of loading. A convergence in deformations between monotonic and cyclic axial loading of identical specimens was observed.

In early loading stage and up to about 0.9 of ultimate unconfined concrete load, the stress–strain response (axial, lateral and volumetric) of the composite system is similar to that of plain concrete. After 0.9 of ultimate unconfined concrete load disintegration of the concrete core is accelerated and cracks are formed. The jacket restricts with linear tensile stress-strain response the unstable behavior of concrete and a linear stress-strain relation is obtained up to failure, when the jacket breaks. Under cyclic loading the same behavior is obtained, figures 8 and 10. The FRP jacket with its elastic behavior up to failure regardless of the number of cycles (the tests included loading up to 6 cycles), restores the characteristics of the composite system as if the load was monotonic.

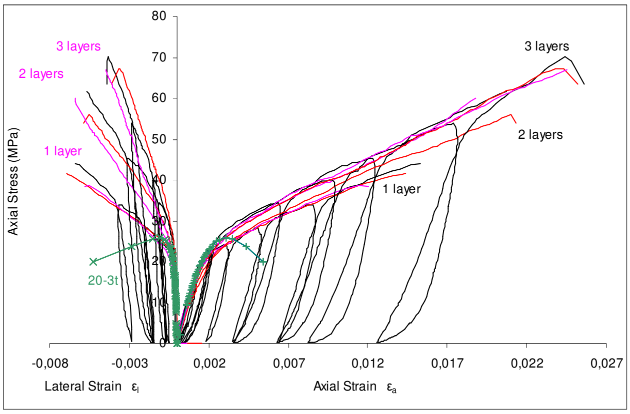

Figure 8. Stress–strain behavior of specimens. 20 MPa concrete confined with 0, 1, 2 and 3 layers of carbon FRP sheet.

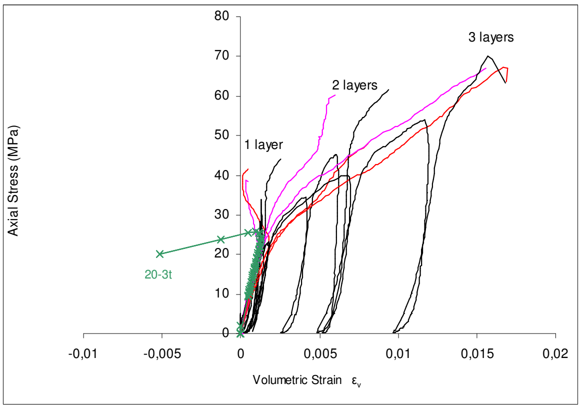

Figure 9. Stress–volumetric strain. 20 MPa concrete confined with 0, 1, 2 and 3 layers of carbon FRP sheet.

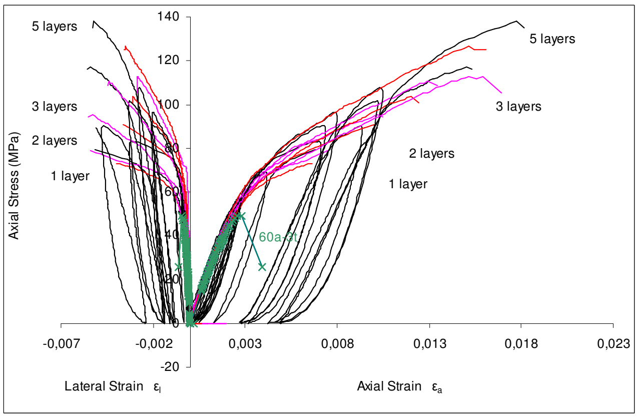

Figure 10. Stress–strain behavior of specimens. 60a MPa concrete confined with 0, 1, 2, 3 and 5 layers of carbon FRP sheet.

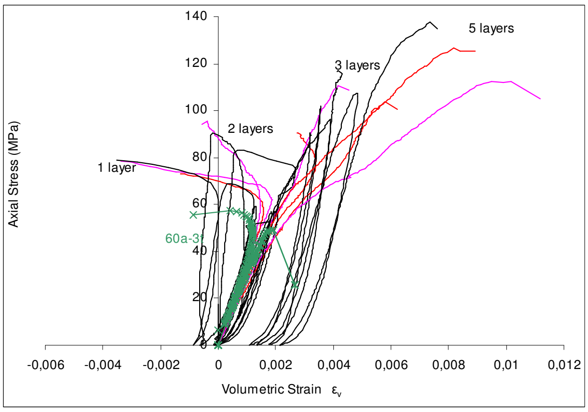

Figure 11. Stress–volumetric strain. 60a MPa concrete confined with 0, 1, 2, 3 and 5 layers of carbon FRP sheet.

The confining effect on strength and ductility of concrete is quantified and presented with the rest of experimental results in table 3. The labels given are decoded as follows: designed concrete strength (i.e. 20), composite material (i.e. c1), number of sheet layers (i.e. L1), mode of loading (i.e. blank for monotonic or C for cyclic), identical specimen number and finally use of teflon or not (i.e. t or blank).The confining effect of carbon FRP sheet is higher as the concrete strength is lower. For 25.2 MPa concrete strength and 2 layers of jacket the normalized ultimate load at failure varied from 2.22 – 2.38 while for 51.8 MPa the corresponding values ranged from 1.74 - 1.84 times the load of plain concrete. The normalized axial strains were between 6.04 – 6.74 and between 3.36 – 3.52 for the two concrete strengths respectively. The normalized lateral strain had similar reducing tendency for higher strength concrete.

For the confined specimens tested under repeated load–unload cycles the variation of strength and ductility was the same as for the monotonic mode of load. In fact for some specimens there were a gain in strength and ductility. In terms of concrete expansion it could be noticed from the stress–volumetric response diagrams that the carbon jacket tends to control concrete expansion, figures 9 and 11. For the same confinement volumetric ratio, the lower concrete strength results in better control of concrete expansion. This was evident from the fact that the lateral strain is better restricted in lower strength concrete. For specimens subjected to cyclic loading the same remarks are valid.

TABLE 3. Experimental results.

Test	Stress fc' $_{max}$, (MPa)	Axial Strain ε_{cu}	Lateral Strain ε_{lu}	Elastic Modulus ASTM (GPa)	Load Pc $_{max}$ / P_{co},	Axial Strain ε_{cu} / ε_{co}	Lateral Strain ε_{lu} / ε_{lo}
PRETESTS							
60b - 1	60,1	0,00307	-0,00101	27,4			
60b - 2t	53,7	0,00288	-0,00051	23,2			
Average 60b	56,9	0,00298	-0,00076	25,3			
60bc1L1/50mm-1t	67,4				1,18		
60bc1L1/100mm-1	79,3				1,39		
60bc1L1/150mm-1	78,7				1,38		
TESTS							
20 - 1	25,8	0,00312	-0,00184	18,9			
20 - 2t	24,2	0,00310	-0,00071	13,7			
20 - 3t	25,8	0,00312	-0,00106	19,2			
Average 20	25,2	0,00311	-0,00120	17,3			
20c1L1 - 2t	41,6	0,01437	-0,00695		1,65	4,62	5,78
20c1L1 - 3t	38,8	0,01206	-0,00581		1,53	3,88	4,83
20c1L1C - 1t	44,1	0,01533	-0,00639		1,75	4,93	5,31
20c1L2 - 1t	60,1	0,01881	-0,00641		2,38	6,04	5,33
20c1L2 - 2t	55,9	0,02097	-0,00551		2,22	6,74	4,58
20c1L2C - 3t	61,6	0,02075	-0,00569		2,44	6,67	4,73
20c1L3 - 1t	67,0	0,02452	-0,00449		2,65	7,88	3,73
20c1L3 - 2t	67,3	0,02432	-0,00368		2,66	7,82	3,06
20c1L3C - 3t	70,2	0,02442	-0,00435		2,78	7,85	3,61
60a - 1	57,4	0,00308	-0,00133	24,2			
60a - 2t	49,1	0,00274	-0,00050	25,3			
60a - 3t	48,8	0,00311	-0,00121	24,2			
Average 60a	51,8	0,00298	-0,00101	24,6			
60ac1L1 - 1t	78,7	0,00748	-0,00543		1,52	2,51	5,36
60ac1L1 - 3t	72,8	0,00663	-0,00398		1,41	2,23	3,93
60ac1L1C - 2t	79,2	0,00680	-0,00517		1,53	2,29	5,10
60ac1L2 - 1t	95,4	0,01047	-0,00551		1,84	3,52	5,44
60ac1L2 - 3t	90,7	0,01001	-0,00364		1,75	3,36	3,59
60ac1L2C - 2t	90,3	0,01020	-0,00513		1,74	3,43	5,06
60ac1L3 - 1t	110,5	0,01292	-0,00438		2,14	4,34	4,32
60ac1L3 - 2t	103,6	0,01203	-0,00310		2,00	4,04	3,06
60ac1L3C - 3t	117,2	0,01531	-0,00559		2,26	5,14	5,52
60ac1L5 - 1t	112,7	0,01593	-0,00289		2,18	5,35	2,85
60ac1L5 - 2t	126,7	0,01612	-0,00360		2,45	5,42	3,56
60ac1L5C - 3t	137,9	0,01814	-0,00526		2,66	6,09	5,19

Increasing the volumetric ratio of carbon jacket (more sheet layers) the axial stiffness of the jacket was increased. For plain concrete strength 25.2 MPa, the normalized values of ultimate load, in table 3, revealed an increase (mean values) from 1.64 for one layer of jacket, to 2.70 times the load of plain concrete for three layers. The increase in deformability (mean values) varied from 4.48 to 7.85 correspondingly. From normalized values in table 3 it could be noticed that the increase in both strength and ductility of the confined concrete (for every additional layer of jacket) was lower when the plain concrete strength was higher. However high strength concrete specimens wrapped with only five layers of high E-modulus carbon sheet reached the strength of (mean value) 125.8 MPa. No difference was noticed for specimens under cyclic mode of loading. Increase of the layer numbers of carbon jacket resulted in better control of concrete expansion for the same quality of concrete subjected to monotonic or cyclic loading

The carbon FRP jacket has a linear tensile stress-strain response up to failure and is under a tri-axial state of stress due to confining tension, concrete pressure and bond to concrete. The ultimate strain at failure of the carbon FRP jacket for concrete with strength 25.2 MPa ranged (mean values) from 0.00638 for one layer to 0.00417 for three layers. For the concrete strength 51.8 MPa and cylinder with five layers of CFRP, the strain at failure was 0.00392 (mean value). From the results presented in table 3 it becomes obvious that the strain at failure decreases with increased number of sheet layers. The strain at failure of the jacket was less than half of the tensile elongation of carbon fibers, table 2.

4 CONCLUSIONS

The behavior of concrete cylinders confined by carbon FRP sheet jacket was investigated experimentally under compressive load. The response of the composite system concrete–carbon FRP jacket depends on the material mechanical properties of the concrete and the carbon FRP sheet, the wrapping application performance, the overlap length, the volumetric confinement ratio as well as the mode of loading. Also the friction between concrete cylinder and steel loading plates affects the mode of failure of confined concrete. With use of teflon the mode of failure changes from shear cone to columnar, while in high strength concrete a decrease in ultimate stress is observed.

The results obtained from cylindrical concrete specimens confined by BPE Composite 300M carbon FRP sheet, with 150 mm overlap length, use of teflon four layer caps and tested under monotonic and cyclic axial compressive load, give a bilinear stress-strain relation and an ever increasing strength response due to expanding concrete above the unconfined concrete strength up to failure of jacket. Under cyclic loading the highest strength, 137.9 MPa at a strain of 0.01814 is obtained for 51.8 MPa concrete wrapped with 5 layers (structural thickness 0.6mm) of carbon FRP.

The carbon FRP confined concrete fails when the carbon sheet is fractured. The lateral measured strain at failure may be lower than the half of the tensile elongation at failure of carbon fibers. The ultimate strain of the jacket for the 25.2 MPa concrete shows a decrease with the number of carbon sheet layers, from 0.00638 for one layer to 0.00417 for three layers. For high concrete strength there is a similar tendency but not so clear. In general the strain at failure of the jacket fibers is lower than the nominal tensile elongation at failure of the carbon fibers and decreases with the number of sheet layers.

ACKNOWLEDGEMENT

The investigation was sponsored by European Commission - TMR - Network, ConFibreCrete "Research leading to the Development of Design Guidelines for the use of FRP in Concrete Structures", Chalmers University of Technology and Åke and Greta Lissheds Foundation, SEB Bank, 106 40 Stockholm.

REFERENCES

[1] Mirmiran A., Shahawy M.: Behavior of Concrete Columns Confined by Fiber Composites. ASCE Journal of Structural Engineering, V. 123, No. 5, May 1997. pp. 583-590.

[2] Harries K.A., Kestner J., Pessiki S., Sause R., Ricles J.: Axial Behavior of Reinforced Concrete Columns Retrofit with FRPC Jackets. Proceedings of the 2nd International Conference on Composites in Infrastructure ICCI'98, 5-7 January 1998. Tucson, Arizona. pp.411-425.

[3] Matthys S., Taerwe L., Audenaert K.: Tests on Axially Loaded Concrete Columns Confined by Fiber Reinforced Polymer Sheet Wrapping. 4th International Symposium on Fiber Reinforced Polymer Reinforcement for Reinforced Concrete Structures, 1999. pp. 217-228.

[4] Wang Y.C., supervised by Restrepo J.I. and Park R.: Retrofit of Reinforced Concrete Members Using Advanced Composite Materials. University of Canterbury, Civil Engineering, Research Report 2000-3. Christchurch, New Zealand, February 2000.

[5] Καραμπίνης Α.Ι., Ρουσάκης Θ.Χ.: Κυλινδρικά στοιχεία σκυροδέματος περισφιγμένα με ανθρακονήματα σε αξονική καταπόνηση, Α' Ελληνικό Συνέδριο Σύνθετων Υλικών Σκυροδέματος, 9 – 10 Νοεμβρίου 2000 (in Greek).

[6] Sjöström G.O., Svensson J.I.: Utveckling av metod för mätning av värme- och destruktionsenergi vid utmattning av betong. Examensarbete 85:3. Chalmers Tekniska Högskola, Avdelningen för Byggnadsmaterial. Göteborg, November (1985).

[7] Kono S., Inazumi M., Kaku T.: Evaluation of Confining Effects of CFRP Sheets on Reinforced Concrete Members. Proceedings of the 2nd International Conference on Composites in Infrastructure ICCI'98, 5-7 January 1998. Tucson, Arizona. pp.343-355.

[8] Miyauchi K., Nishibayashi S., Inoue S.: Estimation of strengthening effects with carbon fiber sheet for concrete column. Proceedings of the Third International Symposium (FRPRCS-3) on Non-Metallic (FRP) Reinforcement for Concrete Structures, Saporo, Japan, 14-16 October 1997. Vol 1, pp. 217-224.

[9] Rochette P., Labossiére P.: Axial Testing of Rectangular Column Models Confined with Composites. ASCE Journal of Composites for Construction, V. 4, No. 3, August 2000. pp. 129-136.

[10] Rousakis T. (2001). "Experimental investigation of concrete cylinders confined by carbon FRP sheets, under monotonic and cyclic axial compressive load". Research Report No 44, Division of Building Technology, Chalmers University of Technology, Göteborg, Sweden. 2001. p. 87.